Zinc availability in the tumor microenvironment dictates anti-PD1 response in *CDKN2A*^{Low} tumors via increased macrophage phagocytosis

Raquel Buj[1]*, Aidan R. Cole[1], Jeff Danielson[1], Jimmy Xu[2], Drew Hurd[3], Akash Kishore[4,5], Katarzyna M. Kedziora[6], Jie Chen[3], Baixue Yang[1,7], David Barras[8], Apoorva Uboveja[1], Amandine Amalric[1], Juan J. Apiz Saab[9], Jayamanna Wickramasinghe[10], Naveen Kumar Tangudu[1], Evan Levasseur[1], Hui Wang[1], Aspram Minasyan[8], Rebekah E. Dadey[3], Allison C. Sharrow[1], Sheryl Kunning[12], Frank P. Vendetti[11], Dayana B. Rivadeneira[12], Christopher J. Bakkenist[1,11], Tullia C. Bruno[12], Greg M. Delgoffe[12], Nadine Hempel[3], Nathaniel W. Snyder[13], Riyue Bao[3], Adam C. Soloff[14], John M. Kirkwood[3], Denarda Dangaj Laniti[8], Andrew V. Kossenkov[10], Alexander Muir[9], Jishnu Das[4], Diwakar Davar[3], Clementina Mesaros[2], Katherine M. Aird[1]*

[1]Department of Pharmacology & Chemical Biology and UPMC Hillman Cancer Center, University of Pittsburgh School of Medicine, Pittsburgh, PA

[2]Department of Pharmacology, University of Pennsylvania, Philadelphia, PA

[3]Department of Medicine and UPMC Hillman Cancer Center, University of Pittsburgh, Pittsburgh, PA

[4]Center for Systems Immunology, Departments of Immunology and Computational & Systems Biology, University of Pittsburgh School of Medicine, Pittsburgh, PA

[5]Joint Carnegie Mellon-University of Pittsburgh Ph.D. Program in Computational Biology, Pittsburgh, PA, USA

[6]Department of Cell Biology, Center for Biologic Imaging, University of Pittsburgh School of Medicine, Pittsburgh, PA

[7]Tsinghua University School of Medicine, Beijing, P.R. China

[8]Ludwig Institute for Cancer Research, Lausanne Branch, University of Lausanne (UNIL), Department of Oncology, Lausanne University Hospital (CHUV) and University of Lausanne, and Agora Cancer Research Center, Lausanne, Switzerland

[9]Ben May Department for Cancer Research, University of Chicago, Chicago, IL, USA

[10]The Wistar Institute of Anatomy and Biology, Philadelphia, PA

[11]Department of Radiation Oncology and UPMC Hillman Cancer Center, University of Pittsburgh School of Medicine, Pittsburgh, Pennsylvania, PA

[12]Department of Immunology and UPMC Hillman Cancer Center, University of Pittsburgh School of Medicine, Pittsburgh, PA

[13]Aging + Cardiovascular Discovery Center, Department of Cardiovascular Sciences, Lewis Katz School of Medicine, Temple University, Philadelphia, PA

[14]Department of Cardiothoracic Surgery and UPMC Hillman Cancer Center, University of Pittsburgh School of Medicine, Pittsburgh, PA

*Corresponding Authors

Katherine M. Aird, PhD
Associate Professor
UPMC Hillman Cancer Center
University of Pittsburgh School of Medicine
5051 Centre Ave.
Office: 2041; Lab 2050A
Pittsburgh, PA 15213
412-648-4823
Katherine.aird@pitt.edu

Starting September 2025:
Professor
The Wistar Institute
3601 Spruce Street
Philadelphia, PA 19014
kaird@wistar.org

and

Raquel Buj, PhD
Research Assistant Professor
5051 Centre Ave.
Office: 2050; Lab 2050A
Pittsburgh, PA 15213
Rbg19@pitt.edu

Starting September 2025:
Research Assistant Professor
The Wistar Institute
3601 Spruce Street
Philadelphia, PA 19014
rbuj@wistar.org

Running title: Zinc modulates anti-PD1 response in *CDKN2A*^{Low} tumors

Keywords: SLC39A9, ZIP9, tumor microenvironment (TME), Tumor associated macrophages (TAM), p16, anti-PD1, anti-PD-L1, immune checkpoint blockade (ICB), tumor interstitial fluid (TIF), dietary intervention, zinc, metabolism, metals

ABSTRACT

Anti-PD1 therapies are primarily thought to rely on functional T cell responses; yet tumors with limited T cell infiltration can still benefit, suggesting alternative mechanisms contribute to therapeutic efficacy. Indeed, we found that myeloid-rich, T cell-poor tumor models respond to anti-Pd1, and this is dependent on a cancer cell-macrophage crosstalk mediated by cancer cell *Cdkn2a* expression. Mechanistically, we found that cancer cells with decreased *Cdkn2a* expression (C*dkn2a*^{Low}), which occurs in ~50% of all human cancers, reorganize zinc compartmentalization by upregulating the zinc importer Slc39a9 at the plasma membrane. Increased cancer cell plasma membrane Slc39a9 leads to intracellular zinc accumulation in cancer cells and depletion of zinc in the tumor microenvironment (TME), resulting in zinc-starved tumor-associated macrophages (TAMs) with reduced phagocytic activity. Restoring zinc availability in TAMs—via dietary supplementation or Slc39a9 knockdown in cancer cells—reprograms TAMs to a pro-phagocytic state and sensitizes *Cdkn2a*^{Low} tumors to anti-Pd1 therapy. Remarkably, Slc39a9 knockdown tumors respond to anti-Pd1 in Rag1$^{-/-}$ mice, and co-injection of zinc-replete macrophages is sufficient to drive an anti-Pd1 response in immunodeficient mice, demonstrating the T cell-independent nature of this response. Clinically, TAMs from *CDKN2A*^{Low} cancer patients show reduced zinc and phagocytosis gene signatures. Moreover, patients with lower circulating zinc levels have significantly worse time-to-event outcomes than those with higher levels. Together, these findings uncover a previously unrecognized mechanism by which *Cdkn2a*^{Low} cancer cells outcompete TAMs for zinc, impairing their function and limiting anti-Pd1 efficacy. They also provide evidence that macrophages alone,

117 without T cells, can enhance anti-PD1 response through zinc-mediated reprogramming
118 of phagocytosis.

INTRODUCTION

A number of data mining studies have highlighted a significant correlation between Cyclin-Dependent Kinase Inhibitor 2A gene (*CDKN2A*) genetic alterations and a pro-tumorigenic tumor microenvironment (TME), including TMEs with decreased T cell infiltration[1-6]. Prior studies have also shown a correlation between loss of *CDKN2A* function and poor response to immune checkpoint blockade (ICB) therapies[1-18]. ICB therapies, particularly monoclonal antibodies targeting the PD-1/PD-L1 axis, have become a cornerstone in cancer treatment, demonstrating significant clinical success across several cancers[19-23]. Their effectiveness is primarily attributed to enhancing T cell activity and T cell-mediated tumor killing[24]. However, published studies have described specific contexts in which tumors with low T cell infiltration but high myeloid cell content show responsiveness to immunotherapies, including ICB[25-28]. Supporting this notion, recent evidence suggests that at least a subset of tumor-associated macrophages (TAMs) play a role in the response to ICB[28-35]. Anti-PD-1/PD-L1 therapies can directly affect monocytes and macrophages to improve therapeutic responses at least in part by increasing their phagocytic activity[28,29,36-38]. Indeed, studies have shown that increased TAM phagocytic activity inhibits tumor growth in mouse models[39-41]. However, the mechanisms underlying this enhancement of TAM phagocytosis remain unclear.

The *CDKN2A* gene, located on chromosome 9p21, is a critical tumor suppressor and one of the most frequently altered loci in human cancers[42-45]. Disruption of *CDKN2A* typically occurs through promoter hypermethylation and genetic deletions, resulting in the loss of *CDKN2A* mRNA expression[46-48]. These alterations are observed in 12% to 80% of

143 tumors, depending on cancer type and stage[49]. Additionally, loss-of-function mutations in
144 the *CDKN2A* coding sequence represent another common mechanism of disruption, oc-
145 curring in approximately 6% to 16% of cases, with frequencies also depending on tumor
146 context[48,49]. *CDKN2A* encodes two distinct proteins through alternative reading frames:
147 $p14^{ARF}$ ($p19^{ARF}$ in mice) and $p16^{INK4A}$ (hereafter p16), both of which are essential regula-
148 tors of the cell cycle[50]. While the canonical roles of *CDKN2A* in cell cycle regulation and
149 senescence induction are well established[51,52], evidence from our laboratory and others
150 suggests that its functions extend beyond this paradigm[13,18,53-63]. We have demonstrated
151 that loss of *CDKN2A*/p16 expression reprograms intracellular metabolism, enhancing key
152 biosynthetic metabolites that contribute to cellular proliferation and tumorigenesis, includ-
153 ing nucleotides and cholesterol[54,56]. However, whether this metabolic disruption down-
154 stream of *CDKN2A* loss affects the metabolic landscape of the TME remains unexplored.
155 Additionally, while metabolic reprogramming is known to influence macrophage phago-
156 cytic activity[39,64,65], the role of cancer cell-TAM nutrient competition in driving this process
157 remains poorly understood.
158
159 Zinc is an essential trace element obtained through the diet[66] and is the second most
160 abundant metal in the human body[67]. Over 2,500 human proteins depend on zinc for
161 structural or functional roles (e.g. zinc fingers and cofactors)[67], reflecting its broader im-
162 portance in numerous cellular processes, including immune responses[68-75]. Therefore,
163 tight regulation of zinc homeostasis is essential. The SLC39A family members, also
164 known as ZRT- and IRT-like proteins (ZIP), increase cytosolic zinc by importing it from
165 the extracellular environment or releasing it from intracellular organelles[76]. In contrast,

166 the SLC30A family members or zinc transporter (ZNT) proteins, reduce cytosolic zinc by
167 transporting it into organelles or exporting it to the extracellular space[77]. Indeed, dysreg-
168 ulated zinc homeostasis, due to altered transport or systemic deficiency, has been linked
169 to multiple malignancies[78-90]. Moreover, *in vivo* studies have shown that zinc supplemen-
170 tation can reduce tumor burden, enhance resistance to tumor challenges, and decrease
171 the incidence of spontaneous tumors in mice[91-94], suggesting a potential therapeutic role
172 for zinc in cancer treatment. Additionally, recent reports have found that patients who
173 respond to ICB have TAMs with metal/zinc signatures[30], and an elevated serum zinc level
174 has recently been associated with improved ICB responses in cancer patients[95]. While
175 some studies have explored the link between zinc and immunotherapy response[96-100], the
176 results remain contradictory, and the precise molecular mechanisms underlying zinc in
177 the TME are unclear.
178
179 Here, we found that in myeloid-rich, T cell-poor tumors, the expression of *Cdkn2a* in can-
180 cer cells determines the response to anti-Pd1 by regulating zinc compartmentalization,
181 which in turn modulates TAM phagocytic activity. By cross-comparing differentially regu-
182 lated metabolites and metals in the tumor interstitial fluid (TIF) and negatively enriched
183 plasma membrane solute carrier transporters (SLCs) from a metabolism-focused *in vivo*
184 CRISPR knockout screen, we identified zinc and the zinc importer Slc39a9 as critical
185 regulators of anti-Pd1 resistance in tumors with low *Cdkn2a* mRNA expression
186 (*Cdkn2a*^{Low}). *Cdkn2a*^{Low} cells have increased cholesterol-driven plasma membrane (PM)
187 localization of Slc39a9, leading to elevated intracellular zinc and a zinc-depleted TME.
188 This competition for zinc within the TME leads to decreased zinc in TAMs, reducing their

189 phagocytic activity and impairing anti-Pd1 response. Restoring TME zinc levels through
190 Slc39a9 knockdown in cancer cells or dietary zinc supplementation rescues TAM function
191 and enhances anti-Pd1 response. Excitingly, this was independent of T cells. Using pub-
192 licly available single-cell RNA-Sequencing (scRNA-Seq), we also found that zinc and
193 phagocytosis signatures were impaired in TAMs from patients with *CDKN2A*^{Low} tumors.
194 These findings highlight zinc homeostasis as essential for anti-PD1 efficacy in
195 *CDKN2A*^{Low} tumors, emphasize T cell-independent mechanisms of anti-PD1 response,
196 and have clinical implications for the use of zinc supplements to improve patient out-
197 comes.

198 **RESULTS**

199

200 **Expression of *CDKN2A*/p16 in cancer cells modulates anti-PD1 response in mye-**
201 **loid-rich, CD8 T cell-poor tumors**

202 Loss of *CDKN2A* is a common event in cancer cells[49], including melanoma, where ~40%
203 of patients show reduced *CDKN2A* expression[101,102]. Published studies show that tumors
204 with loss of *CDKN2A* correlate with decreased response to ICB, including anti-
205 PD1[1,7,9,12,14-17]. Consistently, using publicly available data, we found that melanoma pa-
206 tients with low *CDKN2A* mRNA expression (*CDKN2A*^{Low}) have shorter overall survival
207 compared to those with high *CDKN2A* mRNA expression (*CDKN2A*^{High}) following anti-
208 PD1 treatment (**Fig. 1A**). Therefore, we sought to determine the mechanisms by which
209 *CDKN2A* loss in cancer cells contributes to anti-PD1 resistance. Towards this goal, we
210 developed two complementary syngeneic models. In the first model, *Cdkn2a* expression
211 was knocked down in the *Cdkn2a*^{High} murine melanoma cell line Yumm5.2 (**Fig. S1A**). In
212 the second model, p16 was expressed at physiological levels in the *Cdkn2a*^{Null} melanoma
213 cell line Yumm1.7 (**Fig. S1B**). Note that we did not observe differences in cell proliferation
214 or senescence upon physiological expression of p16 (**Fig. S1C-D**). Additionally, p19 re-
215 mained unexpressed in the Yumm1.7 cells with p16 expression (**Fig. S1B**); thus, results
216 with this model specifically relate to p16 function. *CDKN2A* is located on chromosome
217 9p21 in humans and 4qC4 in mice. In both species, this region also contains *MTAP* and
218 the interferon (IFN) gene cluster, which are frequently co-deleted with *CDKN2A* in can-
219 cer[1,103,104]. Importantly, both of our models have intact *Mtap* and *Ifn* gene cluster (**Fig.**
220 **S1E-F**); therefore, all subsequent observations with these models are related only to

221 *Cdkn2a*. Herein, for simplicity, Yumm5.2 and Yumm1.7 with p16 expression are referred
222 to as *Cdkn2a*^{High,} while Yumm5.2 with knockdown of *Cdkn2a* and Yumm1.7 cells are re-
223 ferred to as *Cdkn2a*^{Low} cancer cells (**Fig. S1G**). Importantly, both syngeneic tumors mimic
224 the ICB response seen in cancer patients, where decreased mRNA expression of *Cdkn2a*
225 in both models leads to anti-Pd1 resistance (**Fig. 1B-C**).
226
227 Given the central role of the tumor immune microenvironment in dictating ICB out-
228 comes[105], we next investigated how *Cdkn2a* expression in cancer cells shapes the im-
229 mune compartment. Towards this goal, we performed scRNA-Seq on Cd45^{+} immune cells
230 isolated from the Yumm5.2 isogenic model in mice treated with and without anti-Pd1. We
231 found that these tumors are heavily enriched in myeloid cells (>95% of all Cd45^{+} cells)
232 and poor in conventional T cells (<1% of all Cd45^{+} cells), regardless of *Cdkn2a* status or
233 anti-Pd1 treatment (**Fig. 1D** and **S1H**). This myeloid-rich, T cell–poor composition aligns
234 with prior reports showing that *Cdkn2a*^{Low} tumors show reduced T cell infiltration[1-6] and
235 reflects the immune landscape observed in many human tumors[106]. Intriguingly, despite
236 the paucity of T cells, shControl (*Cdkn2a*^{High}) tumors still respond to anti-Pd1 (**Fig. 1B-C**).
237 Thus, these data point to a potential T cell-independent mechanism of anti-Pd1 response
238 in these tumors, which we aimed to explore. Interestingly, Gene Set Enrichment Analysis
239 (GSEA) of scRNA-seq data from the myeloid compartment showed broadly reduced in-
240 flammatory signals in Yumm5.2 sh*Cdkn2a* compared to shControl tumors (**Fig. 1E**). This
241 is consistent with prior research showing that anti-inflammatory myeloid cells have pro-
242 tumorigenic functions that suppress ICB responses[107-109]. Therefore, we aimed to deter-
243 mine whether depletion of myeloid cells in *Cdkn2a*^{Low} tumors would phenocopy the

244 improved response to anti-Pd1 observed in *Cdkn2a*^{High} tumors. To test this, we treated

245 mice bearing Yumm5.2 sh*Cdkn2a* tumors with pexidartinib, a CSF1R inhibitor known to

246 effectively reduce tumor myeloid cells[110,111]. Unexpectedly, myeloid depletion (**Fig. S1I**)

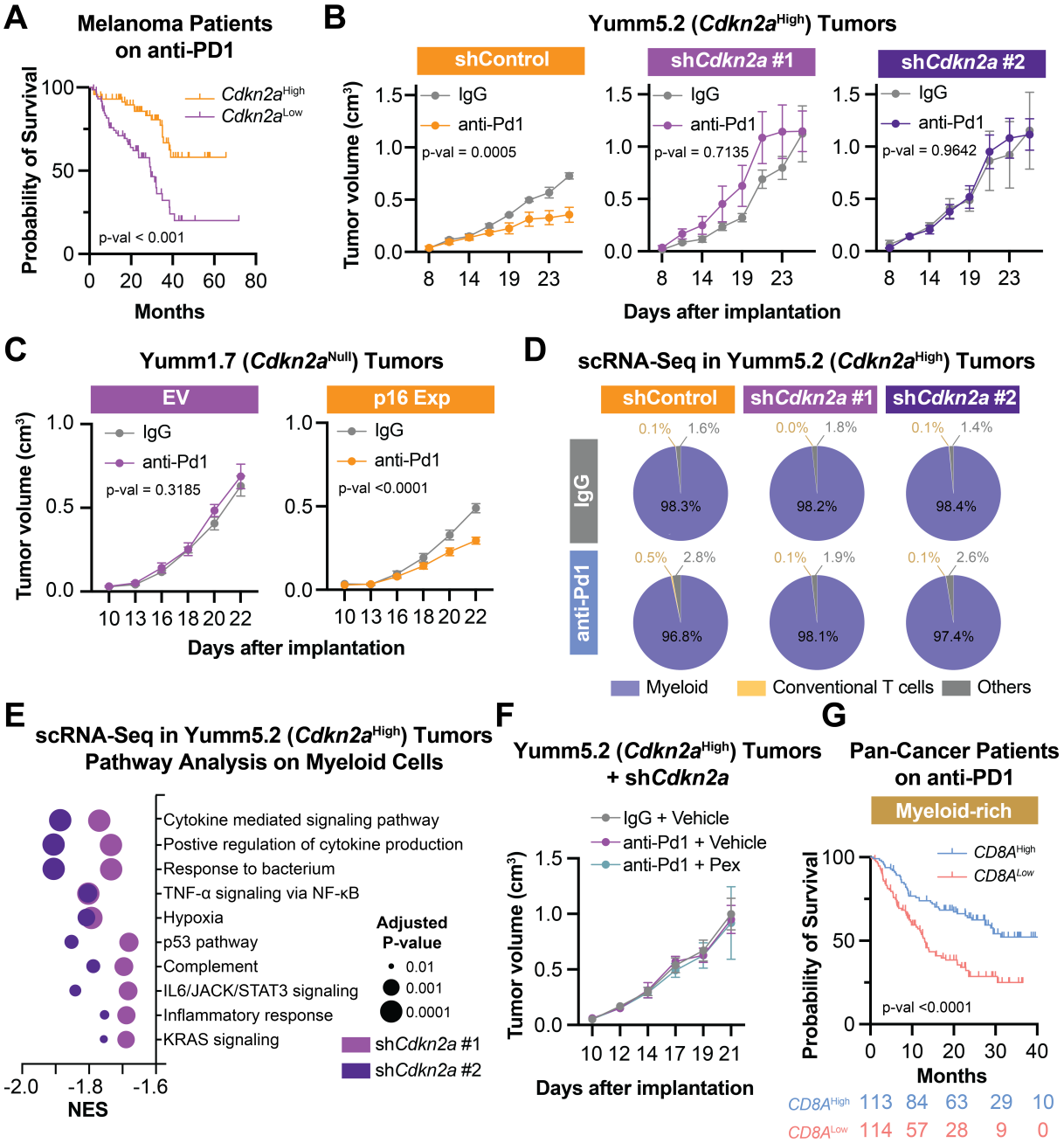

Figure 1. Loss of *CDKN2A* expression abrogates anti-PD1 efficacy in myeloid-rich, CD8 T cell-poor tumors. (A) Overall survival of melanoma patients treated with anti-PD1 stratified by *CDKN2A* mRNA expression. Melanoma Patient Cohort; Log-rank (Mantel-Cox) test. **(B)** Longitudinal tumor growth in mice implanted with Yumm5.2 (*Cdkn2a*^{High}) cells with knockdown of GFP (shControl) or *Cdkn2a* (sh*Cdkn2a,* hairpins #1 and #2) and treated with IgG or anti-Pd1 (200 µg,

i.p., 3×/week). Mean ± SEM (n=4/group); mixed-effects model. **(C)** Longitudinal tumor growth in mice implanted with Yumm1.7 (*Cdkn2a*^{Null}) cells expressing empty vector (EV) or physiological levels of p16 (p16 Exp) and treated with IgG or anti-Pd1 (200 µg, i.p., 3×/week). Mean ± SEM (n=8/group); mixed-effects model. **(D-E)** Cd45^{+} cells from the indicated Yumm5.2 (*Cdkn2a*^{High}) tumors treated with IgG or anti-Pd1 (200 µg, i.p., 3×/week) were sorted and used for scRNA-Seq. **(D)** Pie charts showing percentages of immune cell types. **(E)** Dot plot showing the top 10 significant gene signatures from gene set enrichment analysis (GSEA) performed in the myeloid subset. NES = normalized enrichment score. **(F)** Longitudinal tumor growth in mice implanted with Yumm5.2 (*Cdkn2a*^{High}) cells with knockdown of *Cdkn2a* and treated with pexidartinib (Pex, 45 mg/kg, o.g., 3×/week) or vehicle in combination with IgG or anti-Pd1 (200 µg, i.p., 3×/week). Mean ± SEM (n=6/group); mixed-effects model. **(G)** Overall survival of anti-PD1-treated, myeloid-rich (*ITGAM* mRNA expression above the group average) cancer patients stratified by *CD8A* mRNA expression. KMP Patient Cohort; Log-rank (Mantel-Cox) test.

failed to sensitize sh*Cdkn2a* tumors to anti-Pd1 (**Fig. 1F**). These findings indicate that the overall anti-inflammatory bulk myeloid compartment is not the primary driver of anti-Pd1 resistance in *Cdkn2a*^{Low} tumors.

CD8 T cells are commonly considered the main mediators of anti-PD1 responses[112,113]. However, both *Cdkn2a*^{High} Yumm tumor models respond to anti-Pd1 treatment (**Fig. 1B-C**) despite being Cd8 T cell-poor – particularly Yumm5.2 tumors, which are severely depleted (**Fig. 1D, S1H, and S1J**). Interestingly, there is literature to demonstrate that specific myeloid subsets also contribute to the therapeutic efficacy of ICB[28,30,35,114]. In this regard, analysis of publicly available bulk RNA-seq data from anti-PD1-treated patients showed that 21% of tumors with high *ITGAM* (encoding for CD11B) and low *CD8A* expression (reflecting a myeloid-rich, T cell-poor TME) had similar survival at 20 months to tumors with both high *ITGAM* and high *CD8A* (reflecting a myeloid-rich, T cell-rich TME; **Fig. 1G**). Surprisingly, 7.9% of the myeloid-rich, T cell-poor group maintained similar survival even at 30 months (**Fig. 1G**). Together, these data suggest that a subset of myeloid cells may actively contribute to the anti-PD1 response, even in a T cell-poor environment. In this study, we took advantage of the Yumm models as they provide a unique platform

264 to investigate how myeloid cells, in the context of high *Cdkn2a,* may promote anti-Pd1
265 responses in a T cell-poor TME.
266
267 ***Cdkn2a*^{Low} tumors have impaired anti-Pd1-mediated TAM phagocytosis**
268 We found that depletion of the bulk myeloid compartment does not sensitize T cell-poor
269 sh*Cdkn2a* Yumm5.2 tumors to anti-Pd1 (**Fig. 1F** and **S1I**) and that some patients with
270 myeloid-riched, T cell-poor tumors show sustained benefit from anti-PD1 (**Fig. 1G**). To-
271 gether, these data suggest that a specific subset of myeloid cells may unexpectedly pro-
272 mote, not inhibit, an anti-PD1 response. To explore this idea, we further investigated the
273 different types of myeloid cells in our scRNA-Seq. We found that the large majority of
274 myeloid cells in these tumors are tumor-associated macrophages (TAMs) (**Fig. 2A**). In-
275 terestingly, a growing body of recent literature has reported that TAMs alone drive re-
276 sponse to ICB by promoting phagocytosis[28,29,36-38]. Consistently, analysis of publicly avail-
277 able patient data shows that when phagocytosis is high, overall survival following anti-
278 PD1 treatment is not significantly different between T cell-rich and T cell-poor tumors (**Fig.
279 2B**). Therefore, we sought to determine the role of anti-Pd1-mediated TAM phagocytosis
280 in our models. Further analysis of our scRNA-seq revealed a significant increase in phag-
281 ocytosis-related gene signatures in TAMs following anti-Pd1 treatment in Yumm5.2
282 shControl (*Cdkn2a*^{High}) but not in sh*Cdkn2a* (*Cdkn2a*^{Low}) tumors (**Fig. 2C** and **Table S1**).
283 Notably, even in IgG treated mice, Yumm5.2 shControl tumors showed modestly higher
284 phagocytic activity scores in TAMs compared to Yumm5.2 sh*Cdkn2a* tumors (**Fig. 2C** and
285 **Table S1**), suggesting that TAMs in *Cdkn2a*^{Low} tumors impair basal TAM phagocytosis

286 that is further exacerbated by anti-Pd1. To assess whether this is relevant in human tu-

287 mors, we analyzed publicly available scRNA-seq data from patients with melanoma and

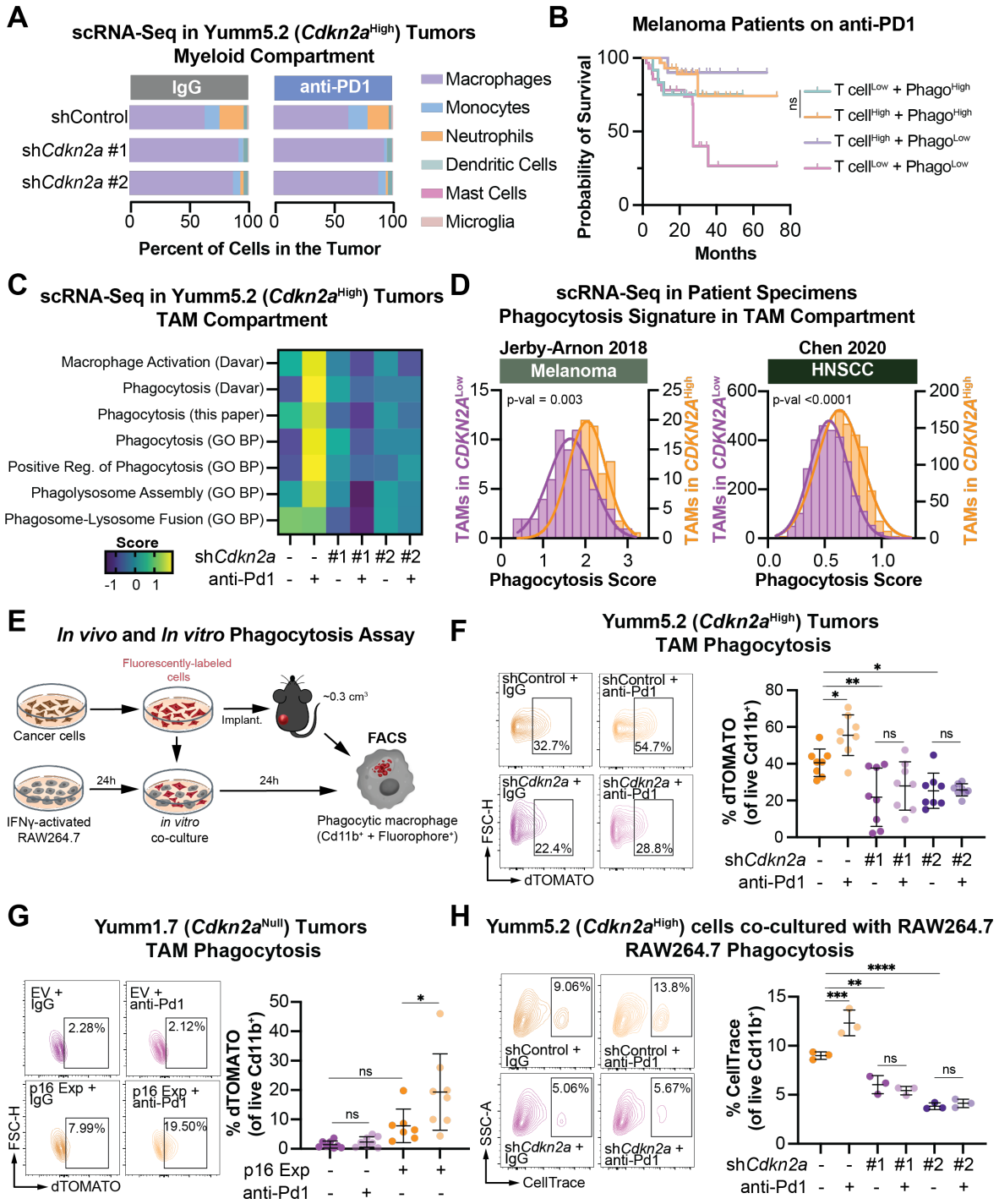

Figure 2. Loss of *CDKN2A* expression in cancer cells impairs tumor-associated macrophage (TAM) phagocytic activity. (A) Cd45⁺ cells from the indicated Yumm5.2 (*Cdkn2a*^{High}) tumors treated with IgG or anti-Pd1 (200 µg, i.p., 3×/week) were sorted and used for scRNA-Seq. Bar plots

showing percentages of myeloid cell types. **(B)** Overall survival of anti-PD1-treated patients stratified by T cell inflamed score and phagocytic score (see **Table S1**). Melanoma Patient Cohort; Log-rank (Mantel-Cox) test. **(C)** Heatmap of phagocytosis signature scores in the TAM compartment from scRNA-seq of Yumm5.2 (*Cdkn2a*^{High}) tumors from (A)**. (D)** Histogram showing the phagocytosis score in TAMs from the indicated scRNA-Seq datasets from melanoma and head and neck squamous cell carcinoma (HNSCC) patients stratified by *CDKN2A* expression in cancer cells. Linear mixed model. **(E)** Schematic of *in vivo* and *in vitro* phagocytosis assays. **(F)** dTOMATO-labeled Yumm5.2 (*Cdkn2a*^{High}) cells with knockdown of GFP (shControl) or *Cdkn2a* (sh*Cdkn2a,* hairpins #1 and #2) were injected into mice (see schematic in panel E), and mice were treated with IgG or anti-Pd1 (200 µg, i.p., 3×/week). Representative flow cytometry plots (left) and quantification (right) of the percentage of TAMs with dTOMATO signal (phagocytic TAMs). Mean ± SD; one-way ANOVA. **(G)** dTOMATO-labeled Yumm1.7 (*Cdkn2a*^{Null}) cells expressing empty vector (EV) or physiological levels of p16 (p16 Exp) were injected into mice (see schematic in panel E), and mice were treated with IgG or anti-Pd1 (200 µg, i.p., 3×/week). Representative flow cytometry plots (left) and quantification (right) of phagocytic TAMs. Mean ± SD; one-way ANOVA. **(H)** CellTrace™ Violet-labeled Yumm5.2 (*Cdkn2a*^{High}) cells with shControl or sh*Cdkn2a* knockdown were co-cultured with RAW264.7 macrophages. Cells in co-culture were treated with IgG or anti-Pd1 (1 µg/mL, 24 h). Representative flow cytometry plots (left) and quantification (right) of the percentage of RAW264.7 with CellTrace™ Violet signal (phagocytic RAW264.7 macrophages). Mean ± SD; one-way ANOVA. * $p<0.05$, ** $p<0.01$, *** $p<0.001$, **** $p<0.0001$, ns = not significant.

head and neck squamous cell carcinoma (HNSCC), cancers where *CDKN2A* loss is common and clinically relevant[49]. Consistent with our mouse tumor scRNA-Seq data, we observed reduced TAM phagocytosis signatures in *CDKN2A*^{Low} vs. *CDKN2A*^{High} patient tumors (**Fig. 2D**), underscoring the clinical relevance of our findings. To functionally validate these observations, we generated fluorescently-labeled cancer cells and assessed *in vivo* and *in vitro* phagocytosis by measuring the percentage of Cd11b^{+} cells that have engulfed fluorescently-labeled cancer cells (**Fig. 2E** and **Fig. S2**), similar to previous reports[29,115]. We acknowledge the limitation that Cd11b is not a specific TAM marker, as other myeloid cells can also express Cd11b. However, given that the overwhelming majority (60-90%) of phagocytic myeloid cells in these tumors are TAMs (**Fig. 2A**), the Cd11b^{+} population primarily reflects TAMs in these tumors. Consistent with our scRNA-Seq gene signatures, we observed that TAMs in both *Cdkn2a*^{High} tumor models were more phagocytic than those in *Cdkn2a*^{Low} tumors (**Fig. 2F-G**), although we note this was more pronounced in

301 the Yumm5.2 model. Moreover, anti-Pd1 treatment enhanced TAM phagocytosis only in
302 *Cdkn2a*^{High} tumors in both models (**Fig. 2F-G**). This increase in phagocytic activity in re-
303 sponse to anti-Pd1 aligns with the tumor growth reduction observed upon anti-Pd1 treat-
304 ment in both models (**Fig. 1B-C**). Together with patient data, these *in vivo* data demon-
305 strate that TAM phagocytosis is modulated by *CDKN2A* status in cancer cells. Finally, we
306 aimed to confirm that this is a direct effect on macrophages by performing *in vitro* co-
307 culture assays with cancer cells and IFNγ-activated RAW264.7 macrophages (**Fig. 2E**).
308 Consistent with our *in vivo* results, macrophages *in vitro* had higher phagocytic activity
309 towards *Cdkn2a*^{High} cancer cells, which was further enhanced by anti-Pd1 (**Fig. 2H**). This
310 effect was not observed when these macrophages were co-cultured with *in vitro*
311 *Cdkn2a*^{Low} cancer cells (**Fig. 2H**). Collectively, these data demonstrate that *Cdkn2a* ex-
312 pression in cancer cells directly regulates macrophage phagocytic activity and that anti-
313 Pd1 enhances macrophage phagocytosis, which corresponds to decreased tumor vol-
314 ume. These findings add to emerging evidence challenging the prevailing view that T cells
315 are always required to mediate responses to anti-PD1, instead highlighting a critical role
316 for TAMs.
317

318 **The zinc importer Slc39a9 in cancer cells abrogates anti-Pd1 response in**
319 ***Cdkn2a*^{Low} tumors via a TAM-dependent mechanism**

320 We found that *Cdkn2a*^{High} cancer cells promote increased TAM phagocytosis compared
321 to *Cdkn2a*^{Low} cancer cells both *in vitro* and *in vivo* and that anti-Pd1 treatment further
322 enhances this effect only in the context of *Cdkn2a*^{High} cells (**Fig. 2C-D and F-H**). TAMs
323 are highly plastic cells and responsive to the tumor's metabolic environment[116]. We and

324 others have published that suppression of *CDKN2A*/p16 alters cell-intrinsic metabo-
325 lism[54,55,58,59,117-119], although no study to date has assessed TME metabolites in the con-
326 text of *CDKN2A*^{Low} tumors. Analyzing the tumor interstitial fluid (TIF) by unbiased metab-
327 olomics and metalomics (**Fig. S3A**), we found that multiple analytes are also differentially
328 regulated in the TME of Yumm5.2 sh*Cdkn2a* tumors compared to controls (**Fig. 3A**).
329 Therefore, we hypothesized that these metabolic changes could extend beyond cancer
330 cells to influence the surrounding immune microenvironment, including TAMs. To identify
331 metabolic drivers of the altered TME in sh*Cdkn2a* tumors and evaluate their role in anti-
332 Pd1 resistance, we performed an *in vivo* CRISPR screen using a metabolism-focused
333 sgRNA knockout library in the Yumm5.2 isogenic model, with and without anti-Pd1 treat-
334 ment (**Fig. 3B**). We identified 137 genes with significant negative enrichment in sh*Cdkn2a*
335 tumors treated with anti-Pd1 vs. IgG compared to shControl tumors treated with anti-Pd1
336 vs. IgG, indicating their requirement for inducing ICB resistance in the context of low
337 *Cdkn2a* expression (**Table S2**). As we observed differences in TME metabolites in
338 *Cdkn2a*^{Low} tumors (**Fig. 3A**), we focused on plasma membrane solute carrier transporters
339 (**Fig. 3C and Table S3**), which play critical roles in metabolite compartmentalization be-
340 tween the intracellular and extracellular space[120]. We cross-compared these genes with
341 depleted analytes in sh*Cdkn2a* TIF (**Fig. 3A**). Using this comparison, we identified zinc
342 and the plasma membrane zinc importer *Slc39a9* as potential drivers of anti-Pd1 re-
343 sistance in sh*Cdkn2a* tumors (**Fig. 3A and Fig. 3C**). Notably, we found that the decrease
344 of zinc in the TIF in sh*Cdkn2a* tumors correspond to increased zinc in cancer cells (**Fig.
345 3D**). Consistently, data mining of scRNA-Seq from melanoma patient specimens showed
346 that *CDKN2A*^{Low} cancer cells have higher zinc scores compared to *CDKN2A*^{High} cancer

347 cells (**Fig. 3E**). Altogether, these data demonstrate that loss of *CDKN2A* in cancer cells

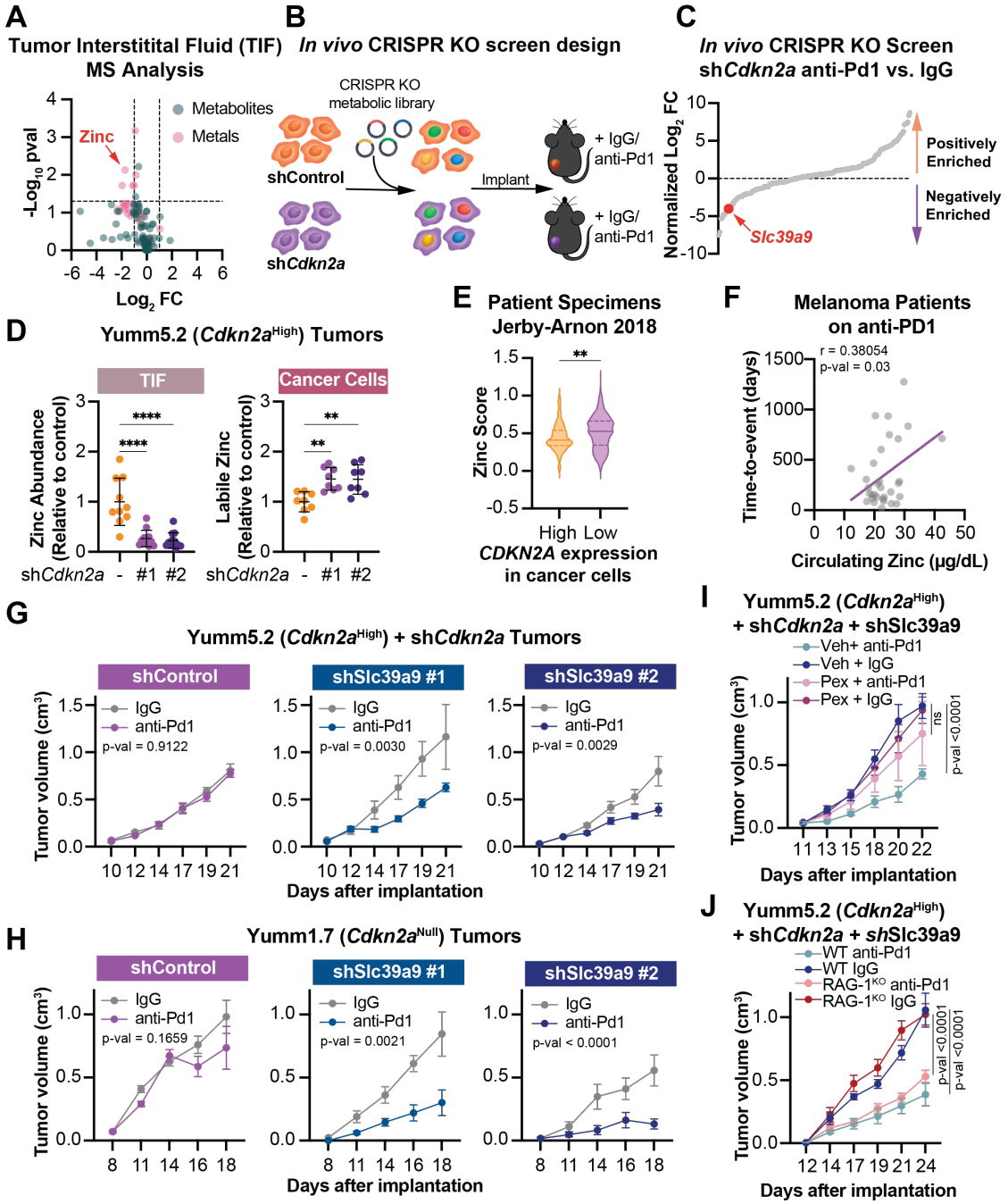

Figure 3. Zinc and Slc39a9 are key determinants of anti-Pd1 response in *Cdkn2a*^{Low} tumors. **(A)** Volcano plot of metabolites and metals in the tumor interstitial fluid (TIF) of tumors derived from Yumm5.2 (*Cdkn2a*^{High}) cells with knockdown of GFP (shControl) or *Cdkn2a* (sh*Cdkn2a*). Metabolites were quantified by liquid chromatography–mass spectrometry (LC-MS) and metals by inductively coupled plasma mass spectrometry (ICP-MS). Data show $\log_2$ fold change (FC) of analytes in sh*Cdkn2a* vs. shControl and corresponding $-\log_{10}$ p-value (FDR-adjusted). **(B)** Schematic of *in*

vivo metabolic CRISPR knockout (KO) screen design. Yumm5.2 (*Cdkn2a*^{High}) cells with knockdown of GFP (shControl) or *Cdkn2a* (sh*Cdkn2a*) were implanted into mice. Mice were treated with IgG or anti-Pd1 (200 µg, i.p., 3×/week). **(C)** Ranked plot of CRISPR KO screen results in tumors (see Schematic in B). Graph is log_2 Fold change (FC) of CRISPR negative scores of plasma membrane solute carrier transporters in sh*Cdkn2a* tumors treated with anti-Pd1 vs. IgG compared to shControl tumors treated with anti-Pd1 vs. IgG (see **Table S1**). **(D)** ICP-MS quantification of total zinc levels in TIF (left) and labile zinc levels in cancer cells (right) from tumors derived from Yumm5.2 (*Cdkn2a*^{High}) cells with knockdown of GFP (shControl) or *Cdkn2a* (sh*Cdkn2a,* hairpins #1 and #2). Data show mean ± SD; one-way ANOVA. **(E)** Violin plot showing the cancer cell zinc score from scRNA-seq of melanoma patient tumors stratified by *CDKN2A* expression in cancer cells. Student's t-test. **(F)** Correlation plot between total zinc levels in plasma (quantified by ICP-MS) and time-to-event outcomes in patients treated with anti-PD1. Pearson correlation. **(G)** Mice were implanted with Yumm5.2 (*Cdkn2a*^{High}) cells with knockdown of *Cdkn2a* in combination with knockdown of GFP (shControl) or Slc39a9 (shSlc39a9, hairpins #1 and #2). Longitudinal tumor growth of mice treated with IgG or anti-Pd1 (200 µg, i.p., 3×/week). Mean ± SEM (n=5/group); mixed-effects model. **(H)** Mice were implanted with Yumm1.7 (*Cdkn2a*^{Null}) cells with knockdown of GFP (shControl) or Slc39a9 (shSlc39a9, hairpins #1 and #2). Longitudinal tumor growth of mice treated with IgG or anti-Pd1 (200 µg, i.p., 3×/week). Mean ± SEM (n=5/group); mixed-effects model. **(I)** Mice were implanted with Yumm5.2 (*Cdkn2a*^{High}) cells with knockdown of *Cdkn2a* in combination with knockdown of GFP (shControl) or Slc39a9 (shSlc39a9). Longitudinal tumor growth of mice treated with pexidartinib (Pex, 45 mg/kg, o.g., 3×/week) or vehicle, and IgG or anti-Pd1 (200 µg, i.p., 3×/week). Data show mean ± SEM (n=6/group); mixed-effects model. **(J)** Wildtype (WT) or B6.129S7-Rag1^tm1Mom^/J (RAG-1^{KO}) mice were implanted with Yumm5.2 (*Cdkn2a*^{High}) cells with knockdown of *Cdkn2a* in combination with knockdown of GFP (shControl) or Slc39a9 (shSlc39a9). Longitudinal tumor growth of mice treated with IgG or anti-Pd1 (200 µg, i.p., 3×/week). Mean ± SEM (n=5/group); mixed-effects model. * $p<0.05$, ** $p<0.01$, *** $p<0.001$, **** $p<0.0001$, ns = not significant.

drives a differential zinc compartmentalization within the tumor, leading to zinc accumulation in cancer cells and concurrent depletion of zinc in the TME. Interestingly, a recent publication demonstrates that cancer patients with elevated serum zinc levels show improved overall survival when undergoing ICB treatment, including anti-PD1[95]. Consistently, we also found that anti-PD1-treated patients with low circulating zinc levels have reduced time-to-event outcomes compared to those with higher zinc levels (**Fig. 3F**), providing support for the role of zinc in ICB response. We validated that the knockdown of Slc39a9 (**Fig. S3B-D**) sensitizes *Cdkn2a*^{Low} tumors to anti-Pd1 treatment in our two models (**Fig. 3G-H**). Importantly, TAM depletion abrogated the anti-Pd1 efficacy following Slc39a9 knockdown (**Fig. 3I**), while there was no difference in anti-Pd1 response in tumors implanted into Rag-1-/- mice (**Fig. 3J**), suggesting that this restored response was

359 dependent on TAMs and not T cells. Altogether, these data demonstrate that Slc39a9 is
360 essential for anti-Pd1 resistance in *Cdkn2a*^{Low} tumors and that TAMs, not T cells, are the
361 primary immune effectors driving anti-Pd1 responses in these tumors. Moreover, these
362 data indicate that zinc compartmentalization between cancer cells and the TME plays a
363 critical role in regulating the anti-Pd1 response.
364

365 ***CDKN2A*^{Low} cancer cells reprogram zinc compartmentalization via plasma mem-**
366 **brane SLC39A9 in a mechanism mediated by cholesterol**

367 Next, we sought to determine how *CDKN2A* regulates zinc homeostasis via SLC39A9.
368 Prior work found that SLC39A9 is localized in the plasma membrane and imports zinc
369 ions from the extracellular space into the cytosol[121-125]. We found that knockdown of
370 *CDKN2A* in multiple human and mouse cancer cell models increased plasma membrane
371 SLC39A9 (**Fig. 4A** and **Fig. S4A-B**), whereas expression of p16 in *Cdkn2a*^{Low} cancer
372 cells decreased plasma membrane Slc39a9 (**Fig. 4B**). Cells with increased plasma mem-
373 brane Slc39a9 had elevated intracellular zinc levels and reduced extracellular zinc levels,
374 an effect that was reversed by knockdown of Slc39a9 in *Cdkn2a*^{Low} cancer cells (**Fig. 4C-**
375 **E** and **Fig. S4C-F**). Importantly, knockdown of Slc39a9 decreased both labile zinc (**Fig.**
376 **4C-E**) and total zinc (**Fig. S4C-F**), where total zinc includes both labile zinc and zinc
377 bound to proteins and other molecules. These findings indicate that Slc39a9 is a key
378 regulator of zinc homeostasis, and that labile zinc quantification is a reliable indicator of
379 zinc content in our model. Consistently, overexpression of wildtype Slc39a9 rescued the
380 intracellular labile zinc defect in Slc39a9 knockdown cells, whereas the putative hypo-
381 morphic mutant Slc39a9^{H156R} [126-128] was less effective in both Yumm5.2 (**Fig. 4F-H**) and

382 Yumm1.7 (**Fig. S4G-I**) cells. Importantly, the decreased zinc uptake in cells expressing

383 the Slc39a9^{H156R} mutant was not due to the inability of the mutant to localize to the plasma

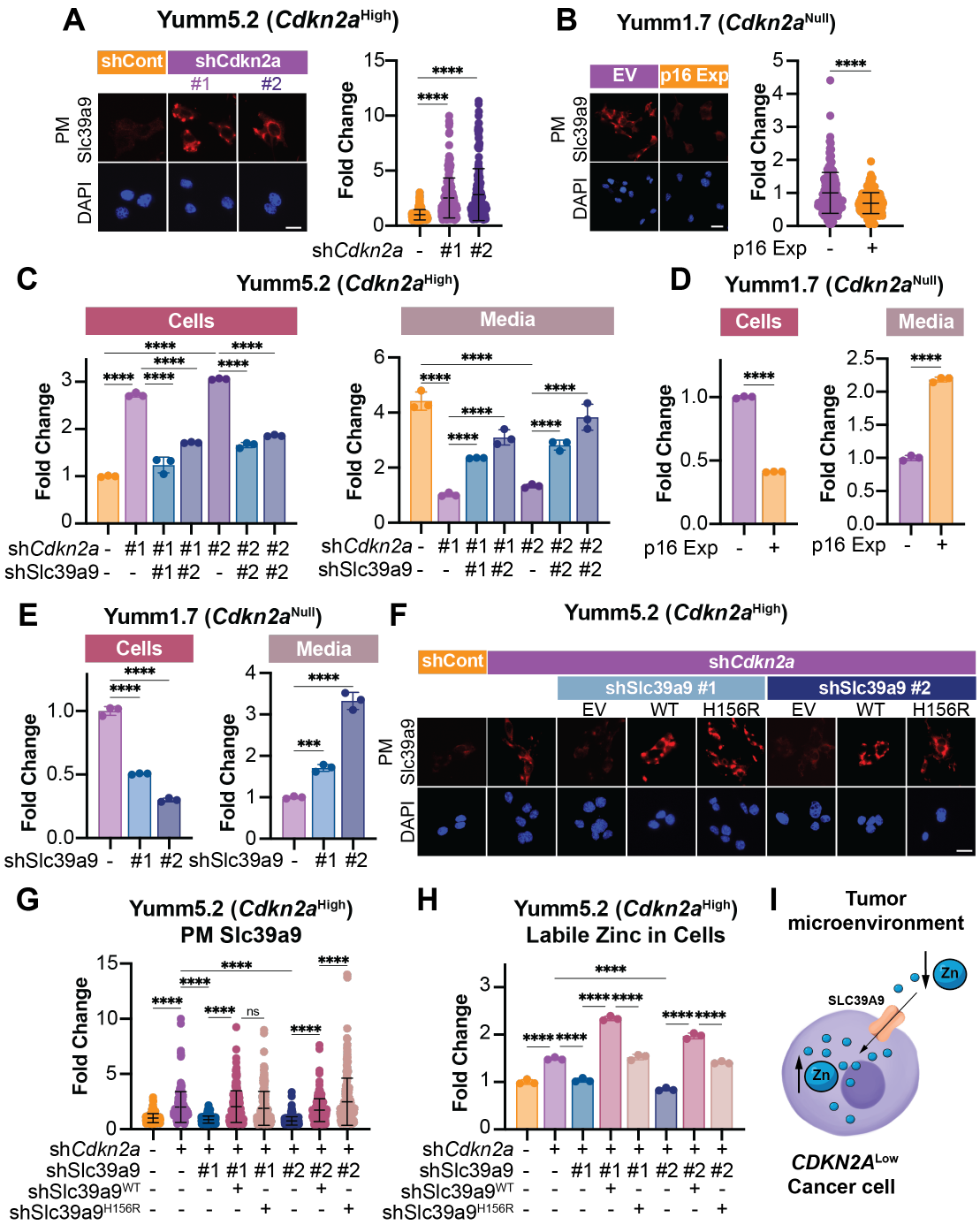

Figure 4. Increased plasma membrane Slc39a9 drives zinc uptake in *Cdkn2a*^{Low} cancer cells. (A-B) Representative images (left) and quantification (right) of Slc39a9 immunofluorescence on non-permeabilized cells to visualize plasma membrane (PM) Slc39a9 in **(A)** Yumm5.2 (*Cdkn2a*^{High}) cells with knockdown of GFP (shControl) or *Cdkn2a* (sh*Cdkn2a,* hairpins #1 and #2) and **(B)**

Yumm1.7 (*Cdkn2a*^{Null}) cells expressing empty vector (EV) or physiological levels of p16 (p16 Exp). Mean ± SD (n=200/group); one-way ANOVA. **(C-E)** Bar graph showing labile zinc quantification in cells (left) and media (right) in **(C)** Yumm5.2 (*Cdkn2a*^{High}) cells with knockdown of GFP (shControl) or *Cdkn2a* (sh*Cdkn2a,* hairpins #1 and #2) in combination with knockdown of GFP (shControl) or Slc39a9 (shSlc39a9, hairpins #1 and #2), **(D)** Yumm1.7 (*Cdkn2a*^{Null}) cells expressing empty vector (EV) or physiological levels of p16 (p16 Exp), and **(E)** Yumm1.7 (*Cdkn2a*^{Null}) cells with knockdown of GFP (shControl) or Slc39a9 (shSlc39a9, hairpins #1 and #2). Mean ± SD; Student's t-test and one-way ANOVA. **(F-H)** Yumm5.2 (*Cdkn2a*^{High}) cells with knockdown of GFP (shControl) or *Cdkn2a* (sh*Cdkn2a,* hairpins #1 and #2) alone or in combination with empty vector (EV) control, wildtype (WT), or hypomorphic mutant (H156R) Slc39a9. **(F)** Representative images of Slc39a9 immunofluorescence on non-permeabilized cells to visualize plasma membrane (PM) Slc39a9. **(G)** Quantification of (F). Mean ± SD (n=200/group); one-way ANOVA. **(H)** Labile zinc quantification in cells. Mean ± SD; one-way ANOVA. **(I)** Schematic of how plasma membrane Slc39a9 compartmentalizes zinc between the cells and the tumor microenvironment. Scale bars = 25μm.* $p<0.05$, ** $p<0.01$, *** $p<0.001$, **** $p<0.0001$, ns = not significant.

membrane (**Fig. 4F-G** and **Fig. S4G-H**). We did not observe a compensatory upregulation of other *Slc39* or *Slc30* genes known to transport zinc upon knockdown of Slc39a9 (**Fig. S4J** and **Table S4**), further confirming Slc39a9 as the key zinc transporter in these cells. Additionally, none of the metal ions commonly transported by SLC39 family members were altered upon knockdown of Slc39a9 (**Fig. S4K**), indicating that the observed changes are not due to differential uptake of other metals. These findings demonstrate that plasma membrane SLC39A9 is a major and specific regulator of zinc compartmentalization between intracellular and extracellular spaces in *CDKN2A*^{Low} cancer cells (**Fig. 4I**).

Finally, we sought to determine the mechanism whereby *Cdkn2a*^{Low} cancer cells have increased plasma membrane Slc39a9. We did not observe differential mRNA expression of *Slc39a9* upon *Cdkn2a* knockdown or p16 expression (**Fig. S5A**). SLC39A9 is a transmembrane protein, which are often anchored to the plasma membrane through cholesterol[129]. Our prior study found that human cells with knockdown of *CDKN2A*/p16 have

399 increased cholesterol[56], a finding we validated in the complementary mouse cell line mod-

400 els used in this study (**Fig. S5B-C**). Thus, we hypothesized that increased cholesterol

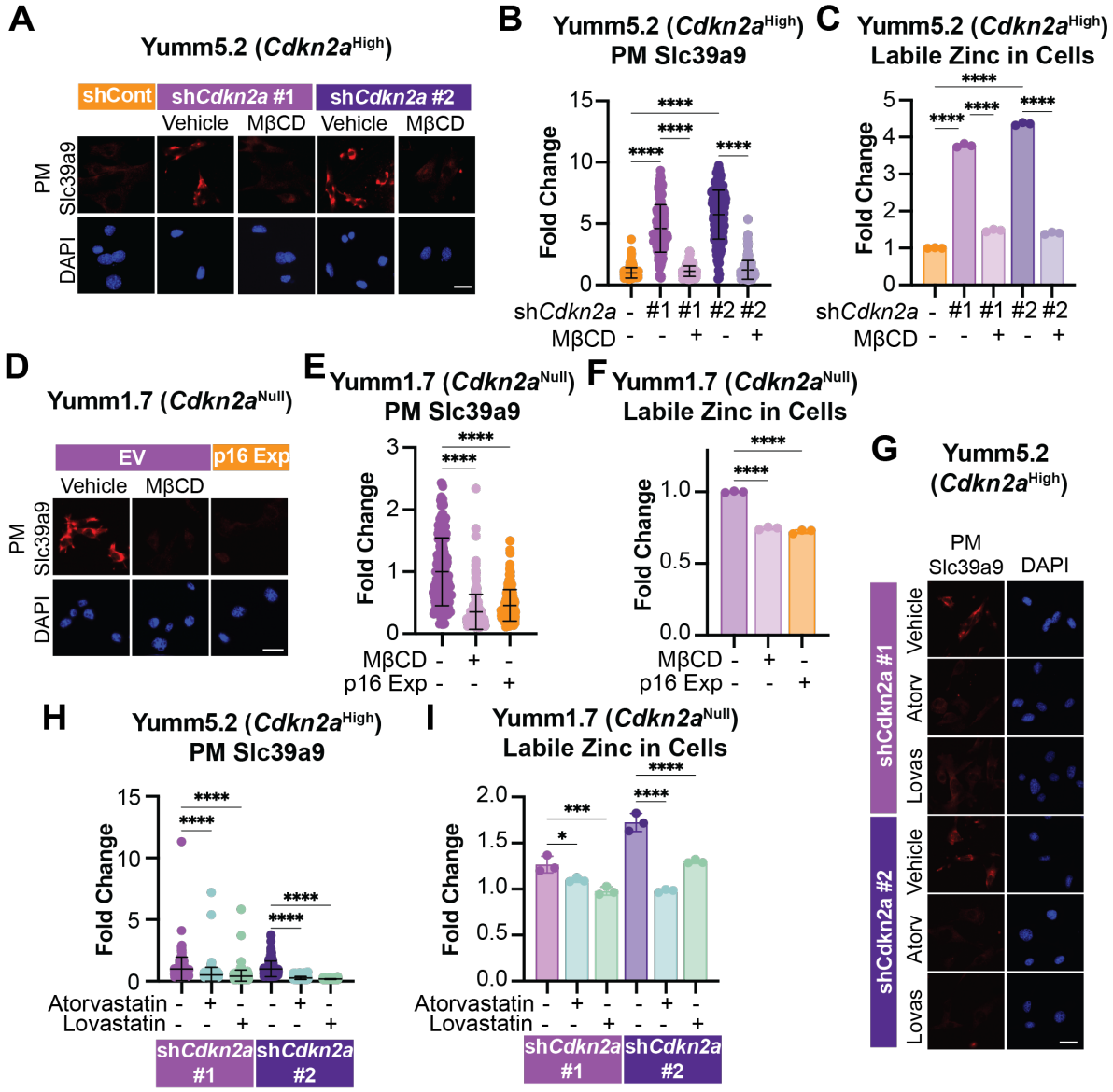

Figure 5. Increased plasma membrane Slc39a9 in *Cdkn2a*^{Low} cancer cells is mediated by cholesterol. (A-C) Yumm5.2 (*Cdkn2a*^{High}) cells with knockdown of GFP (shControl) or *Cdkn2a* (sh*Cdkn2a,* hairpins #1 and #2) were treated with vehicle or Methyl-β-cyclodextrin (MβCD; 10mM, 1h). **(A)** Representative images of Slc39a9 immunofluorescence on non-permeabilized cells to visualize plasma membrane (PM) Slc39a9. **(B)** Quantification of (A). Mean ± SD (n=200/group); one-

way ANOVA. **(C)** Labile zinc quantification in cells. Mean ± SD; one-way ANOVA. **(D-F)** Yumm1.7 (*Cdkn2a*^{Null}) cells expressing empty vector (EV) or physiological levels of p16 (p16 Exp) were treated with vehicle or Methyl-β-cyclodextrin (MβCD; 10mM, 1h). **(D)** Representative images of Slc39a9 immunofluorescence on non-permeabilized cells to visualize plasma membrane (PM) Slc39a9. **(E)** Quantification of (D). Mean ± SD (n=200/group); one-way ANOVA. **(F)** Labile zinc quantification in cells. Mean ± SD; one-way ANOVA. **(G-I)** Yumm5.2 (*Cdkn2a*^{High}) cells with knockdown of *Cdkn2a* (sh*Cdkn2a,* hairpins #1 and #2) were treated with vehicle or the statins atorvastatin (Atov, 1μM, 4 days) or lovastatin (Lovas,1μM, 4 days). **(G)** Representative images of Slc39a9 immunofluorescence on non-permeabilized cells to visualize plasma membrane (PM) Slc39a9, **(H)** Quantification of (G). Mean ± SD (n=200/group); one-way ANOVA. **(I)** Labile zinc quantification in cells. Mean ± SD; one-way ANOVA. Scale bars = 25μm.* $p<0.05$, ** $p<0.01$, *** $p<0.001$, **** $p<0.0001$, ns = not significant.

levels in *CDKN2A*^{Low} cancer cells may enhance plasma membrane SLC39A9 accumulation. Consistent with this hypothesis, depleting plasma membrane cholesterol with methyl-β-cyclodextrin (MβCD)[130,131] or inhibiting *de novo* cholesterol synthesis using statins reduced plasma membrane Slc39a9 levels and decreased intracellular labile zinc in *Cdkn2a*^{Low} cancer cells (**Fig. 5A-I**). Altogether, these data demonstrate that *Cdkn2a*^{Low} cancer cells increase intracellular zinc via increased cholesterol-mediated plasma membrane Slc39a9.

Competition for zinc between *Cdkn2a*^{Low} cancer cells and TAMs regulates phagocytosis and anti-Pd1 response

We found that *CDKN2A*^{Low} tumors do not respond to anti-PD1 treatment (**Fig. 1A–C**), and that macrophages are less phagocytic when exposed to *Cdkn2a*^{Low} cancer cells, both *in vitro* (**Fig. 2H**) and *in vivo* (**Fig. 2C–D** and **F-G**). We also found that *Cdkn2a*^{Low} cancer cells deplete microenvironmental zinc through zinc uptake via increased Slc39a9 at the plasma membrane (**Fig. 4C-E and Fig. S4C-F**) and that knockdown of Slc39a9 in *Cdkn2a*^{Low} cells restores anti-Pd1 response (**Fig. 3G–H**). Thus, we hypothesized that the availability of zinc in the TME may play a direct role in TAM phagocytosis. Analysis of

418 publicly available scRNA-seq data from melanoma and HNSCC patients showed that
419 TAMs in *CDKN2A*^{Low} tumors have lower zinc scores and that zinc scores positively cor-
420 relate with phagocytosis scores (**Fig. 6A** and **Fig. S6A**). Moreover, further analysis of our
421 scRNA-Seq data from Yumm5.2 tumors demonstrated that TAMs in *Cdkn2a*^{Low} tumors,
422 which have low phagocytic activity (**Fig. 2C**), also have decreased zinc scores (**Fig. S6B**).
423 Consistently, *in vivo* validation demonstrated that TAMs in tumors derived from *Cdkn2a*^{Low}
424 cancer cells have reduced zinc levels (**Fig. 6B** and **Fig. S6C**), and zinc levels positively
425 correlate with phagocytosis (**Fig. 6B** and **Fig. S6D**). Moreover, we found that RAW264.7
426 macrophages with higher intracellular zinc have greater phagocytic activity *in vitro* (**Fig.**
427 **S6E**). Strikingly, while anti-Pd1 treatment increased the expression of phagocytosis-re-
428 lated genes in RAW264.7 macrophages *in vitro*, this effect was further amplified by zinc
429 supplementation and suppressed by zinc chelation (**Fig. S6F**). These data demonstrate
430 that zinc availability indeed modulates anti-Pd1-mediated macrophage phagocytosis.
431
432 We found that knockout or knockdown of the zinc importer Slc39a9 restores anti-Pd1
433 response in *Cdkn2a*^{Low} tumors (**Fig. 3C, 3G-H**) and that increased intracellular zinc in
434 macrophages correlates with enhanced phagocytosis in human melanoma and HNSCC
435 patients (**Fig. 6A** and **Fig. S6A**). A recent publication found that increased metal signa-
436 tures in TAMs, mainly genes related to zinc function, correlate with improved ICB re-
437 sponses in patients[30]. Additionally, both published data[95] and our data (**Fig. 3F**) show that
438 patients with higher circulating zinc levels show improved outcomes on anti-PD1 therapy.
439 Thus, we aimed to determine whether zinc depletion in the TME, driven by Slc39a9 in
440 *Cdkn2a*^{Low} cancer cells, impairs TAM zinc content and phagocytosis. To test this, we

knocked down Slc39a9 in fluorophore-labeled Yumm5.2 *Cdkn2a*^{Low} cancer cells and implanted them into mice (**Fig. 2E**). Slc39a9 knockdown restored TAM phagocytosis upon

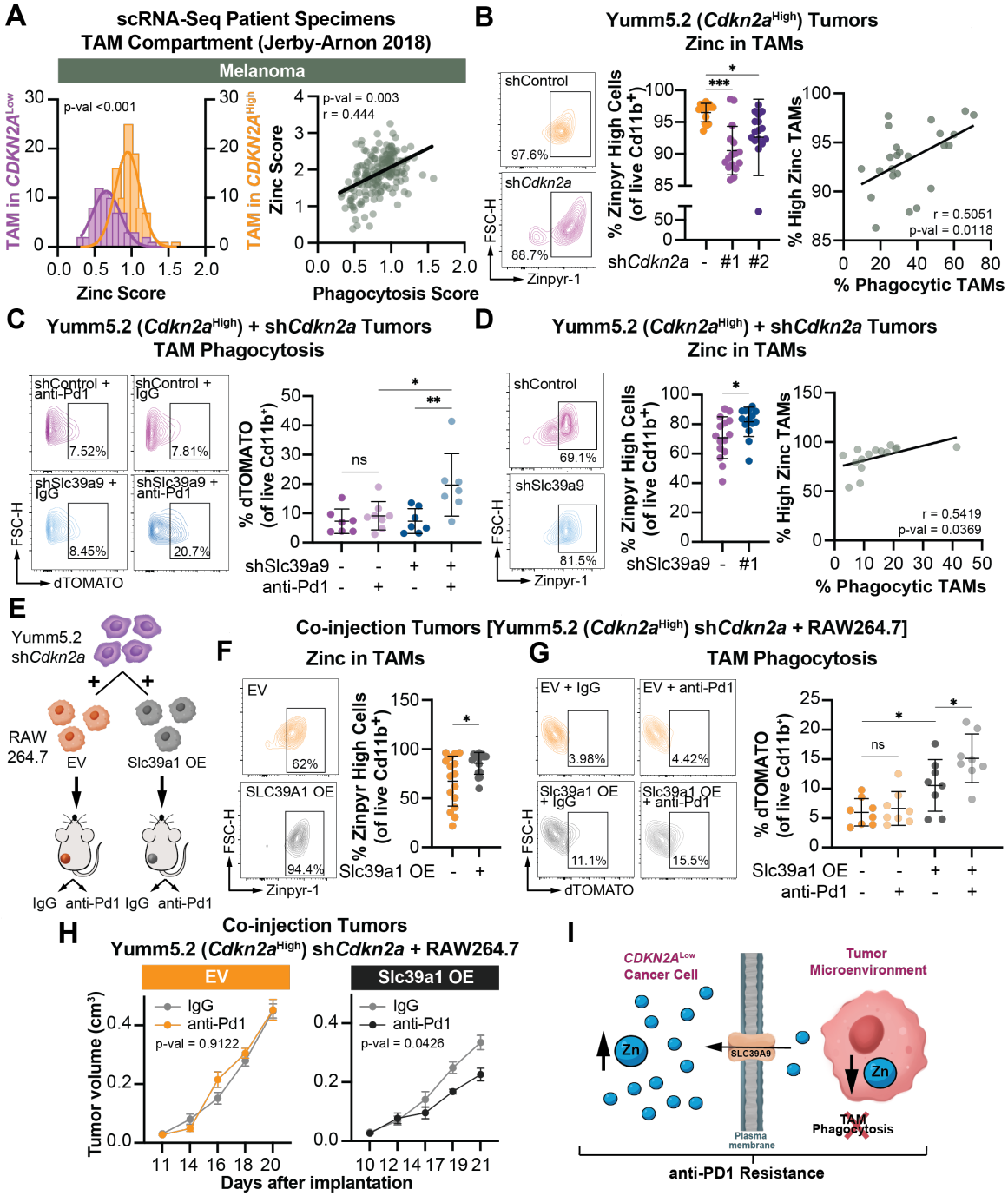

Figure 6. Reduced zinc availability to TAMs in *Cdkn2a*^{Low} tumors suppresses anti-Pd1-driven phagocytosis. (A) scRNA-Seq dataset from melanoma patients stratified by *CDKN2A* expression in cancer cells. Histogram showing the zinc score in TAMs from the indicated scRNA-Seq datasets from melanoma patients stratified by *CDKN2A* expression in cancer cells (left) and zinc score correlation with phagocytic score (right). Linear mixed models and Pearson correlation. **(B)** Mice were implanted with dTOMATO-labeled Yumm5.2 (*Cdkn2a*^{High}) cells with knockdown of GFP (shControl) or *Cdkn2a*

(sh*Cdkn2a,* hairpins #1 and #2). Representative labile zinc flow cytometry plots in TAMs (left), quantification of labile zinc in TAMs (center), and correlation between labile zinc and phagocytosis in TAMs (right). Mean ± SD; one-way ANOVA and Pearson correlation. **(C-D)** Mice were implanted with dTOMATO-labeled Yumm5.2 (*Cdkn2a*^{High}) cells with knockdown of *Cdkn2a* (sh*Cdkn2a*) alone or in combination with knockdown of GFP (shControl) or Sl39a9 (shSlc39a9). **(C)** Representative flow cytometry plots of TAM phagocytosis (left) and quantification of TAM phagocytosis (right). Mean ± SD; one-way ANOVA. **(D)** Representative labile zinc flow cytometry plots in TAMs (left), quantification of labile zinc in TAMs (center), and correlation between labile zinc and phagocytosis in TAMs (right). Mean ± SD; one-way ANOVA and Pearson correlation. **(E)** Schematic of macrophage co-injection model. **(F-H)** RAW264.7 macrophages expressing empty vector (EV) control or Slc39a1 (Slc39a1 OE) were co-injected in immunocompromised NSG mice with Yumm5.2 (*Cdkn2a*^{High}) cells with knockdown of *Cdkn2a* (shCdkn2a) at a ratio of 1:10. Mice were treated with IgG or anti-Pd1 (200 µg, i.p., 3×/week). **(F)** Representative flow cytometry plots (left) and quantification (right) of labile zinc in TAMs. Mean ± SD; Student's t-test. **(G)** Representative flow cytometry plots (left) and quantification (right) of the percentage of TAMs with dTOMATO signal (phagocytic TAMs). Mean ± SD; one-way ANOVA. **(H)** Longitudinal tumor growth. Mean ± SEM (n=8/group); mixed-effects model. **(I)** Schematic of zinc competition between *CDKN2A*^{Low} cells and TAMs, leading to decreased phagocytosis and anti-PD1 resistance. * $p<0.05$, ** $p<0.01$, *** $p<0.001$, **** $p<0.0001$, ns = not significant.

443 anti-Pd1 (**Fig. 6C**), corresponding with increased zinc in TAMs (**Fig. 6D**). Altogether,
444 these data indicate that Slc39a9-mediated zinc sequestration by cancer cells directly im-
445 pairs TAM function in response to anti-Pd1. We did not observe consistent expression
446 differences in "eat me" or "don't eat me" signals in *Cdkn2a*^{Low} cells with or without Slc39a9
447 knockdown (**Fig. S6G** and **Table S5**), nor did we detect changes in Pd-l1 expression on
448 cancer cells (**Fig. S6H-I**), indicating that the observed changes in TAM phagocytosis and
449 anti-Pd1 response is macrophage-intrinsic. Finally, to demonstrate that increased zinc in
450 macrophages directly increases phagocytosis *in vivo*, we engineered RAW264.7 macro-
451 phages that have the ability to compete for TME zinc by overexpressing the zinc importer
452 Slc39a1 (**Fig. S6J**). Indeed, these macrophages are able to increase intracellular zinc *in*
453 *vitro* (**Fig. S6K**). We then co-implanted these zinc-replete macrophages with Yumm5.2
454 sh*Cdkn2a* cells in immunodeficient NSG mice (**Fig. 6E**). TAMs in tumors co-implanted
455 with Slc39a1-overexpressing macrophages had higher intracellular zinc (**Fig. 6F**). Excit-
456 ingly, upon anti-Pd1 treatment, these TAMs had increased phagocytic activity (**Fig. 6G**),

457 which was associated with reduced tumor volume (**Fig. 6H**). Together, our data demon-
458 strate that zinc is critical for TAM phagocytosis and that zinc-replete TAMs respond to
459 anti-Pd1 by increasing their phagocytic gene expression and activity. Thus, increased
460 zinc uptake by *Cdkn2a*^{Low} cancer cells impairs TAM phagocytosis by outcompeting mac-
461 rophages for zinc, corresponding to anti-Pd1 resistance (**Fig. 6I**).
462

463 **High zinc diet combined with anti-Pd1 decreases tumor burden and enhances TAM**
464 **phagocytosis in *Cdkn2a*^{Low} tumors**

465 Finally, we aimed to find a manner to exploit our discoveries to improve anti-Pd1 treat-
466 ment in *Cdkn2a*^{Low} tumors. We found that *Cdkn2a*^{Low} cancer cells deplete the TME of zinc
467 by upregulating plasma membrane Slc39a9 (**Fig. 4A-E** and **Fig. S4C-F**), therefore out-
468 competing TAMs for zinc (**Fig. 6B-D**). We also found that engineering TAMs that have an
469 enhanced ability to compete for zinc uptake have increased phagocytosis (**Fig. 6E-H**).
470 Since there are no available inhibitors for SLC39A9, we hypothesized that increasing di-
471 etary zinc would raise zinc levels in the TME to restore zinc within TAMs and promote an
472 anti-Pd1 response. Excitingly, a high zinc diet (~3X higher than normal chow) significantly
473 elevated TME zinc levels (**Fig. 7A-B**), which corresponded to decreased tumor volume in
474 *Cdkn2a*^{Low} tumors upon anti-Pd1 treatment (**Fig. 7C-D and Fig. S7A**). The dietary inter-
475 vention did not significantly affect food intake or body weight (**Fig. S7B-C**) nor did it mark-
476 edly alter tumor growth in the IgG control treatment group (**Fig. S7D**). Similar to
477 *Cdkn2a*^{Low} tumors with Slc39a9 knockdown (**Fig. 3I**), TAM depletion abrogated this anti-
478 Pd1 response (**Fig. 7E**), indicating that TAMs are essential for the anti-Pd1 response of
479 *Cdkn2a*^{Low} cancer cells on a high zinc diet. Excitingly, we confirmed that the high zinc diet

480 increased TAM zinc levels (**Fig. 7F** and **Fig. S7E**), and these zinc-replete TAMs had en-

481 hanced phagocytic activity following anti-Pd1 treatment (**Fig. 7G** and **Fig. S7F**). Similar

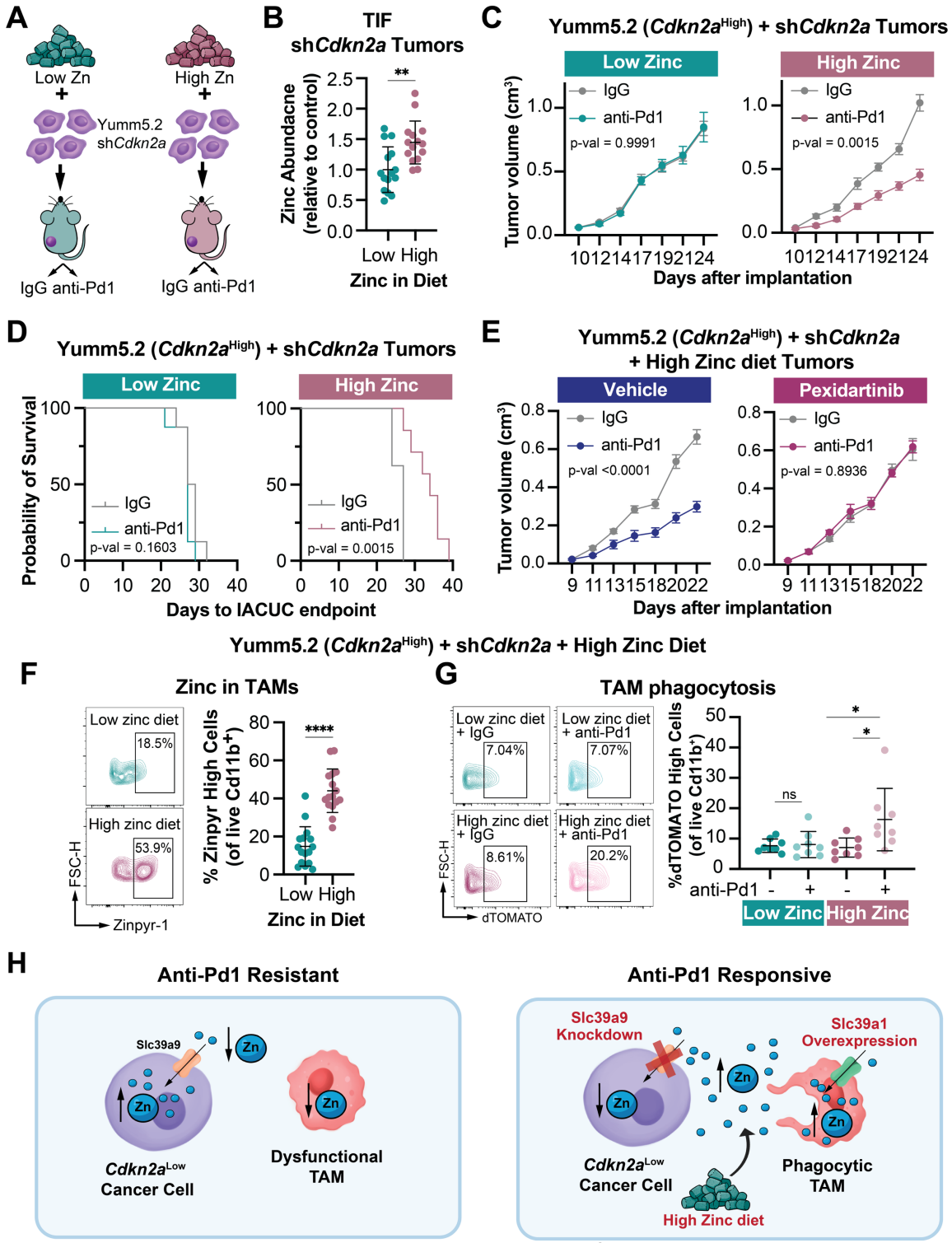

Figure 7. Replenishing TME zinc via the diet in *Cdkn2a*^{Low} tumors re-educates TAMs and promotes anti-Pd1-mediated phagocytosis. (A) Schematic of diet study. **(B-D)** Mice were

assigned to low (55 mg/kg) or high (300 mg/kg) zinc diets, implanted with Yumm5.2 (*Cdkn2a*^{High}) cells with knockdown of *Cdkn2a* (sh*Cdkn2a*), and treated with IgG or anti-Pd1 (200 µg, i.p., 3×/week). **(B)** Dot plot showing total levels of zinc in the tumor interstitial fluid (TIF) quantified by ICP-MS. Mean ± SD; student's t-test. **(C)** Longitudinal tumor growth. Mean ± SEM (n=8/group); mixed-effects model. **(D)** Kaplan-Meier plot depicting survival analysis. Log-rank (Mantel-Cox) test. **(E)** Mice fed a high (300 mg/kg) zinc diet were implanted with Yumm5.2 (*Cdkn2a*^{High}) cells with knockdown of *Cdkn2a* (sh*Cdkn2a*). Mice were treated with Pexidartinib (45 mg/kg, o.g., 3×/week) or vehicle in combination with IgG or anti-Pd1 (200 µg, i.p., 3×/week). Longitudinal tumor growth. Mean ± SEM (n=8/group); mixed-effects model. **(F-G)** Mice were assigned to a high (300 mg/kg) zinc diet, implanted with Yumm5.2 (*Cdkn2a*^{High}) cells with knockdown of *Cdkn2a* (shCdkn2a), and treated with IgG or anti-Pd1 (200 µg, i.p., 3×/week). **(F)** Representative flow cytometry plots (left) and quantification (right) of labile zinc in TAMs. Mean ± SD; student's t-test. **(G)** Representative flow cytometry plots (left) and quantification (right) of the percentage of TAMs with dTOMATO signal (phagocytic TAMs). Mean ± SD; one-way ANOVA. **(H)** *Cdkn2a*^{Low} cancer cells sequester TME zinc via increased plasma membrane Slc39a9, leading to macrophage dysfunction and anti-Pd1 resistance. Replenishment of TME zinc via knockdown of Slc39a9 in cancer cells, overexpression of Slc39a1 in co-implanted macrophages, or high zinc diet increases intracellular zinc in macrophages priming their phagocytic activity to respond to anti-Pd1. * $p<0.05$, ** $p<0.01$, *** $p<0.001$, **** $p<0.0001$, ns = not significant.

482 to our findings with knockdown of Slc39a9 (**Fig. S6I**), the observed increase in TAM phag-
483 ocytosis was independent of changes in Pd-l1 expression on cancer cells (**Fig. S7G**),
484 further confirming that TAM phagocytosis and decreased tumor burden upon anti-Pd1
485 treatment is macrophage-intrinsic. Taken together, these findings support the notion that
486 replenishing the TME with zinc via a dietary intervention can reverse anti-Pd1 resistance
487 in *Cdkn2a*^{Low} tumors, which is associated with an enhanced TAM phagocytotic response
488 (**Fig. 7H**).

489 **DISCUSSION**

490

491 The role of *CDKN2A* as a critical regulator of the cell cycle has been well established for
492 >30 years[51,132]. However, accumulating evidence from our lab and others has revealed
493 that *CDKN2A*/p16 loss has non-canonical pro-tumorigenic functions that extend beyond
494 its role in cell cycle control, including in metabolism[133]. Moreover, there is recent evidence
495 that nutrient competition within the TME can affect immune cell activity and function[134-
496 137], although how the micronutrient zinc is compartmentalized within cancer and immune
497 cells has never been explored. Here, we demonstrate that loss of *CDKN2A* in cancer cells
498 enhances zinc uptake through upregulation of the SLC39A9 transporter at the plasma
499 membrane, a process that is mediated by cholesterol. The increased zinc uptake by
500 *Cdkn2a*^{Low} cancer cells leads to a zinc-depleted TME, impairing TAM phagocytic activity
501 and diminishing the efficacy of anti-Pd1 treatment. Our findings underscore the critical
502 role of *CDKN2A*/p16 expression in modulating the immune response through zinc,
503 demonstrate an anti-tumorigenic role for zinc-replete TAMs, and open up new therapeutic
504 possibilities through dietary interventions. Moreover, given that the effects we observed
505 were T cell-independent, and that many human tumors are myeloid-rich and T cell-
506 poor[106], our data provide compelling evidence that elevating TME zinc could sensitize
507 tumors that have generally been considered anti-PD1 refractory.

508

509 Our studies and others have shown that suppression of *CDKN2A*/p16 correlates with re-
510 duced expression of pro-inflammatory factors across various diseases, including can-
511 cer[18,63,138-142]. Consistently, *CDKN2A*^{Low} tumors exhibit 'cold' immune phenotypes with

512 reduced immune infiltration, which has been linked to the observed resistance to ICB[1-
513 5,11,143-146]. Excitingly, our findings reveal that TAMs, rather than T cells, are the critical
514 immune cell promoting the response to anti-PD1 in *CDKN2A*^{Low} tumors (**Fig. 3I-J**). In this
515 regard, a small but growing body of literature suggests that patients with T cell-poor tu-
516 mors can still benefit from ICB, potentially through effects on other immune cell popula-
517 tions[25-27]. Consistent with this, our analysis shows that around 20% of patients with mye-
518 loid-rich, T cell-poor tumors exhibit clinical benefit from anti-PD1 therapy beyond 20
519 months, and >7% continue to benefit beyond 30 months (**Fig. 1G**). Recent studies have
520 shown that certain myeloid cells, including TAMs, can directly respond to anti-PD1 and
521 contribute to therapeutic efficacy[28-35]. Using myeloid-rich, T cell-poor models, we found
522 that *Cdkn2a*^{Low} murine tumors have increased TAMs (**Fig. 3A**), consistent with prior re-
523 ports in human patients[1,5]. However, while other research focused on the macrophage
524 polarization status[1,3,6], here we found that *CDKN2A*^{Low} cancer cells modulate TAM phag-
525 ocytic activity (**Fig. 2F-H**). This paradigm shift underscores the critical importance of stud-
526 ying TAM activity, not simply polarization status or macrophage markers, in the context
527 of ICB treatment to improve anti-tumor efficacy. Our results also give rise to the intriguing
528 possibility that myeloid-rich, T cell-poor tumors, which have typically been considered re-
529 fractory to ICB, can be sensitized by reprogramming TAMs to a more phagocytic pheno-
530 type.
531
532 Previous research indicates that TAMs can directly respond to ICB in part by enhancing
533 phagocytosis[28,29,35]. Additionally, a recent pan-cancer study in patient samples identified
534 a subgroup of TAMs that upregulate zinc-binding metallothioneins (named *metalloMac*)

535 that are enriched in ICB-responsive patients[30]. This is consistent with our data demon-
536 strating that elevated zinc in TAMs boosts the response to anti-Pd1 (**Fig. 6G-H**). Indeed,
537 zinc has been previously shown to enhance phagocytosis capacity and/or pathogen clear-
538 ance[68-70,147-150], although none of this work is in cancer and the mechanism is not well
539 understood. Here we found that there is a correlation between the amount of intracellular
540 zinc in TAMs and their phagocytic activity in both *in vivo* tumor models and human tumors
541 (**Fig. 6A-B**, **6D** and **Fig. S6A, S6D**). Moreover, zinc supplementation enhanced the ex-
542 pression of phagocytosis-related genes in macrophages treated with anti-Pd1 *in vitro*, an
543 effect that was abolished by zinc chelation (**Fig. S6F**). The human genome encodes over
544 700 zinc-finger proteins, the largest class of putative transcription factors[151], and prior
545 research has explored whether intracellular zinc levels directly influence gene transcrip-
546 tion[152]. Future studies will investigate the specific transcription factors that drive macro-
547 phage phagocytic activity in response to zinc replenishment. Collectively, our findings
548 underscore the critical role of TAM zinc metabolism in modulating the efficacy of anti-PD1
549 therapy, particularly in the context of *CDKN2A*^{Low} tumors where zinc homeostasis within
550 the TME is disrupted. This study also highlights the potential for boosting zinc metabolism
551 in TAMs as a strategy to enhance the therapeutic response to anti-PD1 in cancer patients,
552 regardless of T cell infiltration.
553
554 Our study demonstrates that *CDKN2A*/p16 itself drives inherent resistance to anti-PD1.
555 There are a handful of prior reports linking loss of *CDKN2A* expression, or 9p21 deletion,
556 with changes in anti-tumor immunity and ICB response[1-18]. Here, we found that *Cdk2na*,
557 and more specifically p16 alone, can drive differential anti-PD1 responses (**Fig. 1B-C**).

558 Consistent with our findings, an integrated analysis of immunogenomic and clinical data
559 from over 1000 patients across 8 solid tumors demonstrated that 9p21 deletions, specif-
560 ically encompassing *CDKN2A* and *MTAP*, were associated with decreased tumor im-
561 mune responses and resistance to anti-PD1 or anti-PD-L1 monotherapy[1]. In contrast, a
562 prior study using cells with different 9p21 deletions showed deletions involving only the
563 *CDKN2A* gene did not affect the response to anti-CTLA4[104]. This discrepancy may arise
564 from differences in the models and immunotherapies used. Despite these insights, routine
565 assessment of *CDKN2A*/p16 expression remains uncommon in clinical practice, except
566 in specific cases such as HPV-positive tumors or when germline alterations are sus-
567 pected, particularly in individuals with a family history of melanoma and/or pancreatic
568 cancer[153-155]. Together with the prior research, our work provides compelling evidence for
569 the need to routinely assess *CDKN2A* status in cancer diagnostics, particularly as our
570 research suggests that treatment outcomes of patients harboring *CDKN2A*^{Low} tumors may
571 be improved by combining ICB therapy with dietary zinc supplementation.
572
573 *CDKN2A* has non-canonical roles in intracellular metabolism[54,55,58,59,117-119], and we em-
574 phasize here a role for *CKDN2A* in influencing metabolites within the TME. Specifically,
575 we found that *CDKN2A*^{Low} cancer cells sequester zinc from the TME (**Fig. 4**), reducing
576 macrophage phagocytic activity during anti-Pd1 treatment (**Fig. 6C-D** and **Fig. S6C-D**),
577 thereby diminishing the therapeutic response (**Fig. 3G-H**). Zinc is an essential micronu-
578 trient critical for the proper functioning of cells. For example, zinc deficiency impairs im-
579 mune cell activity, while zinc supplementation can either restore normal function in defi-
580 cient cells or enhance immune responses in healthy cells[156]. Despite decades of research

581 on zinc's role in cancer, its biological effects remain poorly understood and are often con-
582 tradictory[157]. These inconsistencies stem in part from a historical focus on systemic zinc
583 levels, which overlook the intricate regulation and compartmentalized distribution of zinc
584 within the TME. In this study, we found that increased intracellular zinc in *CDKN2A*^{Low}
585 cancer cells was mediated by a significant upregulation of the zinc transporter SLC39A9
586 at the plasma membrane (**Fig. 4**). Upregulation of plasma membrane Slc39a9 was regu-
587 lated by *de novo* cholesterol synthesis (**Fig. 5**), which we have previously found to be
588 elevated in sh*CDKN2A*/shp16 cells[117] (**Fig. S5B-C**)**.** Interestingly, several epidemiological
589 studies have shown a strong correlation between statin use—drugs that lower choles-
590 terol—and improved response to ICB in cancer patients[158-163]. Our data suggest that this
591 effect may be mediated, at least in part, by reduced plasma membrane Slc39a9 expres-
592 sion in cancer cells (**Fig. 4-5**), thereby increasing zinc availability for immune cells. Future
593 studies will be needed to determine the extent to which the ICB benefit observed in statin-
594 treated patients is driven by altered zinc compartmentalization via SLC39A9. Moreover,
595 these results contribute to the growing body of research highlighting the critical role of
596 metabolite compartmentalization within the TME[134,136,164,165] and underscores the limita-
597 tions of systemic zinc-level assessments in evaluating zinc's role in cancer.
598
599 Zinc can be modulated by the diet, and prior work has associated high dietary zinc intake
600 with improved cancer outcomes or decreased risk[166-171]. However, others report ad-
601 verse[172-175] or neutral effects[176-179]. Here, we found that high dietary zinc effectively in-
602 creases the zinc content in the TME and improves ICB response of *Cdkn2a*^{Low} tumors
603 (**Fig. 7**). This increase in zinc in the diet is ~3X more than the normal chow. The

604 recommended daily allowance (RDA) of zinc is 8 mg for adult women and 11 mg for adult
605 men[180]. Assuming similar zinc metabolism between humans and mice, this increase in
606 dietary zinc is equivalent to a 30 mg zinc supplement, which is available over-the-counter.
607 Future studies are required to explore the potential benefits of combining ICB with this
608 highly accessible and cost-effective zinc supplementation for patients with *CDKN2A*^{Low}
609 tumors. In contrast to our study, a recent article found that high dietary zinc promoted
610 tumor progression in a B16F10 melanoma model by increasing regulatory T cells[98]. These
611 differences are likely due to the amount of zinc in the diet (300mg/kg in our study vs.
612 80mg/kg in[98]), delivery method, or other context-dependent differences. Indeed, 80 mg/kg
613 is below our normal chow levels, suggesting that this study did not achieve high enough
614 intratumoral zinc levels to restore zinc in TAMs and enhance their phagocytosis. None-
615 theless, these discrepancies underscore the importance of considering tumor-specific
616 factors, zinc delivery methods, and bioavailability when exploring zinc-based therapies.
617 In this regard, our data show that the high zinc diet used in this study effectively increases
618 zinc levels not only in the TME (**Fig. 7B**), but also in intratumoral macrophages (**Fig. 7F**).
619 Although we found that replenishing the TME with zinc enhances TAM zinc content and
620 phagocytic activity in C*dkn2a*^{Low} tumors, the role of increased intracellular zinc in
621 *CDKN2A*^{Low} cancer cells remains unclear. The literature reports both pro-tumorigenic[181-
622 183] and cytotoxic[184-187] effects of high intracellular zinc in cancer cells. Thus, it is interest-
623 ing to speculate that zinc may have pleiotropic roles within cancer cells similar to that
624 observed for ROS[188], where excessively high levels are detrimental, but moderate to high
625 levels promote tumorigenesis. Further research is needed to determine the intracellular
626 mechanisms of zinc in C*DKN2A*^{Low} cancer cells.

627

628 In conclusion, the TME represents a competitive environment where access to nutrients,
629 such as zinc, critically shapes the dynamics between tumor and immune cells. Our find-
630 ings demonstrate that suppression of *Cdkn2a* confers the ability to deplete zinc from the
631 TME by upregulating the Slc39a9 importer, impairing TAM function, and reducing the
632 efficacy of anti-Pd1 therapy irrespective of T cells. This study highlights a previously un-
633 recognized role of *CDKN2A* in maintaining a balanced TME metabolism that supports
634 immune activity and therapeutic responses. Our results also emphasize that, in certain
635 contexts, T cells are dispensable for an anti-PD1 response. In summary, our results iden-
636 tify an unexpected role for *CDKN2A* as a master regulator of zinc homeostasis, which
637 impacts the TME and anti-PD1 therapy through a T cell-independent mechanism. These
638 results have major implications not only for understanding novel roles for *CDKN2A* out-
639 side of the cell cycle, but also in underscoring the anti-tumorigenic potential of TAMs that
640 can be harnessed for improved ICB response.

641 **SUPPLEMENTAL FIGURES**

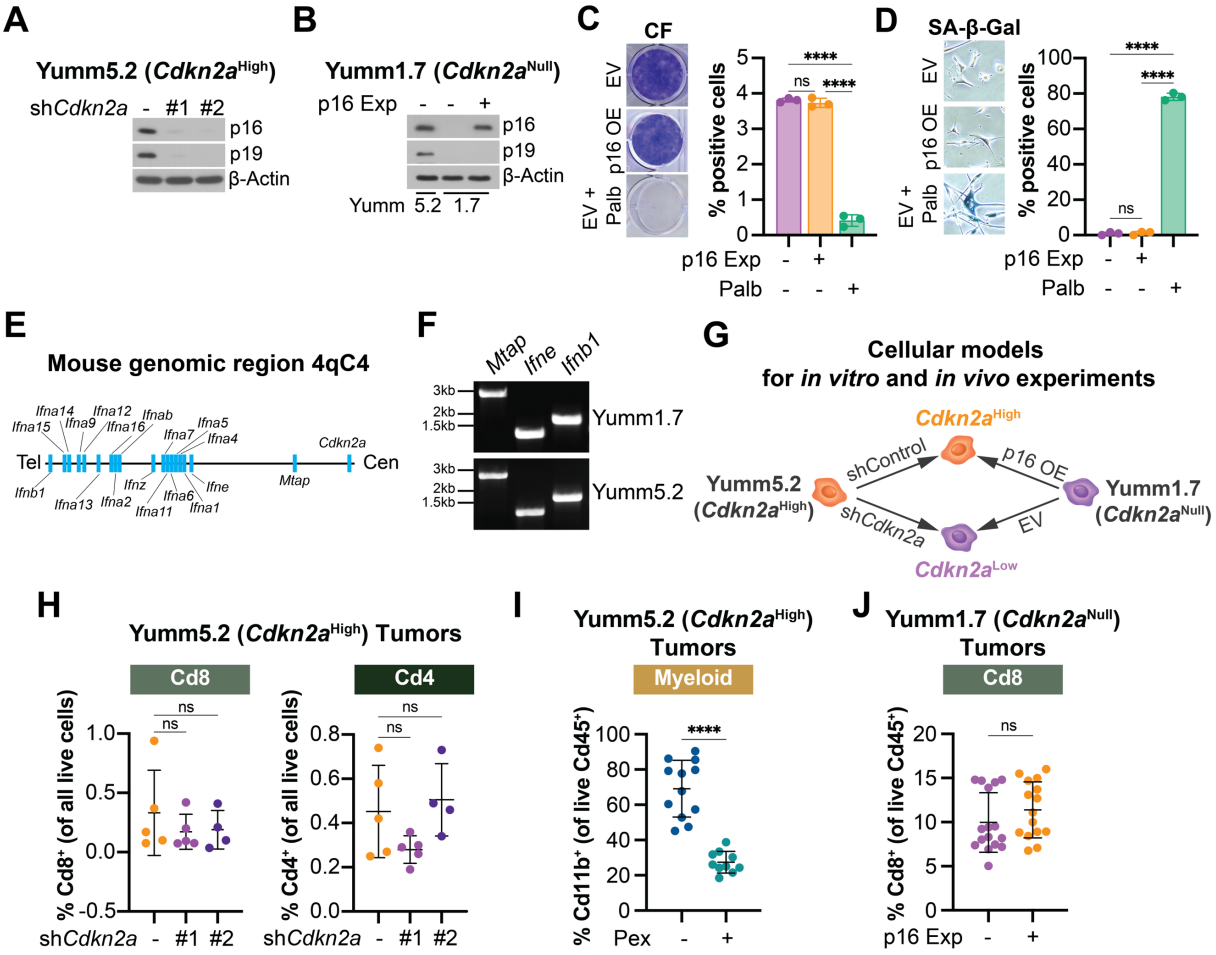

Figure S1. Cellular models used in this study. Related to Figure 1. (A-B) Immunoblot analysis of p16 and p19 in **(A)** Yumm5.2 (*Cdkn2a*^{High}) with knockdown of GFP (shControl) or *Cdkn2a* (sh*Cdkn2a* hairpins #1 and #2) cells and **(B)** Yumm1.7 (*Cdkn2a*^{Null}) cells expressing empty vector (EV) control of physiological levels of p16 (p16 Exp). β-Actin was used as a loading control. **(C-D)** Yumm1.7 (*Cdkn2a*^{Null}) cells expressing empty vector (EV) control of physiological levels of p16 (p16 Exp). Induction of cellular senescence with palbociclib (Palb; 3μM, 10 days) was used as a positive control. **(C)** Representative images of colony formation (CF) assay (left) and quantification (right). Mean ± SD; one-way ANOVA. **(D)** Representative images of senescence-associated β-Galactosidase (SA-β-Gal) activity (left) and quantification (right). Mean ± SD; one-way ANOVA. **(E)** Schematic representation of the murine 4qC4 genomic region containing the *Cdkn2a* gene and gene neighbors. **(F)** Genomic DNA PCR amplification of indicated genes in Yumm1.7 and Yumm5.2 cell lines. **(G)** Schematic of cellular models. **(H)** Quantification of Cd8$^+$ (left) and Cd4$^+$ (right) T cells in tumors derived from Yumm5.2 (*Cdkn2a*^{High}) cells with knockdown of GFP (shControl) or *Cdkn2a* (sh*Cdkn2a*, hairpins #1 and #2). Mean ± SD; one-way ANOVA. **(I)** Quantification of Cd11b$^+$ cells in tumors derived from Yumm5.2 (*Cdkn2a*^{High}) treated with pexidartinib (Pex, 45 mg/kg, o.g., 3×/week) or vehicle. Mean ± SD; student's t-test**. (J)** Quantification of Cd8$^+$ cells in tumors derived from Yumm1.7 (*Cdkn2a*^{Null}) cells expressing empty vector (EV) control or

physiological levels of p16 (p16 Exp). Mean ± SD; student's t-test. * p<0.05, ** p<0.01, *** p<0.001, **** p<0.0001, ns = not significant.

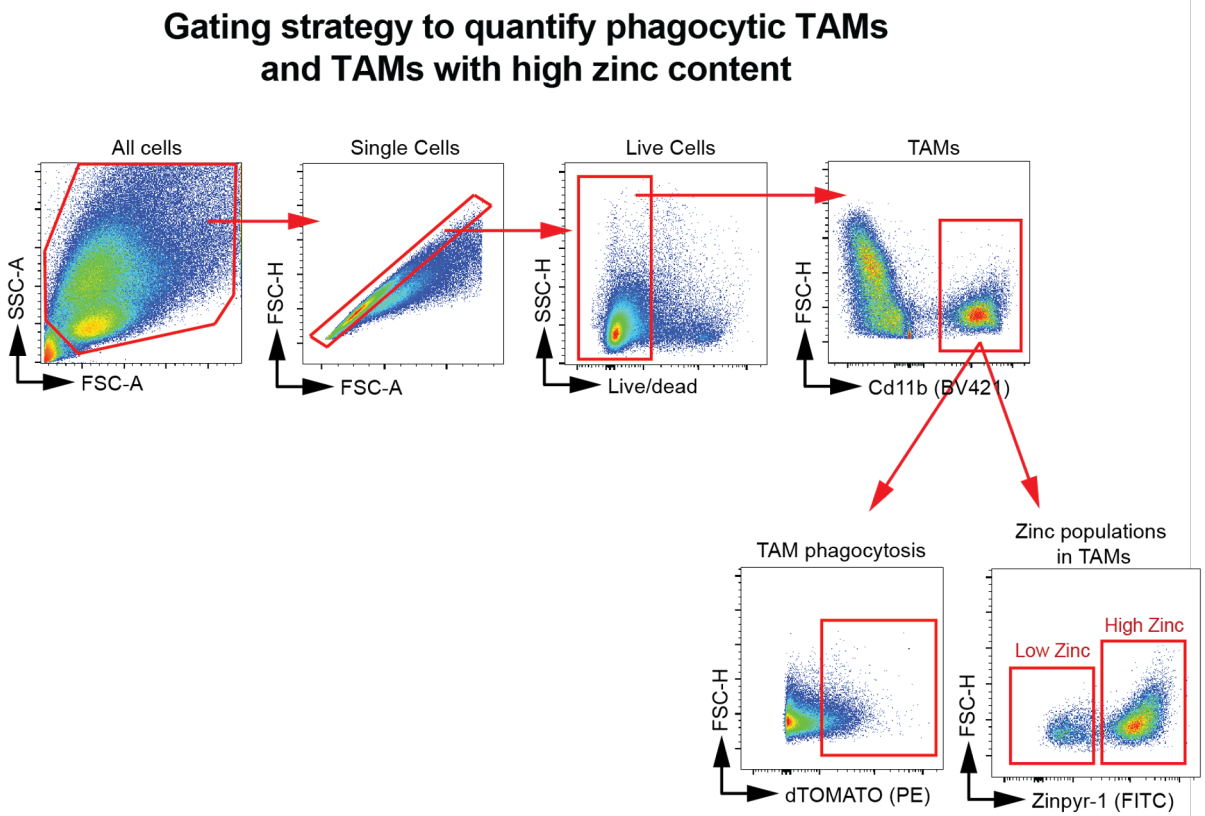

Figure S2. TAM gating strategy. Related to Figures 2, 6, 7, and S6. Figure shows the strategy used to identify live tumor-associated macrophages (TAMs), defined as the Cd11b$^+$ population, and the subsequent gating to quantify: (1) High Zinc TAMs, defined as Cd11b$^+$ TAMs with high Zinpyr-1 fluorescence, and (2) Phagocytic TAMs, defined as Cd11b$^+$ TAMs positive for dTOMATO, the fluorophore used to label the cancer cells implanted into mice (see **Fig. 2E**).

645

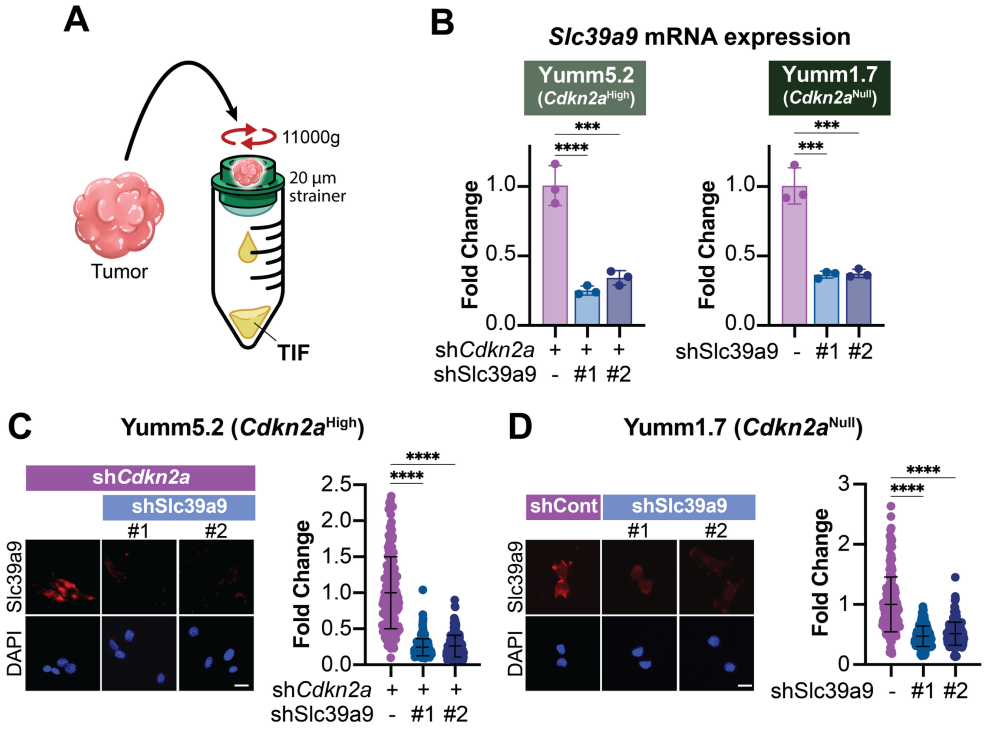

Figure S3. Tumor Interstitial Fluid (TIF) isolation; knockdown of Slc39a9 in cancer cells. Related to Figure 3. (A) Schematic of procedure to collect tumor interstitial fluid (TIF). **(B)** Slc39a9 mRNA expression in the indicated cell lines. Fold change to shControl group. Mean ± SD; one-way ANOVA. **(C-D)** Representative images (left) and quantification (right) of Slc39a9 immunofluorescence in **(C)** Yumm5.2 (*Cdkn2a*^{High}) cells with knockdown of GFP (shControl) or *Cdkn2a* (sh*Cdkn2a*, hairpins #1 and #2). Mean ± SD (n=200/group); one-way ANOVA. **(D)** Yumm1.7 (*Cdkn2a*^{Null}) cells expressing empty vector (EV) or physiological levels of p16 (p16 Exp). Mean ± SD (n=200/group); one-way ANOVA. Scale bars = 25µm.* p<0.05, ** p<0.01, *** p<0.001, **** p<0.0001, ns = not significant.

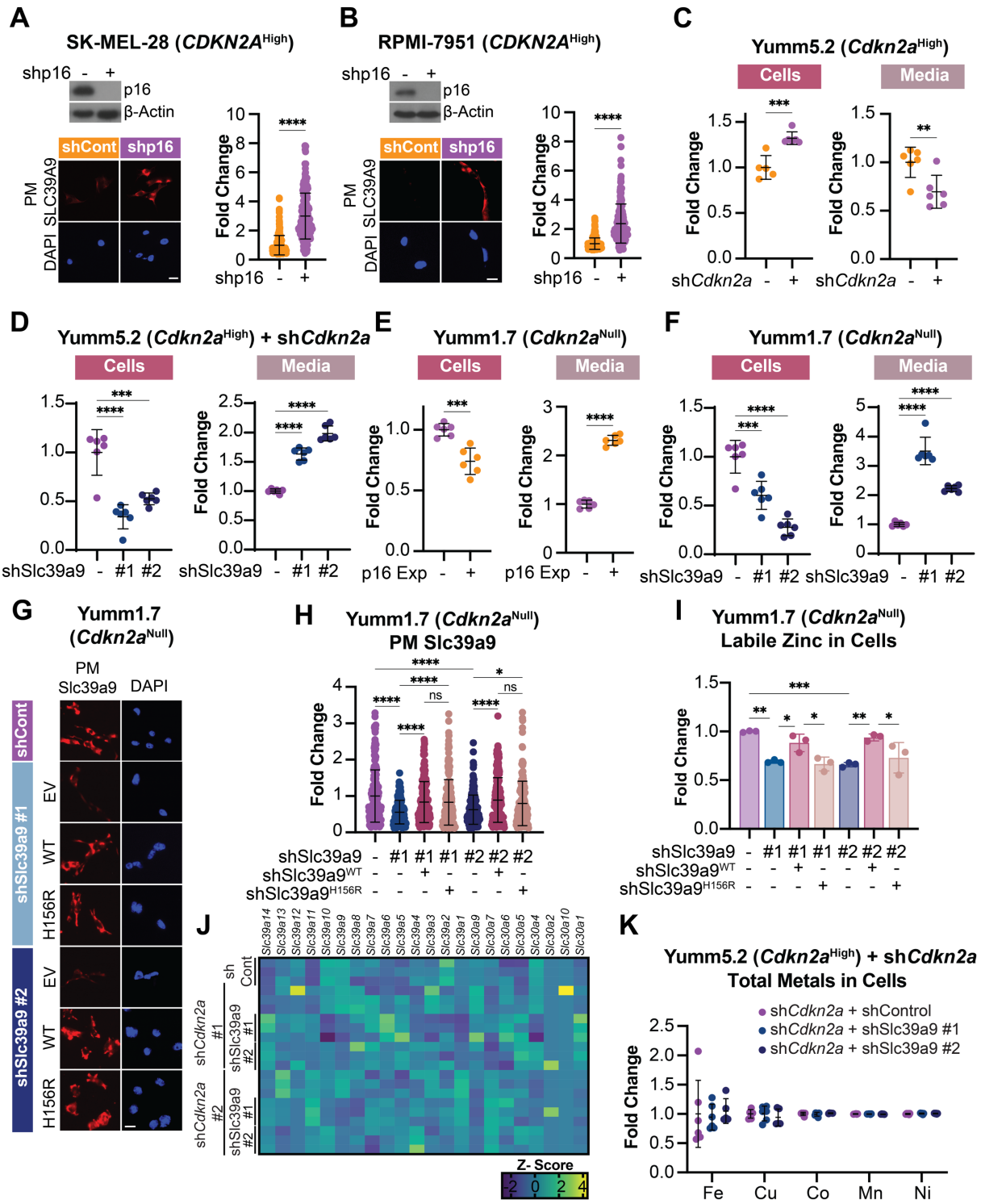

Figure S4. Knockdown of p16 in human melanoma cells increases plasma membrane SLC39A9; Slc39a9 regulates zinc uptake in *Cdkn2a*^{Low} cells. Related to Figure 4. (A-B) Top left- Immunoblot analysis of p16. β-Actin was used as a loading control. Bottom- representative images (bottom left), and quantification (bottom right) of the human melanoma cell lines **(A)** SK-MEL-28 (*Cdkn2a*^{High}) and **(B)** RPMI-7951 (*Cdkn2a*^{High}) with knockdown of GFP (shControl) or p16 (shp16). Mean ± SD (n=200/group); Student's t-test. **(C-F)** Dot plot showing total zinc quantification

by ICP-MS in cells (left) and media (right) in **(C)** Yumm5.2 (*Cdkn2a*^{High}) cells with knockdown of GFP (shControl) or *Cdkn2a* (sh*Cdkn2a*), **(D)** Yumm5.2 (*Cdkn2a*^{High}) cells with knockdown of *Cdkn2a* (sh*Cdkn2a*) alone or in combination with knockdown of GFP (shControl) or Slc39a9 (shSlc39a9, hairpins #1 and #2), **(E)** Yumm1.7 (*Cdkn2a*^{Null}) cells expressing empty vector (EV) or physiological levels of p16 (p16 Exp), and **(F)** Yumm1.7 (*Cdkn2a*^{Null}) cells with knockdown of GFP (shControl) or Slc39a9 (shSlc39a9, hairpins #1 and #2). Mean ± SD; Student's t-test and one-way ANOVA. **(G-I)** Yumm1.7 (*Cdkn2a*^{Null}) cells with knockdown of GFP (shControl) or Slc39a9 (shSlc39a9, hairpins #1 and #2) alone or in combination with empty vector (EV) control, wildtype (WT), or hypomorphic mutant (H156R) Slc39a9. **(G)** Representative images of Slc39a9 immunofluorescence on non-permeabilized cells to visualize plasma membrane (PM) Slc39a9. **(H)** Quantification of (G). Mean ± SD (n=200/group); one-way ANOVA. **(I)** Labile zinc quantification in cells. Mean ± SD; one-way ANOVA. **(J)** Heatmap of expression values for the indicated genes in the indicated Yumm5.2 isogenic cells. **(K)** Quantification of indicated metals by ICP-MS in Yumm5.2 (*Cdkn2a*^{High}) cells with knockdown of *Cdkn2a* (sh*Cdkn2a*) alone or in combination with knockdown of GFP (shControl) or Slc39a9 (shSlc39a9, hairpins #1 and #2). Mean ± SD. Scale bars = 25μm.* p<0.05, ** p<0.01, *** p<0.001, **** p<0.0001, ns = not significant.

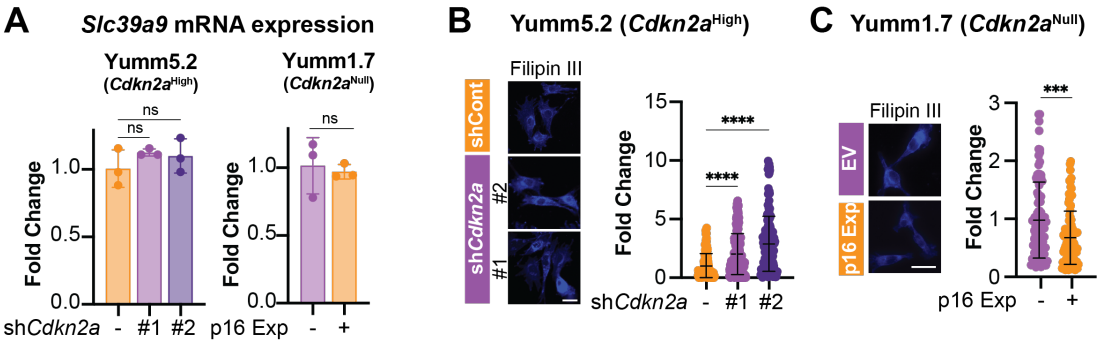

Figure S5. Modulation of *Cdkn2a*/p16 expression does not affect *Slc39a9* mRNA expression; *Cdkn2a*^{Low} cancer cells have decreased cholesterol. Related to Figure 5. (A) *Slc39a9* mRNA expression in the indicated cell lines. **(B-C)** Representative images of Filipin III staining to detect cholesterol (left) and quantification (right) in **(B)** Yumm5.2 (*Cdkn2a*^{High}) cells with knockdown of GFP (shControl) or *Cdkn2a* (sh*Cdkn2a*, hairpins #1 and #2) and **(C)** Yumm1.7 (*Cdkn2a*^{Null}) cells expressing empty vector (EV) control of physiological levels of p16 (p16 Exp). Mean ± SD (n=200/group); one-way ANOVA, student's t-test. Scale bars = 25μm.* p<0.05, ** p<0.01, *** p<0.001, **** p<0.0001, ns = not significant.

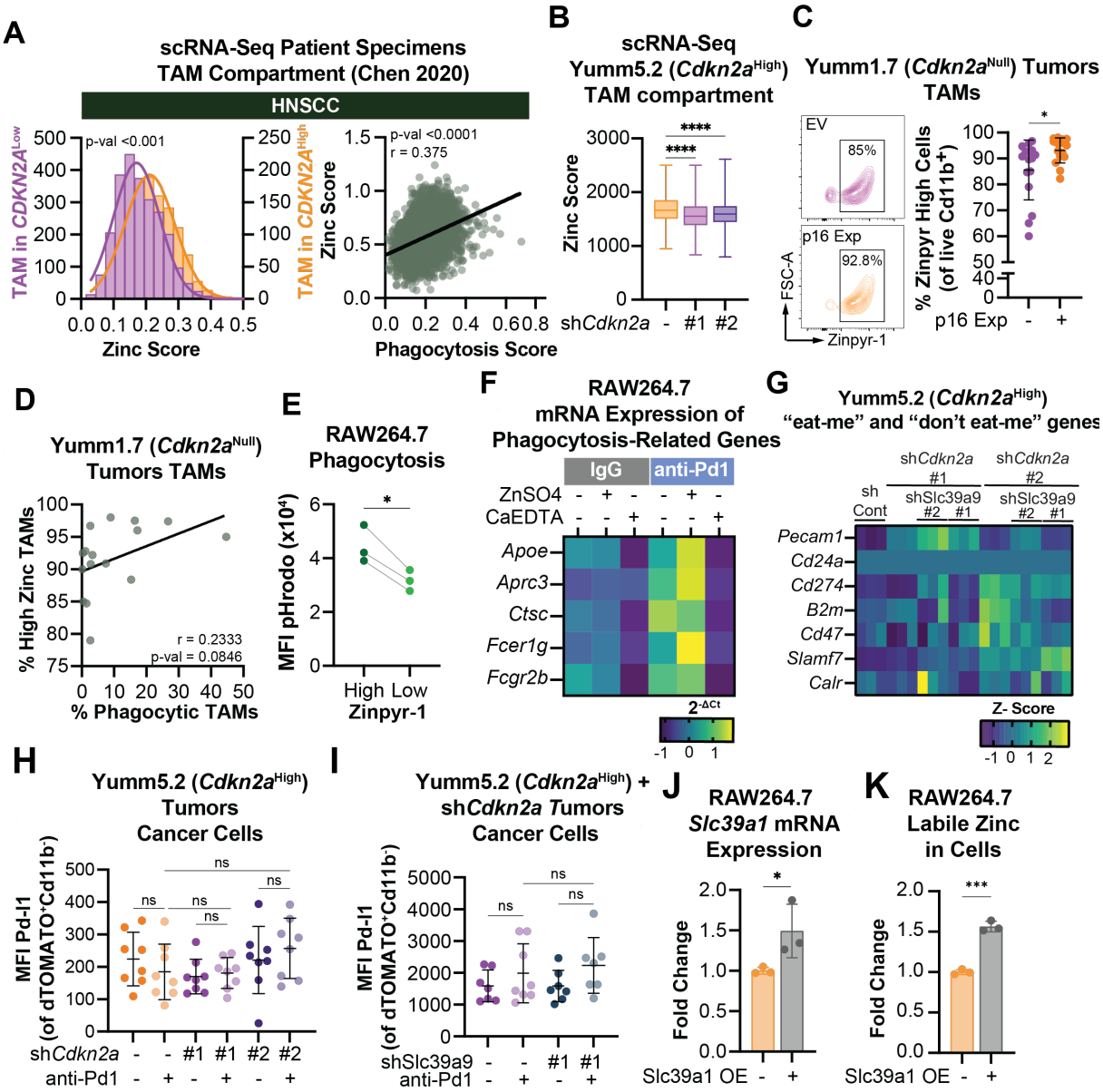

Figure S6. TAMs in *CDKN2A*^{Low} tumors have decreased zinc, correlating with phagocytosis activity; Zinc regulates the expression of phagocytic-related genes; Knockdown of *Cdkn2a* alone or in combination with Slc39a9 knockdown does not markedly affect the mRNA expression of 'eat me' and 'don't eat me' signals; *Cdkn2a*^{Low} cancer cells alone or with knockdown of Slc39a9 do not have altered Pd-l1 expression *in vivo*. Related to Figure 6. (A) scRNA-Seq dataset from head and neck squamous cell carcinoma (HNSCC) patients stratified by *CDKN2A* expression in cancer cells. Histogram showing the zinc score in TAMs from the indicated scRNA-Seq datasets from melanoma patients stratified by *CDKN2A* expression in cancer cells (left) and zinc score correlation with phagocytic score (right). Linear mixed models and Pearson correlation **(B)** Box plot showing zinc signatures scores in the TAM compartment of the scRNA-Seq from Yumm5.2 (*Cdkn2a*^{High}) cells with knockdown of *Cdkn2a* (sh*Cdkn2a*, hairpins #1 and #2). One-way ANOVA. **(C-D)** dTOMATO-labeled Yumm1.7 (*Cdkn2a*^{Null}) cells expressing empty vector (EV) control or physiological levels of p16 (p16 Exp) were implanted into mice. **(C)** Representative flow

673

cytometry plots of labile zinc in TAMs (left) and quantification (right). Mean ± SD; Student's t-test. **(D)** Correlation between labile zinc in TAMs and TAM phagocytosis. Person's correlation. **(E)** Mean fluorescence intensity (MFI) of pHrodoRed in RAW264.7 macrophages stratified based on high or low Zinpyr-1 staining of intracellular labile zinc. Mean ± SD; Student's t-test. **(F)** Heatmap of phagocytosis-related genes measured by qPCR in RAW264.7 macrophages treated with ZnSO4 (30µg, 16h) or CaEDTA (3mM, 16h) in combination with IgG or anti-Pd1 (1 µg/mL,16h) in FBS-free media. **(G)** Heatmap of expression values for the indicated 'eat me' and 'don't eat me' genes in Yumm5.2 (*Cdkn2a*^{High}) cells with knockdown of *Cdkn2a* (sh*Cdkn2a*, hairpins #1 and #2) alone or in combination with knockdown of GFP (shControl) or Slc39a9 (shSlc39a9, hairpins #1 and #2). **(H)** Mice were implanted with dTOMATO-labeled Yumm5.2 (*Cdkn2a*^{High}) cells with knockdown of GFP (shControl) or *Cdkn2a* (sh*Cdkn2a* #1 or #2). Mice were treated with IgG or anti-PD1 (200 µg, i.p., 3×/week). Dot plot of mean fluorescence intensity (MFI) of Pd-l1 in cancer cells (dTOMATO^{+} and Cd11b^{-}). Mean ± SD; one-way ANOVA. **(I)** Mice were implanted with dTOMATO-labeled Yumm5.2 (*Cdkn2a*^{High}) cells with knockdown of *Cdkn2a* (sh*Cdkn2a*) alone or in combination with knockdown of GFP (shControl) or Slc39a9 (shSlc39a9). Mice were treated with IgG or anti-PD1 (200 µg, i.p., 3×/week). Dot plot of mean fluorescence intensity (MFI) of Pd-l1 in cancer cells (dTOMATO^{+} and Cd11b^{-}). Mean ± SD; one-way ANOVA. **(J)** Bar plot of *Slc39a1* mRNA expression in RAW264.7 macrophages expressing empty vector control or Slc39a1 overexpression plasmid (Slc39a1 OE). Mean ± SD as the fold change relative to shControl; Student's t-test. **(K)** Bar plot of mean fluorescence intensity (MFI) of labile zinc in RAW264.7 macrophages expressing empty vector (EV) control or Slc39a1 overexpression plasmid (Slc39a1 OE). Mean ± SD as the fold change relative to shControl; Student's t-test. * $p<0.05$, ** $p<0.01$, *** $p<0.001$, **** $p<0.0001$, ns = not significant.

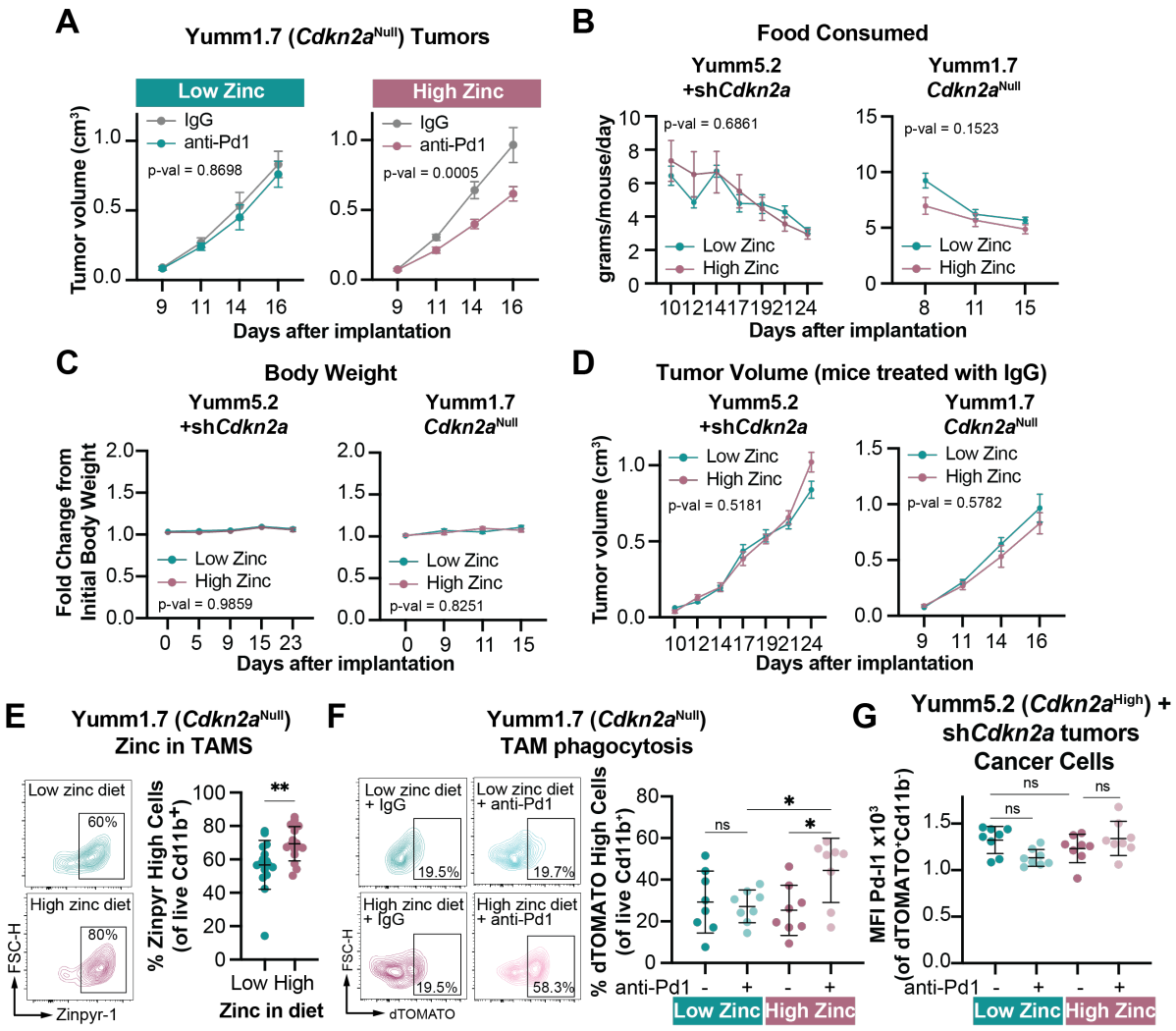

Figure S7. High zinc diet overcomes anti-Pd1 resistance in the Yumm1.7 *Cdkn2a*^{Null} model; Different zinc diets do not alter body weight or food consumed; Different zinc diets do not alter cancer cell Pd-l1 expression *in vivo*. Related to Figure 7. (A) Mice were fed a low (55 mg/kg) or high (300 mg/kg) zinc diet and implanted with Yumm1.7 (*Cdkn2a*^{Null}) cells expressing empty vector (EV) control or physiological levels of p16 (p16 Exp). Mice were treated with IgG or anti-PD1 (200 µg, i.p., 3×/week). Longitudinal tumor growth in the indicated groups. Mean ± SEM (n=12/group); Mixed-effects model. **(B-D)** Mice were assigned to low (55 mg/kg) or high (300 mg/kg) zinc diets and then implanted with Yumm5.2 (*Cdkn2a*^{High}) cells with knockdown of *Cdkn2a* (shCdkn2a, left) or Yumm1.7 (*Cdkn2a*^{Null}) cells expressing empty vector (EV) control or physiological levels of p16 (p16 Exp, right). Mice were treated with IgG or anti-Pd1 (200 µg, i.p., 3×/week). **(B)** Food consumed. **(C)** Body weight. **(D)** Longitudinal tumor growth in IgG treated groups. Mean ± SEM (n=12/group); Mixed-effects model. **(E-F)** Mice were assigned to a high (300 mg/kg) zinc diet and implanted with Yumm1.7 (*Cdkn2a*^{Null}) cells expressing empty vector (EV) control or physiological levels of p16 (p16 Exp). Once tumor establishment, mice were treated with IgG or anti-Pd1 (200 µg, i.p., 3×/week). **(E)** Representative flow cytometry plots (left) and quantification (left) of labile zinc in TAMs. Mean ± SD; student's t-test. **(F)** Representative flow cytometry plots (left) and quantification (right) of the percentage of TAMs with dTOMATO signal (phagocytic TAMs). Mean ± SD; one-way ANOVA. **(G)** Mice were fed a high (300 mg/kg) zinc diet and implanted with dTOMATO-labeled Yumm5.2 (*Cdkn2a*^{High}) cells with knockdown of GFP (shControl) or *Cdkn2a* (sh*Cdkn2a*). Once tumor establishment, mice were treated with IgG or anti-Pd1 (200 µg, i.p., 3×/week). Dot plot of mean fluorescence intensity (MFI) of Pd-l1 in cancer cells (dTOMATO^{+} and Cd11b^{-}). Mean ± SD; one-way ANOVA. * p<0.05, ** p<0.01, *** p<0.001, **** p<0.0001, ns = not significant.

Acknowledgements

This work was supported by grants from the National Institutes of Health (R37CA240625 to KM. Aird, R01CA259111 to KM. Aird and NW. Snyder, 1R01CA301573-01 to KM. Aird, N. Hempel, and R. Buj, R01DE031729 and P50CA254865 to R. Bao, and T32 CA082084 to RE. Dadey), the Congressionally Directed Medical Research Program (HT9425-23-1-0436 to KM. Aird and OC230324 to NK. Tangudu), the Melanoma Research Foundation (to R. Buj), the HERA Ovarian Cancer Foundation (to A. Amalric, A. Uboveja, and NK. Tangudu), the University of Chicago Cancer Center Support Grant (to A. Muir), the Ludwig Center for Metastasis Research (to A. Muir), the MaryEllen Connelan Award (to JJ. Apiz Saab), the Robert C and Mary Jane Gallo Scholarship Fund (to JJ. Apiz Saab) and the Harper Fellowship at the University of Chicago (to JJ. Apiz Saab). We utilized resources from the Hillman Cancer Center shared facilities, partially supported by award P30CA047904 including the Animal Facility, the Cytometry Facility (RRID:SCR_025361), the Biostatistics Facility (RRID:SCR_025355), and the Cancer Bioinformatics Services (RRID:SCR_025355). The Cancer Bioinformatics Services were additionally supported by the University of Pittsburgh Center for Research Computing, specifically the HTC high-performance computing cluster, which is supported by NIH (S10OD028483). We also used the University of Pittsburgh Single Cell Core Facility (RRID:SCR_025110), whose services and instruments were in part graciously supported by the University of Pittsburgh and the Department of Medicine. Similarly, we also used the Health Sciences Sequencing Core at UPMC Children's Hospital of Pittsburgh (RRID:SCR_023116), which resources were generously supported by the University of Pittsburgh, the Office of the Senior Vice Chancellor for Health Sciences, the Department of Pediatrics, the Institute for Precision

Medicine, and the Richard K. Mellon Foundation for Pediatric Research. Finally, we extend our gratitude to Francisco J. Vazquez Moreno for his exceptional contribution to the graphic illustrations included in this paper.

Author Contributions

Raquel Buj: Conceptualization, Investigation, Methodology, Visualization, Writing – Original Draft, Review & Editing, Funding acquisition. Aidan R. Cole: Investigation, Methodology, Writing – Review & Editing. Jeff Danielson: Investigation, Methodology. Jimmy Xu: Investigation, Methodology. Akash Kishore: Investigation, Methodology. Katarzyna M. Kedziora: Investigation, Methodology. Jie Chen: Investigation, Methodology. Baixue Yang: Investigation, Methodology, Writing – Review & Editing. David Barras: Investigation, Methodology. Apoorva Uboveja: Investigation, Methodology, Writing – Review & Editing. Amandine Amalric: Investigation, Methodology, Writing – Review & Editing. Juan J. Apiz Saab: Investigation, Methodology. Jayamanna Wickramasinghe: Investigation, Methodology. Naveen Kumar Tangudu: Investigation, Methodology, Writing – Review & Editing. Evan Levasseur: Investigation, Methodology, Writing – Review & Editing, Hui Wang: Investigation, Methodology. Aspram Minasyan: Investigation, Methodology. Rebecca E. Dadey: Investigation, Methodology. Allison C. Sharrow: Investigation, Methodology. Sheryl Kunning: Investigation, Methodology. Frank P. Vendetti: Investigation, Methodology. Dayana B. Rivadeneira: Investigation, Methodology. Christopher J. Bakkenist: Investigation, Methodology, Writing – Review & Editing. Tullia C Bruno: Investigation, Methodology, Writing – Review & Editing. Greg M. Delgoffe: Investigation, Methodology, Writing – Review & Editing. Nadine Hempel: Investigation, Methodology, Writing

– Review & Editing, Funding acquisition. Nathaniel W. Snyder: Investigation, Methodology, Writing – Review & Editing. Riyue Bao: Investigation, Methodology, Writing – Review & Editing. Adam C. Soloff: Investigation, Methodology, Writing – Review & Editing. John M. Kirkwood: Investigation, Methodology, Writing – Review & Editing. Denarda Dangaj Laniti: Investigation, Methodology, Writing – Review & Editing, Andrew V. Kossenkov: Investigation, Methodology, Writing – Review & Editing. Alexander Muir: Investigation, Methodology, Writing – Review & Editing. Jishnu Das: Investigation, Methodology, Writing – Review & Editing. Diwakar Davar: Investigation, Methodology, Writing – Review & Editing. Clementina Mesaros: Investigation, Methodology, Writing – Review & Editing. Katherine M. Aird: Conceptualization, Investigation, Visualization, Writing – Original Draft, Review & Editing, Supervision, Project Administration, Funding Acquisition. All authors reviewed the results and approved the final version of the paper.

Declaration of Interests

The authors declare no competing interests.

758 **MATERIAL AND METHODS**

759 **Melanoma Patient Cohort**

760 This cohort comprises 248 cutaneous melanoma patients, pooled from five independent,
761 publicly available studies[35,108,189-191], with publicly available pre-treatment RNA-Seq and
762 overall survival data. Details are provided in **Table S6**. Briefly, eligible patients had resec-
763 table stage III melanoma treated with neoadjuvant immunotherapy or unresectable stage
764 III/IV treated with systemic immunotherapy. Treatment regimens included anti-PD1 mon-
765 otherapy or combination therapy with anti-CTLA-4 or TLR9 agonists. For **Fig. 1A**, patients
766 were stratified according to *CDKN2A* expression. Expression levels of the target genes
767 were categorized as follows: patients in or above the third tertile were considered to have
768 high expression, while those in or below the first tertile were considered to have low ex-
769 pression. For **Fig. 2B**, T cell inflamed signature[192] and phagocytosis signature scores
770 (this paper, see **Table S1**) were calculated based on the sum of the genes in each signa-
771 ture. Patients were stratified according to median score.

772

773 **Kaplan-Meier plotter (KMP) Cancer Patient Cohort:**

774 Survival data from cancer patients was downloaded from Kaplan-Meier (KM) plotter 'Start
775 KM Plotter for immunotherapy' (kmplot.com)[193-195] in January 2025. The analysis was
776 performed using the following parameters: the gene symbol was set to *CD8A* with *Filter*
777 *by mean expression* of patients with high expression of *ITGAM* (**Fig. 1G**). Patients were
778 split based on *mean* expression. *Overall survival* was selected as the survival metric, with
779 no restrictions on follow-up thresholds. The analysis was restricted to patients who had

received *all* anti-PD1 therapy and included *all* tumor types and sex. The resulting data was exported as text for subsequent analysis in Graph Prism 10.

Patient scRNA-Seq data sets and processing

The Jereby-Arnon 2018 melanoma dataset[196] and the Chen 2020 head and neck squamous cell carcinoma (HNSCC) dataset[197] were downloaded from the Gene Expression Omnibus (GSE115978 and GSE150430, respectively). For sample processing, genes were retained if expressed in at least three cells, cells were kept if they had more than 200 features, and cells with >20% mitochondrial reads were removed. Library size bias was corrected using Seurat's NormalizeData, scaling expression values to 10,000 counts per cell and log-transforming the data. Data was then scaled using Seurat's ScaleData with all genes as features. Cancer cells and macrophages were annotated based on publicly available cell type labels. Tumor samples were then stratified into *CDKN2A*^{High} and *CDKN2A*^{Low} groups based on *CDKN2A* median expression in the cancer cell compartment. Signature scores were calculated as the mean expression of genes in the zinc signature and phagocytosis signature annotated in this paper (**Table S1**) for each cell in the macrophage or cancer cell compartment.

Cell Lines and culture conditions

All cell lines used in this study were purchased from ATCC and were used within 50 passages. ATCC performs cell line authentication by short tandem repeat (STR) profiling. Cells were cultured within 3 months of receipt or resuscitation. The murine melanoma cell lines Yumm5.2 (ATCC, catalog no. CRL-3367, RRID: CVCL_JK43) and Yumm1.7

803 (ATCC, catalog no. CRL-3362, RRID: CVCL_JK16) were cultured in DMEM and Ham's
804 F-12 50/50 media (Corning, catalog no. 10-092-CV), supplemented with nonessential
805 amino acids (Corning, catalog no. 25-025-CI). The murine macrophage cell line RAW
806 264.7 (ATCC, catalog no. TIB-71 ™, RRID: CVCL_0493), the human melanoma cell line
807 SK-MEL-28 (ATCC, catalog no. HTB-72, RRID: CVCL_0526), and the human embryonic
808 kidney cell line HEK293-FT (ATCC, catalog no. CRL-3216, RRID: CVCL_6911) were cul-
809 tured in DMEM (Corning, catalog no. 10-013-CV), while the human melanoma cell line
810 RPMI-7951 (ATCC, catalog no. HTB-66, RRID: CVCL_1666) was cultured in MEM (Corn-
811 ing, catalog no. 10-009-CV). All cell lines were supplemented with 10% FBS (BioWest,
812 catalog no. S1620) and 1% Penicillin/Streptomycin (Gibco, catalog no. 15-140-122) and
813 maintained at 37 °C with 5% CO_2. To ensure the absence of Mycoplasma contamination,
814 all cell lines were tested monthly as described in[198].
815
816 **Plasmid information and cloning:**
817 To perform knockdown experiments, short hairpin RNAs (shRNAs) targeting specific
818 genes were used. The shRNA sequences used in this study included: human shp16
819 (TRCN0000010482), mouse sh*Cdkn2a* #1 (TRCN0000077816) and #2
820 (TRCN0000362595), and mouse shSlc39a9 #1 (TRCN0000346746) and #2
821 (TRCN0000346750). The hairpins for shp16 and shSlc39a9 #1 and #2 were purchased
822 pre-cloned into the lentiviral vectors expressing puromycin resistance (Sigma-Aldrich).
823 The sh*Cdkn2a* #1 and #2 hairpins sequences (TRCN0000077816 and
824 TRCN0000362595, respectively) were obtained from Integrated DNA Technologies (IDT)
825 as desalted oligos and subsequently cloned into the lentiviral pLKO.1 vector expressing

826 blasticidin resistance (Addgene, catalog no. 26655). Briefly, 2 µg of pLKO.1 vector was
827 digested with 1 µL of EcoRI-HF (New England Biolabs, catalog no. R3101S), 1 µL of
828 AgeI-HF (New England Biolabs, catalog no. R3552S), and 1 µL of rCutsmart 10X Buffer
829 (New England Biolabs, catalog no. B6004S) in a final reaction volume of 10 µL. The di-
830 gestion was incubated for 1 hour at 37°C. The linearized vector was separated by elec-
831 trophoresis on a 1% agarose (IBI Scientific, catalog no. IB70070) gel and purified using
832 the Qiagen Gel Extraction Kit (Qiagen, catalog no. 28704), following the manufacturer's
833 instructions. Simultaneously, shRNA oligos were reconstituted to a final concentration of
834 100 µM in molecular-grade water (Corning, catalog no. 46-000-CM) and annealed by in-
835 cubating 11.25 µL of each oligo with 2.5 µL of 10X annealing buffer (1M NaCl, 100 mM
836 Tris, pH 7.4). The reaction was performed in a thermal cycler (Bio-Rad, T100™ Thermal
837 Cycler, serial no. 621BR59583) starting at 95°C for 5 minutes, followed by a ramp-down
838 to 25°C at 5°C/min. The ligation reaction was prepared by combining 50 ng of purified
839 pLKO.1 vector with 1 µL of annealed shRNA oligos (diluted 1:400 in 0.5X annealing
840 buffer), 1 µL of T4 ligase (New England Biolabs, catalog no. M0202T), and 1 µL of T4
841 ligase buffer (New England Biolabs, catalog no. B0202S) in a final volume of 10 µL. The
842 reaction was incubated at room temperature for 3 hours, after which 5 µL of the ligation
843 mixture was used to transform One Shot™ Stbl3™ Chemically Competent *E. coli*
844 (Thermo Fisher Scientific, catalog no. C737303) following the manufacturer's instructions.
845 Control lentiviral vectors, (Addgene, catalog no. 110419, RRID: Addgene_110419 and
846 Addgene, catalog no. 30323, RRID: Addgene_30323), were used for both human and
847 mouse experiments. For overexpression experiments, lentiviral plasmids were synthe-
848 sized by Twist Bioscience. The Twist Bioscience empty vector (EV) was used as the

849 control in overexpressing experiments. The pLX304-dTOMATO lentiviral plasmid was
850 generously provided by the Gomes Lab at the H. Lee Moffitt Cancer Center.
851
852 **Lentiviral Packaging and Infection conditions**
853 Lentiviral vectors were packaged as follows: 10 µg of the corresponding lentiviral vector
854 was mixed with 7.5 µg of psPAX2 (Addgene, catalog no. 12260, RRID: Addgene_12260)
855 and 7.5 µg of pMD2.G (Addgene, catalog no. 12259, RRID: Addgene_12259) in 1.5 mL
856 of Opti-MEM™ media (Gibco, catalog no. 31985070) and incubated for 5 minutes at room
857 temperature. In parallel, 50 µL of Lipofectamine™ 2000 Transfection Reagent (Invitrogen,
858 catalog no. 11668019) was diluted in 1.5 mL of Opti-MEM™ media and incubated for 5
859 minutes at room temperature. The Lipofectamine mixture was added dropwise to the
860 plasmid mixture, gently swirled to mix, and incubated for 20 minutes at room temperature.
861 The Lipofectamine-lentiviral complexes were then added dropwise to a 60-70% confluent
862 10 cm dish of HEK293-FT cells, seeded 24 hours in advance and containing 7 mL of
863 regular media, and incubated at 37°C with 5% CO2. Six to eight hours later, the media
864 was replaced with 9 mL of fresh regular media and incubated at 37°C with 5% CO_2. Sev-
865 enty-two hours later, the viral supernatants were collected, filtered through a 45 µm filter
866 (Fisherbrand™, catalog no. 09-720-005), and used to infect target cells for 16 hours. In-
867 fected cells were selected for 3 days with 1 µg/mL puromycin (Thermo Fisher Scientific,
868 catalog no. A1113802) for SK-MEL-28 and RPMI-7951, 2 µg/mL puromycin for RAW
869 264.7 cells, and 3 µg/mL puromycin and/or 3 µg/mL blasticidin (InvivoGen, catalog no.
870 ant-bl-05) for Yumm5.2 and Yumm1.7 cells.
871

872 **Mouse Models**

873 All mice were housed in a HEPA-filtered ventilated rack system at the Animal Facility of
874 the Assembly Building of The Hillman Cancer Center, University of Pittsburgh School of
875 Medicine. Mice were maintained on a 12-hour light/dark cycle at 21 ± 2 °C and were
876 group-housed up to 5 mice per cage. All animal procedures were approved by the Insti-
877 tutional Animal Care and Use Committee (IACUC) of the University of Pittsburgh.

878

879 To investigate the role of *CDKN2A* in the response to immunotherapy, we developed two
880 complementary subcutaneous syngeneic melanoma models. In the first model, *Cdkn2a*
881 expression was knocked down in the *Cdkn2a*^{High} murine melanoma cell line Yumm5.2. In
882 the second model, p16 was overexpressed in the *Cdkn2a*^{Null} melanoma cell line Yumm1.7
883 to physiological levels that did not induce a senescence-associated phenotype. To inves-
884 tigate the role of SLC39A9 in resistance to anti-Pd1 treatment in *Cdkn2a*^{Low} cancer cells,
885 we used Yumm5.2 cells with dual knockdown of *Cdkn2a* and *Slc39a9* (sh*Cdkn2a*n +
886 sh*Slc39a9*), as well as Yumm1.7 cells with *Slc39a9* knockdown (sh*Slc39a9*). In all models
887 described above, 350,000 cells were subcutaneously implanted into the right flank of 6–
888 8 weeks old male C57BL/6J mice (The Jackson Laboratory, strain #000664, RRID:
889 IMSR_JAX:000664). To assess the role of T cells in anti-Pd1 response, 350,000
890 Yumm5.2 sh*Cdkn2a*/sh*Slc39a9* double knockdown cells were implanted into B6.129s7-
891 *Rag1*^{tm1Mom}/J mice (The Jackson Laboratory, strain #002216, RRID: IMSR_JAX:002216).
892 For co-injection experiments, 350,000 Yumm5.2 sh*Cdkn2a* cells were mixed with 35,000
893 RAW264.7 cells overexpressing Slc39a1 and subcutaneously implanted into the right
894 flank of 6-8 weeks old male NOD.Cg-Prkdc^{scid} Il2rg^{tm1Wjl}/Szj (The Jackson Laboratory,

895 strain #005557, RRID:IMSR_JAX:005557). In all cases, control groups received cells
896 overexpressing corresponding shControl (shGFP) or empty vector (see *Plasmid Infor-*
897 *mation and cloning* section).
898
899 In all cases described above, cells were resuspended in 200 µL DPBS (Corning, catalog
900 no. 21-031-CV) and subcutaneously implanted using a 1 mL tuberculin syringe and a 25G
901 needle (Becton Dickinson, catalog no. 309626). Tumor formation was monitored, and all
902 models developed palpable tumors within 8–14 days of implantation. Tumor length (L)
903 and width (W) were measured three times a week once palpable tumors appeared using
904 an electronic caliper set in mm (Adoric, model number# KC24, resolution 0.1mm ±
905 0.2mm). Tumor volume was calculated using the formula: $\frac{1}{2}(L \times W^2)$ where $L > W$. Mouse
906 body weight was measured weekly using an electronic scale. The experimental endpoint
907 for longitudinal tumor growth studies was defined as the point when the first mouse
908 reached IACUC-approved criteria: either a tumor volume exceeding 1 cm^3 or a 20% loss
909 of body weight, whichever occurred first. For survival studies, the endpoint for each ani-
910 mal was similarly determined based on IACUC guidelines.
911
912 **Mice treatments**
913 For anti-Pd1 experiments, mice were administered 200 µg of anti-mouse Pd1 (Leinco
914 Technologies, catalog no. P362) or placebo IgG2a (Leinco Technologies, catalog no. I-
915 1177). diluted in DPBS to a final volume of 200 µL, by intraperitoneal injection three times
916 per week using insulin syringes (Excel International, catalog no. 26028). For macrophage
917 depletion, mice were treated with 45 mg/kg pexiclartinib (Selleck Chemicals, catalog no.

918 S7818), diluted in a vehicle solution containing 45% PE300 (Sigma-Aldrich, catalog no.
919 202371), 45% ddH_2O, 5% Tween-80 (Sigma-Aldrich, catalog no. P4780), and 5% DMSO
920 (Fisher BioReagents, catalog no. BP231-100), administered via oral gavage at a final
921 volume of 150 µL, three times per week. Treatment was delivered using a 1 mL syringe
922 (Becton Dickinson, catalog no. 309659) and a reusable animal feeding needle (Cadence
923 Science, catalog no. 7910; 2.5 mm ball diameter, 3.81 cm length, 20G, curved), which
924 were autoclaved between uses. Control mice received the same volume of vehicle solu-
925 tion following the same dosing schedule. All treatments described above were initiated
926 upon detection of palpable tumors. For dietary zinc experiments, standard rodent chow
927 (LabDiet, catalog no. 5P76) containing 110 ppm (110 mg/Kg) zinc was replaced with cus-
928 tom-made diets from LabDiet. Mice were fed either a high-zinc diet (LabDiet, catalog no.
929 5SNB) containing 300 ppm (300 mg/Kg) zinc or a low-zinc diet (LabDiet, catalog no.
930 5SNA) containing 55 ppm (55 mg/Kg) zinc. Both experimental diets were identical in com-
931 position to the standard chow, except for the zinc content. Mice were acclimated to the
932 new diet for 10 to 15 days prior to tumor cell implantation and continued on the assigned
933 diet throughout the experiment. The amount of food per cage was measured before and
934 after replenishing the feeder one to two times per week to estimate food intake per mouse
935 and day on each diet.
936
937 ***In vivo* and *in vitro* phagocytosis assay:**
938 For *in vivo* phagocytosis assays, cancer cells were infected with a lentivirus encoding the
939 dTOMATO fluorescent protein (see *Lentiviral Packaging and Infection conditions* sec-
940 tion). dTOMATO-positive cancer cells were sorted prior to implantation into mice. The

941 level of dTOMATO expression varied by less than 1% across the different cancer cell
942 groups implanted. Once tumors reached a volume of 250–300 mm^3, tumors were har-
943 vested, dissociated (see *Tumor Dissociation* section), stained, and analyzed by flow cy-
944 tometry (see *Immunostaining and Flow Cytometry* section). The percentage of phagocytic
945 TAMs was defined as the proportion of live $Cd11b^+$ cells that also expressed dTOMATO
946 (**Fig. 2E**). For *in vitro* phagocytosis assays, cancer cells were labeled with CellTrace™
947 Violet (Thermo Fisher, Cat. No. C34557) according to the manufacturer's instructions.
948 One million CellTrace-labeled cancer cells were added to 300,000 IFNγ-activated
949 RAW264.7 macrophages (100 ng/mL IFNγ for 24 hours) previously plated, and co-cul-
950 tured for 24 hours. After incubation, cells were harvested by scraping, stained, and ana-
951 lyzed by flow cytometry (see *Immunostaining and Flow Cytometry* section). The percent-
952 age of phagocytic RAW264.7 cells was defined as the live $Cd11b^+$ population that co-
953 expressed CellTrace Violet (**Fig. 2E**). Finally, the in vitro phagocytic activity was also de-
954 termined with the stablished pHrodo red E.coli particles (**Fig. S6E**) as follows: 75,000
955 RAW264.7 cells seeded in 12-well plates were washed with PBS and media replaced for
956 1.5 mL of 200 µg/mL of pHrodo red E.coli particles (Invitrogen, catalog no. P35361) re-
957 suspended in media without FBS and incubated 1h at 37°C and 5% CO_2. Cells were
958 scrapped out and stained with zinpry-1 and Live/Dead Fixable Near-IR Dead Cell Stain
959 (see *In vitro labile Zinc quantification* section).
960

961 **Tumor disassociation**

962 To obtain a single-cell suspension, dissected tumors were enzymatically and mechani-
963 cally disrupted. First, the tumors were mechanically minced using surgical disposable

964 scalpels (Surgical Design, catalog no. SCALPEL 12B) into pieces smaller than 5 mm in
965 diameter on a 6 cm plate. Next, 2 mL of enzymatic cocktail [8 mg of collagenase IV (Gibco,
966 catalog no. 17104-019), 800 µL of dispase (Stem Cell Technologies, catalog no. 07913),
967 and 25 µg of DNase (Sigma Aldrich, catalog no. D4263-5VL) diluted in FBS-free MEM
968 (Corning, catalog no. 10-009-CV)] was added to the minced tumors. The mixture was
969 incubated for 20 minutes at 37°C in a non-CO_2 incubator. Minced tumor pieces were then
970 further disrupted by smashing them between two fully frosted cytology slides (Fisher-
971 brand, catalog no. 12-550-401). The resulting single-cell suspension was filtered through
972 a 70 µm strainer (Fisherbrand, catalog no. 22-363-548) and resuspended in 5 mL of FBS-
973 free media. The cells were centrifuged at 350 g for 5 minutes at 4°C and resuspended in
974 1x RBC lysis buffer (BD, catalog no. 555899). The RBC lysis reaction was incubated for
975 2–5 minutes at room temperature, after which the reaction was stopped by adding 5 mL
976 of FBS-free media. The cells were then centrifuged at 350 g for 5 minutes at 4°C, resus-
977 pended in DPBS, and were ready for subsequent procedures.
978
979 **Single-cell RNA-Sequencing**
980 Yumm5.2 sh*Cdkn2a* hairpins #1 and #2, and control shGFP cells were subcutaneously
981 implanted into five mice per condition (see *Mice Models* section). Once reached a volume
982 of 0.5 cm^3, tumors were harvested and processed into a single-cell suspension (see *Tu-*
983 *mor cell disassociation* section). Single-cell suspensions were first stained with a 1:4000
984 dilution of viability dye (ThermoFisher Scientific, catalog no. 65-0863-14) in DPBS for 20
985 minutes on ice and in the dark. Then, cells were centrifuged at 350 g for 5 minutes at 4°C
986 and stained with 2 µg/mL of anti-Cd45 PE-conjugated antibody (ThermoFisher Scientific,

987 catalog no. 12-0451-83), diluted in EasySep™ buffer (Stemcell Technologies, catalog no.
988 20144) for 20 minutes on ice and protected from light. After centrifugation at 350 g for 5
989 minutes at 4°C, cells were resuspended and pooled by sample group in 5 mL of FBS-free
990 MEM media (Corning, catalog no. 10-009-CV). Single live PE-positive (Cd45+) cells were
991 sorted using a Sony MA900 cell sorter (serial no. 0714313) and collected in 0.04%
992 BSA/PBS for downstream processing. cDNA Libraries were prepared at the University of
993 Pittsburgh Single Cell Core Facility. Briefly, viability was confirmed with greater than 80%
994 live cells using a Nexcelom automated cell counter (serial no. Auto2000-201-1019). Sam-
995 ples were then labeled with TotalSeq-C antibody hashtags (Biolegend, catalog no.
996 155881, 155883, 155885, 155887, 155889, 155891) following manufacturer's instruc-
997 tions. Equal numbers of cells from each sample were then pooled together and loaded
998 onto the Chromium controller (serial no. CXVG11091) for single-cell capture and barcod-
999 ing. cDNA library preparation was carried out using the Chromium Next GEM Single Cell
1000 5' Reagent Kits v2 (10X Genomics, catalog no. PN-1000265) following the manufacturer's
1001 protocol. The sizes of the library pools were analyzed using a Standard Sensitivity NGS
1002 Fragment Analyzer Kit (Agilent) followed by fluorescent quantification using the Promega
1003 QuantiFluor ONE dsDNA kit on the Infinite F Nano+ (Tecan). The library pools were nor-
1004 malized per manufacturer protocol (Illumina). Sequencing was performed on the No-
1005 vaSeq 6000 platform (serial no. A00524), with 28bp/90bp paired-end reads. The se-
1006 quencing data was demultiplexed with 10X Genomics Cell Ranger mkfastq version
1007 v6.0.2. The resulting sequence data was then aligned to the mouse reference genome
1008 (mm10) using cellranger multi (v.7.1.0) to generate count matrices for each condition.
1009 Analysis was conducted using R (v.4.3.0). Seurat's was used for quality control, data

1010 normalization, and data analysis. The data was normalized using the NormalizeData func-
1011 tion, following which the top 2000 variable genes were chosen using the 'vst' parameter
1012 setting of the FindVariableFeatures function. The 6 data objects were merged and used
1013 for further analysis. Celltypes were annotated using ImmGen data and the SingleR pack-
1014 age. Gene Set Enrichment Analysis (GSEA) was performed using ranked gene lists
1015 (log2foldchange * log10pval) using the GOBP_PHAGOCYTOSIS mouse gene set from
1016 MSigDB. Pathway signature scores for each cell were computed using the ssGSEA
1017 framework as implemented in the escape package. Raw and processed RNA-seq data
1018 can be found on Gene Expression Omnibus (GSE291530).
1019

1020 **Immunostaining and flow cytometry**

1021 Tumors were harvested and processed into a single-cell suspension (see *Tumor disas-*
1022 *sociation* section). Single-cell suspensions were first blocked with 5 µg/mL of Cd16/Cd32
1023 (Invitrogen, catalog no. 14016185) diluted in DPBS for 10 minutes on ice. Cells were
1024 stained for 20 minutes at 4°C protected from the light after which cells were fixed in 4%
1025 paraformaldehyde (Sigma Aldrich, catalog no. 158127-3Kg) for 15 minutes at 4°C,
1026 shielded from light, and resuspended in FACS buffer (1x PBS, 10 mM HEPES [Gibco,
1027 catalog no. 15630080], 1% heat-inactivated FBS [Sigma Aldrich, catalog no. F4135-
1028 100ML], 0.05% sodium azide [Sigma Aldrich, catalog no. S2002-25G]). Stained cells were
1029 immediately analyzed on a Fortessa (Beckman Coulter, serial no. H64717700020).
1030 FlowJo version 10 was used for further analysis. Antibodies and dyes used in this study
1031 include: 0.5 µg/mL of anti-Cd11b Brilliant Violet 421-conjugated antibody (Biolegend, cat-
1032 alog no. 101236), 2 µg/mL of anti-Pd-l1 PE/Cyanine5-conjugated antibody (Biolegend,

1033 catalog no. 124344), 0.5 μg/mL of anti-Cd8a FITC-conjugated antibody (Thermo Fisher
1034 Scientific, cat no. 11-0081-82), 0.5 μg/mL of anti-Cd4 Brillian Violet 421-conjugated anti-
1035 body (Biolegend, catalog no. 100437), 2 μg/mL of anti-Cd45 PE-conjugated antibody
1036 (ThermoFisher Scientific, catalog no. 12-0451-83), 50 μM Zinpyr-1 (Cayman Chemical,
1037 catalog no. 15122). Antibodies were diluted in DPBS, containing a 1:1000 dilution of
1038 Live/Dead Fixable Near-IR Dead Cell Stain kit (Invitrogen, catalog no. L34976).
1039

1040 **Isolation of plasma and tumor interstitial fluid (TIF)**

1041 Blood from melanoma patients treated with anti-PD1 immunotherapy (**Fig. 3F**) was col-
1042 lected by venipuncture into ACD-A tubes (Becton-Dickinson, catalog no. 364606) as part
1043 of an IRB-approved biorepository protocol (HCC 20-2019, MOD20010266-016). Mouse
1044 blood was collected via lancet check bleed (Braintree Scientific, catalog no. GR 4MM)
1045 into EDTA tubes (SAI Infusion Technologies, catalog no. K3EDTA). Plasma was sepa-
1046 rated by centrifugation at 1500g for 10 minutes at 4°C and stored at -80°C for later anal-
1047 ysis. After bleeding, animals were euthanized by cervical dislocation, and tumors were
1048 harvested, weighed, rinsed briefly in saline (150 mM NaCl), and excess saline removed
1049 using filter paper (Cytiva, catalog no. 1001-813). TIF was isolated using a previously de-
1050 scribed centrifugal method[199] (**Fig. S3A**). Briefly, tumors were placed on a 20 μm strainer
1051 (pluriSelect, catalog no. 43-50020-03) within a sterile 50 mL conical tube (FisherbrandTM,
1052 catalog no. 06-443-19) and centrifuged at 11,000g for 10 minutes at 4°C. TIF was col-
1053 lected from the conical tube, rapidly frozen in liquid nitrogen, and stored at -80°C. TIF
1054 volumes ranged from 5 to 100 μL, <20% of the tumors did not yield any fluid. The interval
1055 from euthanasia to centrifugation was <2 minutes per mouse.

1056

1057 **Harvest cells and conditioned media for ICP-MS and labile zinc quantification**

1058 For ICP-MS and labile zinc quantification, cells were seeded in 10 cm tissue culture
1059 dishes (Cellstar, catalog no. 82050-916) at densities of 500,000 and 300,000 cells per
1060 dish, respectively. Cells were seeded in complete media and incubated for 48 hours (see
1061 *Cell Lines and Culture Conditions* section for details). After this initial incubation, cells
1062 were washed twice with DPBS, and the media was replaced with 6 mL of FBS-free DMEM
1063 and Ham's F-12 50/50 media (Corning, catalog no. 10-092-CV) and incubated for an ad-
1064 ditional 24 hours. Conditioned media was filtered through a 0.45 µm filter (Fisherbrand™,
1065 catalog no. 09-720-005), aliquoted, snap-frozen in liquid nitrogen, and stored at -80°C
1066 until analysis. This conditioned media is referred to as "Media" in **Figs. 4C-E** and **Fig.**
1067 **S4C-F**.

1068

1069 For ICP-MS, attached cells were washed twice with ice-cold DPBS, scraped into 1 mL of
1070 80% methanol (Fisher Scientific, catalog no. A456-4) over dry ice, snap-frozen in liquid
1071 nitrogen, and stored at -80°C until analysis. For Labile Zinc Quantification, attached cells
1072 were washed twice with room-temperature DPBS, scraped into 1 mL of room-temperature
1073 DPBS, and immediately processed for staining. Six and three replicates per condition (for
1074 both cells and conditioned media) were harvested for ICP-MS and labile zinc quantifica-
1075 tion, respectively. In both cases, two additional plates were cultured in parallel to estimate
1076 the cell number at the end of the experiment, which was used to normalize zinc levels per
1077 cell. Cell counts were determined using a hemocytometer, by counting four squares in
1078 two independent aliquots taken from the same sample and averaging the results.

1079

1080 **Quantification of metals by mass spectrometry**

1081 Human (**Fig. 3F**) and Mouse Plasma and Mouse TIF (**Fig. 3A**) were collected as de-
1082 scribed in the *Isolation of Plasma and Tumor Interstitial Fluid (TIF)* section. *In vitro* cells
1083 and conditioned media were collected as outlined in the *Harvesting Cells and Conditioned*
1084 *Media for ICP-MS and Labile Zinc Quantification* section. For cells collected in 80% meth-
1085 anol, the methanol was evaporated to dryness under nitrogen gas prior to further pro-
1086 cessing. All samples including methanol-evaporated cells, conditioned media, TIF, and
1087 plasma, were spiked with 159Tb and 89Y (High-Purity Standards, catalog nos. 1057-1
1088 and 1067-1, respectively) as ISTDs to final concentrations of 0.2 ppb and 1 ppb, respec-
1089 tively. ISTDs were used to correct variations in sample preparation and to monitor fluctu-
1090 ations during the ICP-MS acquisition. Samples were digested with 250 µL of concentrated
1091 nitric acid (Fisher Chemical™, catalog no. A509P500) at 50°C for 16 hours. Following
1092 digestion, samples were diluted to a final volume of 5 mL with metal-free water (produced
1093 using a Milli-Q system, Millipore Sigma, catalog no. IQ7003). Multi-element metal stand-
1094 ard calibration curves were generated at the same time with each batch of samples, using
1095 a premixed metal ion stock solution (High-Purity Standards, catalog no. QCS-27-100),
1096 using the exact sample procedure as for the samples. The calibration curves used ½
1097 serial dilutions ranging from 250 ppb to 0.12 ppb and were spiked with same amount of
1098 ISTD as the samples. Quality controls were prepared by exactly same protocol as the
1099 samples and were ran at the beginning and the end of the analysis of each batch, to verify
1100 measurement accuracy thorough the batch. The limit of quantification for each metal was
1101 determined for each batch, and was usually 0.12 ppb or 0.24 ppb, depending on the

1102 batch. All solvents used in the protocol were of LC/MS or TraceMetal grade. All samples,
1103 including controls, were prepared in 15 mL polypropylene tubes (Fisher Scientific; catalog
1104 no. 14-955-238).
1105
1106 Metal quantification was performed using an iCAP RQ ICP-MS (Thermo Scientific, serial
1107 no. ICAPRQ01408) equipped with a Cetac ASX-560 autosampler (Teledyne Cetac Tech-
1108 nologies). The ICP-MS system was operated under constant argon plasma gas flow at
1109 110 psi. Elemental detection was performed in kinetic energy discrimination (KED) mode
1110 using helium gas at 17 psi. Data for each sample were acquired in triplicate, and averaged
1111 values were reported.
1112
1113 **Quantification of metabolite levels**
1114 Mouse TIF was collected as described in the *Isolation of Plasma and Tumor Interstitial*
1115 *Fluid (TIF)* section. LC/MS was performed using a QExactive orbitrap mass spectrometer
1116 using an Ion Max source and heated electrospray ionization (HESI) probe coupled with a
1117 Dionex Ultimate 3000 UPLC system (Thermo Fisher). External mass calibration was set
1118 every 7 days and internal mass calibration (lock masses) was not used. The mass spec-
1119 trometer was operated in full-scan, polarity switching mode with the spray voltage set to
1120 3.0 kV, the heated capillary held at 275 °C, and the HESI probe held at 350 °C. Seath
1121 gas flow rate was set to 40 units, the auxiliary gas flow at 15 units, and the sweep gas
1122 flow at 1 unit. Data acquisition was performed in a range of 70 to1000 *m/z*, with resolution
1123 set to 70,000, the AGC target at 1e6, and the maximum injection time at 20 milliseconds.
1124

1125 A library of 149 chemical standards of plasma polar metabolites was built as we have
1126 previously described (see first paragraph of *Quantification of metabolite levels in TIF and*
1127 *plasma* from the methods section in Sullivan MR et al. article[199]). Polar metabolites were
1128 extracted from 5 µL of each sample using 45 µL of a solvent mixture consisting of ace-
1129 tonitrile, methanol, and formic acid (75:25:0.1), which included isotopically labeled inter-
1130 nal standards (ISTDs) listed in **Table S7**. Samples were vortexed at 4°C for 10 minutes
1131 and centrifuged at 15,000g for 10 minutes to separate the supernatant containing soluble
1132 polar metabolites. Aliquots of 2 µL of sample were injected onto a ZIC-pHILIC (2.1x150
1133 mm) analytical column equipped with a guard column (2.1 x 20mm), both of 5 µm particle
1134 size (EMD Milipore, catalog no. 150454). Column was maintained at 25°C and the au-
1135 tosampler was set at 4°C. The mobile phase consisted of Buffer A (20 mM ammonium
1136 carbonate, 0.1% ammonium hydroxide), and Buffer B (acetonitrile). The chromatographic
1137 gradient was run at a flow rate of 0.150 mL/minute as follows: 0–20 min: linear gradient
1138 from 80% to 20% B; 20–20.5 min: linear gradient from 20% to 80% B; 20.5–28 min: hold
1139 at 80%. All solvents used in this protocol were LC/MS gradient.
1140
1141 Metabolite identification was performed using XCalibur 2.2 software (Thermo Fisher Sci-
1142 entific), applying a 5 ppm mass accuracy window and a 0.5-minute retention time window.
1143 External standard pools were used for metabolite peak identification based on *m/z* values
1144 and retention times. The limit of detection ranged from 100 nM to 3 µM, depending on the
1145 metabolite. For metabolite quantification, two methods were used: stable isotope dilution
1146 for metabolites with available ISTDs, and external standard calibration for those without
1147 Briefly, for stable isotope dilution quantification, peak areas of labeled ISTDs were

1148 compared to external standard pools to determine their concentration. The peak area of
1149 each unlabeled metabolite in the TIF and plasma samples was then compared to the
1150 quantified ISTDs to calculate metabolite concentrations. For metabolites without ISTDs,
1151 quantification by external calibration involved normalizing the peak area of each analyte
1152 to that of a labeled ISTD to account for sample recovery differences. This normalization
1153 was applied to both biological samples and external standard pool dilutions. A standard
1154 curve was generated from the normalized peak areas, with linear fits typically above r^2 =
1155 0.95. These curves were used to convert peak areas in TIF or plasma samples into me-
1156 tabolite concentrations. These results are considered semiquantitative due to matrix dif-
1157 ferences between external standards (prepared in water) and the samples. Please, refer
1158 to *Quantification of metabolite levels in TIF and plasma* from the methods section in Sul-
1159 livan MR et al. article[199] for more details.
1160

1161 **CRISPR Drop out Screen**

1162 The pooled mouse metabolic-focused CRISPR KO library was a gift from Dr. Kivanc Bir-
1163 soy (Addgene, catalog no. 160129). Fifteen million Yumm5.2 cells expressing sh*Cdkn2a*
1164 or control shGFP were infected with pooled CRISPR KO library to an MOI <0.25 to
1165 achieve ~500-fold library coverage after selection with 3 µg/mL puromycin. The cells were
1166 passaged every 2–3 days for two weeks, maintaining the full population, before implan-
1167 tation into mice. A total of 350,000 cells per mouse were injected into 36 mice per group,
1168 achieving a 550-fold library coverage. Mice were treated with either anti-Pd1 or IgG as
1169 described in the *Mice Treatments* section above. Once tumors reached 0.5 cm^3, they
1170 were harvested, and DNA was isolated using the Quick-DNA Miniprep Plus kit (Zymo

1171 Research, catalog no. D4069) following the manufacturer's instructions. DNA from each
1172 mouse in the same group was pooled and used for gRNA amplification. To ensure ade-
1173 quate gRNA representation, calculations from Wohlhieter et al.[200] were used to achieve
1174 >450-fold coverage. In brief, 64 µg of genomic DNA per condition was divided into 16
1175 PCR reactions, with 4 µg per reaction. The gRNA region was amplified using primers
1176 listed in **Table S8** and Ex Taq DNA polymerase (Takara, catalog no. RR001A) following
1177 the manufacturer's protocol. The PCR conditions were as follows: one cycle at 94 °C for
1178 2 minutes, followed by 30 cycles of 94 °C for 20 seconds, 63 °C for 30 seconds, and 72
1179 °C for 45 seconds, concluding with a final extension step at 72 °C for 1 minute. The reac-
1180 tion was performed in a thermal cycler (Bio-Rad, T100™ Thermal Cycler, serial no.
1181 621BR59583). The resulting PCR amplicons were purified using the Wizard® SV Gel and
1182 PCR Clean-Up System (Promega, catalog no. A9282) following the manufacturer's in-
1183 structions and pooled. The cleaned amplicons were sequenced using a NextSeq high
1184 output 75 cycle kit 1x50 in an Illumina NextSeq 500 (Serial no. NB: 501446). Data was
1185 analyzed using the MAGeCK bioinformatics pipeline to identify negatively enriched genes
1186 (Li et al., 2014). **Fig. 3C** shows the Log_2 fold change of the negative CRISPR score of
1187 solute carrier transporter in YUMM5.2 sh*Cdkn2a* tumors in mice treated with anti-Pd-1
1188 vs. IgG vs. shControl tumors in mice treated with anti-Pd-1 vs. IgG.
1189

1190 **Methyl-β-cyclodextrin (MβCD) treatment**

1191 Cells seeded in 12-well plates (Corning, catalog no. 3513) for immunofluorescence (IF)
1192 or in 6 cm plates (Falcon, catalog no. 353002) for flow cytometry were treated with 10
1193 mM MβCD (Sigma Aldrich, catalog no. C4555-10G) diluted in FBS-free DMEM and Ham's

1194 F-12 50/50 media (Corning, catalog no. 10-092-CV), supplemented with 10 mM HEPES
1195 (Gibco, catalog no. 15630080). The treatment was carried out for 1 hour at 37°C with 5%
1196 CO_2. After treatment, cells were collected for downstream analysis (i.e. IF or labile zinc
1197 quantification). Note that MβCD-treated cells are extremely loosely adhered, so washes
1198 must be done gently. To prevent cell loss during the immunofluorescence staining proce-
1199 dure, fixation time was increased to 20 minutes.
1200

1201 **Statin treatment**

1202 Two million cells were seeded in 10 cm dishes and treated with 1 μM Lovastatin (Selleck-
1203 chem, Cat. No. S2061), Atorvastatin (MedChemExpress, Cat. No. HY-B0589) or vehicle
1204 (DMSO). Cells were incubated for 4 days, with media replaced at 48 hours using fresh
1205 media containing corresponding treatment. At 72 hours, cells were trypsinized, and
1206 35,000 cells per condition were seeded onto coverslips in 12-well plates for immunofluo-
1207 rescence, using media containing corresponding treatment. In parallel, 1 million cells
1208 were seeded in 10 cm dishes in media containing corresponding treatment for intracellular
1209 labile zinc quantification. After 24 hours, cells on coverslips were washed, fixed, and
1210 stained (see *Immunofluorescence* section). Cells in 10 cm dishes were washed, scraped,
1211 and stained for labile zinc quantification (see *In Vitro Labile Zinc Quantification* section).
1212

1213 ***In vitro* labile Zinc quantification**

1214 Cells and conditioned media were collected as outlined in the *Harvesting Cells and Con-*
1215 *ditioned Media for ICP-MS and Labile Zinc Quantification* section. One million scraped
1216 cells were pelleted in a round-bottom 96-well plate (Corning, catalog no. 3366) by

1217 centrifugation at 350 g for 5 minutes at 4°C. Cells were then stained with 50 μM Zinpyr-1
1218 (Cayman Chemical, catalog no. 15122) diluted in DPBS, containing a 1:1000 dilution of
1219 Live/Dead Fixable Near-IR Dead Cell Stain kit (Invitrogen, catalog no. L34976), in a final
1220 volume of 50 μL for 20 minutes at 4°C, protected from light. Following staining, cells were
1221 fixed in 4% paraformaldehyde (Sigma Aldrich, catalog no. 158127-3Kg) for 15 minutes at
1222 4°C, shielded from light, and resuspended in FACS buffer (1x PBS, 10 mM HEPES
1223 [Gibco, catalog no. 15630080], 1% heat-inactivated FBS [Sigma Aldrich, catalog no.
1224 F4135-100ML], 0.05% sodium azide [Sigma Aldrich, catalog no. S2002-25G]). Stained
1225 cells were immediately analyzed on a CytoFlex Flow Cytometer (Beckman Coulter, serial
1226 no. 822338373). Flow cytometry data were analyzed with FlowJo version 10. The median
1227 fluorescence intensity (MFI) of single live cells was measured to assess intracellular zinc
1228 levels per sample.
1229
1230 Labile zinc concentration was measured as previously described[201]. Briefly, 50 μL of con-
1231 ditioned media was mixed with 50 μL of 50 μM Zinpyr-1 (Cayman Chemical, catalog no.
1232 15122) in a 96-well polystyrene microplate (Greiner Bio-One, catalog no. 655101). The
1233 mixture was incubated for 20 minutes at 37°C in a CO_2 incubator. Fluorescence was then
1234 measured in a fluorescent plate reader (Promega GloMax explorer, serial no.
1235 9720100141) with excitation at 475 nm and emission at 500-550 nm. This first fluores-
1236 cence measurement reflects the signal of Zinpyr-1 bound to zinc in the sample (F). To
1237 determine the baseline fluorescence, 50 μL of 600 μM of the zinc chelator N,N,N',N'-
1238 tetrakis(2-pyridinylmethyl)-1,2-ethanediamine (TPEN, MilliporeSigma, catalog no.
1239 6163941100MG), was added to each well. After another 20-minute incubation at 37°C in

1240 a CO_2 incubator, fluorescence was measured again, representing the minimum fluores-
1241 cence (F_{min}) due to the chelation of zinc. Finally, to obtain the maximum fluorescence
1242 (F_{max}), 50 µL of 2 mM $ZnSO_4$ (Sigma Aldrich, catalog no. Z2876-500ML) was added to
1243 each well. After a final 20-minute incubation at 37°C in a CO_2 incubator, the fluorescence
1244 was measured one last time. The zinc concentration in each sample was then calculated
1245 using the formula: Zn^{2+} concentration = $K_D \times ((F - Fmin) / (Fmax - F))$, where K_D is the
1246 dissociation constant of the zinc:Zinpyr-1 complex (0.7 nM)[201]. Finally, zinc concentra-
1247 tions were normalized to the number of cells in each sample at the time of harvesting.
1248

1249 **Immunofluorescence (IF)**

1250 Approximately 30,000 to 50,000 cells were seeded onto coverslips in 12-well plates
1251 (Corning, catalog no. 3513) and incubated at 37°C with 5% CO_2. Because Yumm1.7 cells
1252 have low attachment properties, these cells were seeded onto poly-L-ornithine-coated
1253 coverslips. Briefly, coverslips were first washed with 2 mL of 200 proof ethanol (Decon
1254 Labs) for 5 minutes, followed by two washes with molecular-grade water (Corning, catalog
1255 no. 46000CM). Then, 500 µL of poly-L-ornithine (Sigma Aldrich, catalog no. P4957-50mL)
1256 was added to each well containing a coverslip. The plates were sealed with parafilm
1257 (VWR, catalog no. 52858-032) to prevent evaporation, and incubated overnight at 37°C.
1258 Before seeding the cells, the coverslips were washed three times with 1 mL of molecular-
1259 grade water and air-dried for 10 minutes. Approximately 16 hours after seeding, the cells
1260 were fixed with 4% paraformaldehyde (Sigma Aldrich, catalog no. 158127-3Kg) for 10
1261 minutes followed by permeabilized with 0.2% Triton X-100 (VWR, catalog no. 97062-208)
1262 for 5 minutes. For plasma membrane staining of SLC39A9, however, permeabilization

1263 was omitted. The cells were then blocked with 5 µg/mL of Cd16/Cd32 (Invitrogen, catalog
1264 no. 14016185) diluted in 3% BSA/PBS (Fisher BioReagents, catalog no. BP1600) for 10
1265 minutes. Both human and mouse cells were subsequently incubated with 10 µg/mL of
1266 anti-Slc39a9 (Thermo Scientific, catalog no. PA521074), diluted in 3% BSA/PBS for 1
1267 hour. After incubation, the cells were washed three times with PBS and then incubated
1268 with 0.75 µg/mL of secondary anti-rabbit Cy3-conjugated antibody (Jackson Immu-
1269 noResearch, catalog no. 111-165-003), diluted in 3% BSA/PBS for 1 hour in the dark.
1270 Cells were then washed 10 times with PBS and permeabilized with 0.2% Triton X-100 for
1271 5 minutes. Cells were stained with 0.15 µg/mL DAPI (diluted in PBS) for 1 minute. Finally,
1272 coverslips were mounted (Sigma Aldrich, catalog no. F6182-20ML) and sealed with trans-
1273 parent nail polish. Controls included staining with 10 µg/mL normal rabbit IgG (Cell Sig-
1274 naling, catalog no. 2729) and secondary-only staining.
1275
1276 For filipin staining cells were cultured on coverslips and fixed with 4% paraformaldehyde
1277 for 10 minutes. Cells were incubated with 0.1 mg/mL filipin III (Cayman Chemicals, cata-
1278 log no. 70440) for 1h at room temperature. Coverslips were mounted and sealed with
1279 transparent nail polish. Of note that Yumm1.7 cells were seeded in media containing lipid-
1280 depleted FBS (Omega Scientific, catalog no. FB-50).
1281
1282 Five to ten images were captured per condition using an inverted microscope (Nikon
1283 ECLIPSE Ti2, serial no. 542740) equipped with a 20x/0.17 objective (Nikon DIC N2 Plan
1284 Apo), a digital camera (ORCA-Fusion, catalog no. C1440-20UP, serial no. 000670) and
1285 the NIS-Elements AR software. Image analysis was conducted using Python (v. 3.10).

1286 SLC39A9 quantification was performed as follows: Nuclear staining images (DAPI) were
1287 normalized to the 3rd and 97th percentiles before segmentation, which was carried out
1288 using a pre-trained CellPose model ("cyto")[202]. Nuclei touching the image borders were
1289 excluded from further analysis. The mean Cy3 fluorescence signal (anti-SLC39A9) was
1290 quantified within the nuclear regions. Background signal was corrected by subtracting the
1291 median intensity of the entire image. Finally, the number of cells per condition was ran-
1292 domized, and 200 cells per condition were plotted as fold change relative to the control
1293 condition. Filipin quantification was performed as follows: Individual cells were defined as
1294 regions of interest (ROIs) and captured using image thresholding. Analysis was con-
1295 ducted using the 'Analyze Particles' tool in ImageJ (Fiji), excluding cells at the image pe-
1296 riphery. Integrated Density values were determined for each ROI. A total of at least 100
1297 cells per condition were analyzed, and data are presented as fold change relative to the
1298 control condition.
1299
1300 **Western Blotting**
1301 Cell lysates were collected in 1X sample buffer [2% SDS (Millipore Sigma, catalog no.
1302 75746-1Kg), 10% glycerol (Sigma Aldrich, catalog no. G5516), 0.01% bromophenol blue
1303 (Millipore Sigma, catalog no. BX1410), 62.5 mM Tris (Fisher Scientific, catalog no.
1304 AAJ65594A1), pH=6.8 and 0.1 M DTT (Thermo Fisher, catalog no. 15508-013)] and
1305 boiled at 95° C for 10 minutes. Protein concentration was determined using Bradford as-
1306 say (Bio-Rad, catalog no. 5000006) following manufacturer's instructions. Proteins were
1307 resolved using SDS-PAGE gels and transferred to nitrocellulose membranes (GE
1308 Healthcare Life Sciences, catalog no. 10600001) as previously described[54]. Antibodies

1309 used include: anti human p16 (Abcam, catalog no. ab108349, working concentration 1.5
1310 µg/mL), mouse anti-p16 (Cell Signaling Technology, catalog no. 29271S, working con-
1311 centration 1 µg/mL), anti-p19 (Abcam, catalog no. ab80, working concentration 1 µg/mL),
1312 anti-β-Actin (Sigma-Aldrich, catalog no. A1978, working concentration 1 µg/mL), anti-
1313 mouse HRP (Cell Signaling Technology, catalog no. 7076, working concentration 0.1
1314 µg/mL), and anti-rabbit HRP (Cell Signaling Technology, catalog no. 7074, , working con-
1315 centration 0.2 µg/mL).
1316
1317 **Bulk RNA-Seq and RT-qPCR**
1318 Total RNA was extracted from cells with Trizol (Ambion, catalog no. 15596018) and
1319 DNase treated, cleaned, and concentrated using Zymo columns (Zymo Research, cata-
1320 log no. R1013) following the manufacturer's instructions. Optical density values for RNA
1321 were measured using NanoDrop One (Thermo Scientific) to confirm an A260 and A280
1322 ratios above 1.9. For bulk RNA-Seq, RNA integrity number (RIN) was measured using
1323 BioAnalyzer (Agilent Technologies; RRID:SCR_019715) RNA 6000 Nano Kit to confirm
1324 RIN above 7 for each sample. The cDNA libraries, next-generation sequencing, and bio-
1325 informatics analysis was performed by Novogene. Differential expression analysis was
1326 done using DESeq (v2_1.6.3). Raw and processed RNA-seq data can be found on Gene
1327 Expression Omnibus (GSE295787).
1328
1329 For RT-qPCR, a total of 2 µg of RNA was reverse-transcribed to cDNA (Applied Biosys-
1330 tems, catalog no. A25742) following manufacturer's instructions in a thermal cycler (Bio-
1331 Rad, T100™ Thermal Cycler, serial no. 621BR59583). Relative expression of target

1332 genes was analyzed using the Real-Time PCR System (Bio-Rad, CFX Connect, serial
1333 no. 788BR09362) with clear 96-well plates (Greiner Bio-One, catalog no. 652240). Pri-
1334 mers were designed using the Integrated DNA Technologies (IDT) web tool (**Table S8**).
1335 Conditions for amplification were: 5 min at 95° C, 40 cycles of 10 sec at 95° C and 7 sec
1336 at 62° C. The assay ended with a melting curve program: 15 sec at 95° C, 1 min at 70°
1337 C, then ramping to 95° C while continuously monitoring fluorescence. Each sample was
1338 assessed in triplicate. Relative quantification was determined to multiple reference genes
1339 (Rplp0, Gusb, and Rp132) to ensure reproducibility using the delta-delta CT method.
1340

1341 **Senescence and proliferation assays**

1342 SA-β-Gal staining was performed as previously described[203]. Cells were fixed in a mixture
1343 of 2% formaldehyde (Fisher Scientific, catalog no. BP531-500) and 0.2% glutaraldehyde
1344 (Fisher Scientific, catalog no. 01909-100) diluted in PBS for 5 minutes, followed by stain-
1345 ing with a staining cocktail containing: 40 mM Na_2HPO_4 (Sigma Aldrich, catalog no.
1346 567547), 150 mM NaCl (Sigma Aldrich, catalog no. S5886), 2 mM $MgCl_2$ (Sigma Aldrich,
1347 catalog no. M1028), 5Mm $K_3Fe(CN)_6$ (Sigma Aldrich, catalog no. 244023), 5 mM
1348 $K_4Fe(CN)_6$ (Sigma Aldrich, catalog no. 455989), and 1 mg/ml 5-Bromo-4-chloro-3-indolyl
1349 β-D-galactopyranoside (Sigma Aldrich, catalog no. B4252). Staining was incubated over-
1350 night at 37° C in a non-CO2 incubator after which reaction was stopped with tap water.
1351 Images were acquired immediately upon reaction stopped using an inverted microscope
1352 (Nikon Eclipse Ts2, serial no. 139045) with a 20X/0.40 objective (Nikon LWD) equipped
1353 with a camera (Nikon DS-Fi3). Each sample was assessed in triplicate and at least 100
1354 cells per well were counted (>300 cells per experiment). For colony formation, an equal

1355 number of cells were seeded in 12-well plates and cultured for an additional 1-2 weeks.
1356 Colony formation was visualized by fixing cells in 1% paraformaldehyde for 5 minutes
1357 followed by staining with 0.05% crystal violet for 20 minutes on rocking. Wells were de-
1358 stained in 500mL 10% acetic acid for 10 minutes on rocking and absorbance (590 nm)
1359 measured using a spectrophotometer (Promega GloMax explorer, serial no.
1360 9720100141). Each sample was assessed in triplicate.
1361

1362 **Qualification and Statistical analysis**

1363 GraphPad Prism version 10.0 was used to perform statistical analysis. The level of sig-
1364 nificance between two groups was assessed with pared or unpaired Student's *t* test as
1365 necessary and indicated in figure caption. For data sets with more than two groups, one-
1366 way ANOVA followed by Šidák correction for multiple comparisons was applied. For lon-
1367 gitudinal tumor growth studies mixed-effects model was used and Šidák correction for
1368 multiple comparisons was applied. For survival analysis log-rank (Mantel-Cox) test was
1369 used. Pearson correlation was used to assess correlation. P-values <0.05 were consid-
1370 ered significant. Specific statistical details used in scRNA-Seq and bulk RNA-Seq data
1371 are included in the corresponding section.

REFERENCES

1 Han, G. *et al.* 9p21 loss confers a cold tumor immune microenvironment and primary resistance to immune checkpoint therapy. *Nature communications* **12**, 5606 (2021). https://doi.org:10.1038/s41467-021-25894-9

2 Tu, Z. *et al.* The cell senescence regulator p16 is a promising cancer prognostic and immune check-point inhibitor (ICI) therapy biomarker. *Aging (Albany NY)* **15**, 2136-2157 (2023). https://doi.org:10.18632/aging.204601

3 Deng, C. *et al.* Pan-cancer analysis of CDKN2A alterations identifies a subset of gastric cancer with a cold tumor immune microenvironment. *Hum Genomics* **18**, 55 (2024). https://doi.org:10.1186/s40246-024-00615-7

4 Fan, K., Dong, Y., Li, T. & Li, Y. Cuproptosis-associated CDKN2A is targeted by plicamycin to regulate the microenvironment in patients with head and neck squamous cell carcinoma. *Front Genet* **13**, 1036408 (2022). https://doi.org:10.3389/fgene.2022.1036408

5 Luo, J. P., Wang, J. & Huang, J. H. CDKN2A is a prognostic biomarker and correlated with immune infiltrates in hepatocellular carcinoma. *Biosci Rep* **41** (2021). https://doi.org:10.1042/BSR20211103

6 Chen, Z. *et al.* Comprehensive Analysis Revealed that CDKN2A is a Biomarker for Immune Infiltrates in Multiple Cancers. *Front Cell Dev Biol* **9**, 808208 (2021). https://doi.org:10.3389/fcell.2021.808208

7 Gutiontov, S. I. *et al.* CDKN2A loss-of-function predicts immunotherapy resistance in non-small cell lung cancer. *Scientific reports* **11**, 20059 (2021). https://doi.org:10.1038/s41598-021-99524-1

8 Yu, J. *et al.* Genetic Aberrations in the CDK4 Pathway Are Associated with Innate Resistance to PD-1 Blockade in Chinese Patients with Non-Cutaneous Melanoma. *Clin Cancer Res* **25**, 6511-6523 (2019). https://doi.org:10.1158/1078-0432.CCR-19-0475

9 Adib, E. *et al.* CDKN2A Alterations and Response to Immunotherapy in Solid Tumors. *Clin Cancer Res* **27**, 4025-4035 (2021). https://doi.org:10.1158/1078-0432.CCR-21-0575

10 Liu, S. *et al.* Response and recurrence correlates in individuals treated with neoadjuvant anti-PD-1 therapy for resectable oral cavity squamous cell carcinoma. *Cell Rep Med* **2**, 100411 (2021). https://doi.org:10.1016/j.xcrm.2021.100411

11 Peng, Y. *et al.* Co-occurrence of CDKN2A/B and IFN-I homozygous deletions correlates with an immunosuppressive phenotype and poor prognosis in lung adenocarcinoma. *Mol Oncol* **16**, 1746-1760 (2022). https://doi.org:10.1002/1878-0261.13206

12 Zhao, L., Zhou, X., Li, H., Yin, T. & Jiang, Y. Prognosis of immunotherapy for non-small cell lung cancer with CDKN2A loss of function. *J Thorac Dis* **16**, 507-515 (2024). https://doi.org:10.21037/jtd-23-1017

13 Leon, K. E., Tangudu, N. K., Aird, K. M. & Buj, R. Loss of p16: A Bouncer of the Immunological Surveillance? *Life (Basel)* **11** (2021). https://doi.org:10.3390/life11040309

14 Banchereau, R. *et al.* Molecular determinants of response to PD-L1 blockade across tumor types. *Nat Commun* **12**, 3969 (2021). https://doi.org:10.1038/s41467-021-24112-w

15 Wang, S. *et al.* Loss of CDKN2A Enhances the Efficacy of Immunotherapy in EGFR Mutant Non-Small Cell Lung Cancer. *Cancer Res* (2024). https://doi.org:10.1158/0008-5472.CAN-24-1817

16 Xue, L. *et al.* Next-generation sequencing identifies CDKN2A alterations as prognostic biomarkers in recurrent or metastatic head and neck squamous cell carcinoma predominantly receiving immune checkpoint inhibitors. *Front Oncol* **13**, 1276009 (2023). https://doi.org:10.3389/fonc.2023.1276009

17 Jang, H. J. *et al.* Inhibition of Cyclin Dependent Kinase 4/6 Overcomes Primary Resistance to Programmed Cell Death 1 Blockade in Malignant Mesothelioma. *Ann Thorac Surg* **114**, 1842-1852 (2022). https://doi.org:10.1016/j.athoracsur.2021.08.054

18 Buj, R., Leon, K. E., Anguelov, M. A. & Aird, K. M. Suppression of p16 alleviates the senescence-associated secretory phenotype. *Aging (Albany NY)* **13**, 3290-3312 (2021). https://doi.org:10.18632/aging.202640

19 Brahmer, J. R. *et al.* Safety and activity of anti-PD-L1 antibody in patients with advanced cancer. *N Engl J Med* **366**, 2455-2465 (2012). https://doi.org:10.1056/NEJMoa1200694

20 Topalian, S. L. *et al.* Safety, activity, and immune correlates of anti-PD-1 antibody in cancer. *N Engl J Med* **366**, 2443-2454 (2012). https://doi.org:10.1056/NEJMoa1200690

21 Wolchok, J. D. *et al.* Final, 10-Year Outcomes with Nivolumab plus Ipilimumab in Advanced Melanoma. *N Engl J Med* (2024). https://doi.org:10.1056/NEJMoa2407417

22 Finn, R. S. *et al.* Atezolizumab plus Bevacizumab in Unresectable Hepatocellular Carcinoma. *N Engl J Med* **382**, 1894-1905 (2020). https://doi.org:10.1056/NEJMoa1915745

23 Herbst, R. S. *et al.* Atezolizumab for First-Line Treatment of PD-L1-Selected Patients with NSCLC. *N Engl J Med* **383**, 1328-1339 (2020). https://doi.org:10.1056/NEJMoa1917346

24 Pardoll, D. M. The blockade of immune checkpoints in cancer immunotherapy. *Nat Rev Cancer* **12**, 252-264 (2012). https://doi.org:10.1038/nrc3239

25 Moore, J. *et al.* Identification of a conserved subset of cold tumors responsive to immune checkpoint blockade. *J Immunother Cancer* **13** (2025). https://doi.org:10.1136/jitc-2024-010528

26 Rappold, P. M. *et al.* A Targetable Myeloid Inflammatory State Governs Disease Recurrence in Clear-Cell Renal Cell Carcinoma. *Cancer Discov* **12**, 2308-2329 (2022). https://doi.org:10.1158/2159-8290.CD-21-0925

27 Rashidian, M. *et al.* Immuno-PET identifies the myeloid compartment as a key contributor to the outcome of the antitumor response under PD-1 blockade. *Proc Natl Acad Sci U S A* **116**, 16971-16980 (2019). https://doi.org:10.1073/pnas.1905005116

28 Bader, J. E. *et al.* Obesity induces PD-1 on macrophages to suppress anti-tumour immunity. *Nature* **630**, 968-975 (2024). https://doi.org:10.1038/s41586-024-07529-3

29 Gordon, S. R. *et al.* PD-1 expression by tumour-associated macrophages inhibits phagocytosis and tumour immunity. *Nature* **545**, 495-499 (2017). https://doi.org:10.1038/nature22396

30 Coulton, A. *et al.* Using a pan-cancer atlas to investigate tumour associated macrophages as regulators of immunotherapy response. *Nat Commun* **15**, 5665 (2024). https://doi.org:10.1038/s41467-024-49885-8

31 Strauss, L. *et al.* Targeted deletion of PD-1 in myeloid cells induces antitumor immunity. *Sci Immunol* **5** (2020). https://doi.org:10.1126/sciimmunol.aay1863

32 Kim, I. S. *et al.* Immuno-subtyping of breast cancer reveals distinct myeloid cell profiles and immunotherapy resistance mechanisms. *Nature cell biology* **21**, 1113-1126 (2019). https://doi.org:10.1038/s41556-019-0373-7

33 Yu, J. *et al.* Liver metastasis restrains immunotherapy efficacy via macrophage-mediated T cell elimination. *Nature medicine* **27**, 152-164 (2021). https://doi.org:10.1038/s41591-020-1131-x

34 Zhang, Y. *et al.* Myeloid cells are required for PD-1/PD-L1 checkpoint activation and the establishment of an immunosuppressive environment in pancreatic cancer. *Gut* **66**, 124-136 (2017). https://doi.org:10.1136/gutjnl-2016-312078

35 Davar, D. *et al.* Neoadjuvant vidutolimod and nivolumab in high-risk resectable melanoma: A prospective phase II trial. *Cancer Cell* **42**, 1898-1918 e1812 (2024). https://doi.org:10.1016/j.ccell.2024.10.007

36 Shen, L. *et al.* PD-1/PD-L pathway inhibits M.tb-specific CD4(+) T-cell functions and phagocytosis of macrophages in active tuberculosis. *Sci Rep* **6**, 38362 (2016). https://doi.org:10.1038/srep38362

37 Wang, L. *et al.* PD-L1-expressing tumor-associated macrophages are immunostimulatory and associate with good clinical outcome in human breast cancer. *Cell Rep Med* **5**, 101420 (2024). https://doi.org:10.1016/j.xcrm.2024.101420

38 Li, C. W., Lai, Y. J., Hsu, J. L. & Hung, M. C. Activation of phagocytosis by immune checkpoint blockade. *Front Med* **12**, 473-480 (2018). https://doi.org:10.1007/s11684-018-0657-5

39 Liu, M. *et al.* Metabolic rewiring of macrophages by CpG potentiates clearance of cancer cells and overcomes tumor-expressed CD47-mediated 'don't-eat-me' signal. *Nat Immunol* **20**, 265-275 (2019). https://doi.org:10.1038/s41590-018-0292-y

40 Ring, N. G. *et al.* Anti-SIRPalpha antibody immunotherapy enhances neutrophil and macrophage antitumor activity. *Proc Natl Acad Sci U S A* **114**, E10578-E10585 (2017). https://doi.org:10.1073/pnas.1710877114

41 Gonzalez, M. A. *et al.* Phagocytosis increases an oxidative metabolic and immune suppressive signature in tumor macrophages. *J Exp Med* **220** (2023). https://doi.org:10.1084/jem.20221472

42 Kamb, A. *et al.* A cell cycle regulator potentially involved in genesis of many tumor types. *Science* **264**, 436-440 (1994). https://doi.org:10.1126/science.8153634

43 Nobori, T. *et al.* Deletions of the cyclin-dependent kinase-4 inhibitor gene in multiple human cancers. *Nature* **368**, 753-756 (1994). https://doi.org:10.1038/368753a0

44 Sherr, C. J. Cancer cell cycles. *Science* **274**, 1672-1677 (1996). https://doi.org:10.1126/science.274.5293.1672

45 Hall, M. & Peters, G. Genetic alterations of cyclins, cyclin-dependent kinases, and Cdk inhibitors in human cancer. *Adv Cancer Res* **68**, 67-108 (1996). https://doi.org:10.1016/s0065-230x(08)60352-8

46 Cairns, P. *et al.* Rates of p16 (MTS1) mutations in primary tumors with 9p loss. *Science* **265**, 415-417 (1994). https://doi.org:10.1126/science.8023167

47 Herman, J. G. *et al.* Inactivation of the CDKN2/p16/MTS1 gene is frequently associated with aberrant DNA methylation in all common human cancers. *Cancer Res* **55**, 4525-4530 (1995).

48 Ranade, K. *et al.* Mutations associated with familial melanoma impair p16INK4 function. *Nat Genet* **10**, 114-116 (1995). https://doi.org:10.1038/ng0595-114

49 Zhao, R., Choi, B. Y., Lee, M. H., Bode, A. M. & Dong, Z. Implications of Genetic and Epigenetic Alterations of CDKN2A (p16(INK4a)) in Cancer. *EBioMedicine* **8**, 30-39 (2016). https://doi.org:10.1016/j.ebiom.2016.04.017

50 Sherr, C. J. The INK4a/ARF network in tumour suppression. *Nat Rev Mol Cell Biol* **2**, 731-737 (2001). https://doi.org:10.1038/35096061

51 Serrano, M., Hannon, G. J. & Beach, D. A new regulatory motif in cell-cycle control causing specific inhibition of cyclin D/CDK4. *Nature* **366**, 704-707 (1993). https://doi.org:10.1038/366704a0 [doi]

52 Serrano, M., Lin, A. W., McCurrach, M. E., Beach, D. & Lowe, S. W. Oncogenic ras provokes premature cell senescence associated with accumulation of p53 and p16INK4a. *Cell* **88**, 593-602 (1997). https://doi.org:10.1016/s0092-8674(00)81902-9

53 Buj, R. & Aird, K. M. p16: cycling off the beaten path. *Mol Cell Oncol* **6**, e1677140 (2019). https://doi.org:10.1080/23723556.2019.1677140

54 Buj, R. *et al.* Suppression of p16 Induces mTORC1-Mediated Nucleotide Metabolic Reprogramming. *Cell Rep* **28**, 1971-1980 e1978 (2019). https://doi.org:10.1016/j.celrep.2019.07.084

55 Tangudu, N. K. *et al.* De Novo Purine Metabolism is a Metabolic Vulnerability of Cancers with Low p16 Expression. *Cancer Res Commun* **4**, 1174-1188 (2024). https://doi.org:10.1158/2767-9764.Crc-23-0450

56 Tangudu, N. K. *et al.* ATR promotes mTORC1 activity via de novo cholesterol synthesis. *EMBO Rep* (2025). https://doi.org:10.1038/s44319-025-00451-3

57 Wolff, B. & Naumann, M. INK4 cell cycle inhibitors direct transcriptional inactivation of NF-kappaB. *Oncogene* **18**, 2663-2666 (1999). https://doi.org:10.1038/sj.onc.1202617

58 Tyagi, E. *et al.* Loss of p16(INK4A) stimulates aberrant mitochondrial biogenesis through a CDK4/Rb-independent pathway. *Oncotarget* **8**, 55848-55862 (2017). https://doi.org:10.18632/oncotarget.19862

59 Jenkins, N. C. *et al.* The p16(INK4A) tumor suppressor regulates cellular oxidative stress. *Oncogene* **30**, 265-274 (2011). https://doi.org:10.1038/onc.2010.419

60 Choi, B. Y. *et al.* The tumor suppressor p16(INK4a) prevents cell transformation through inhibition of c-Jun phosphorylation and AP-1 activity. *Nat Struct Mol Biol* **12**, 699-707 (2005). https://doi.org:10.1038/nsmb960

61 Lee, M. H. *et al.* Tumor suppressor p16(INK4a) inhibits cancer cell growth by downregulating eEF1A2 through a direct interaction. *J Cell Sci* **126**, 1744-1752 (2013). https://doi.org:10.1242/jcs.113613

62 Al-Khalaf, H. H., Mohideen, P., Nallar, S. C., Kalvakolanu, D. V. & Aboussekhra, A. The cyclin-dependent kinase inhibitor p16INK4a physically interacts with transcription factor Sp1 and cyclin-dependent kinase 4 to transactivate microRNA-141 and microRNA-146b-5p spontaneously and in response to ultraviolet light-induced DNA damage. *J Biol Chem* **288**, 35511-35525 (2013). https://doi.org:10.1074/jbc.M113.512640

63 Murakami, Y., Mizoguchi, F., Saito, T., Miyasaka, N. & Kohsaka, H. p16(INK4a) exerts an anti-inflammatory effect through accelerated IRAK1 degradation in macrophages. *J Immunol* **189**, 5066-5072 (2012). https://doi.org:10.4049/jimmunol.1103156

64 Hu, Y. *et al.* Dual roles of hexokinase 2 in shaping microglial function by gating glycolytic flux and mitochondrial activity. *Nat Metab* **4**, 1756-1774 (2022). https://doi.org:10.1038/s42255-022-00707-5

65 Davies, L. C. *et al.* Peritoneal tissue-resident macrophages are metabolically poised to engage microbes using tissue-niche fuels. *Nat Commun* **8**, 2074 (2017). https://doi.org:10.1038/s41467-017-02092-0

66 Sugimoto, R. *et al.* Zinc Deficiency as a General Feature of Cancer: a Review of the Literature. *Biol Trace Elem Res* **202**, 1937-1947 (2024). https://doi.org:10.1007/s12011-023-03818-6

67 Kiouri, D. P. *et al.* Multifunctional role of zinc in human health: an update. *EXCLI J* **22**, 809-827 (2023). https://doi.org:10.17179/excli2023-6335

68 Mehta, A. J., Yeligar, S. M., Elon, L., Brown, L. A. & Guidot, D. M. Alcoholism causes alveolar macrophage zinc deficiency and immune dysfunction. *Am J Respir Crit Care Med* **188**, 716-723 (2013). https://doi.org:10.1164/rccm.201301-0061OC

69 Wirth, J. J., Fraker, P. J. & Kierszenbaum, F. Zinc requirement for macrophage function: effect of zinc deficiency on uptake and killing of a protozoan parasite. *Immunology* **68**, 114-119 (1989).

70 Sheikh, A. *et al.* Zinc influences innate immune responses in children with enterotoxigenic Escherichia coli-induced diarrhea. *J Nutr* **140**, 1049-1056 (2010). https://doi.org:10.3945/jn.109.111492

71 Hall, S. C. *et al.* Critical Role of Zinc Transporter (ZIP8) in Myeloid Innate Immune Cell Function and the Host Response against Bacterial Pneumonia. *J Immunol* **207**, 1357-1370 (2021). https://doi.org:10.4049/jimmunol.2001395

72 Kitamura, H. *et al.* Toll-like receptor-mediated regulation of zinc homeostasis influences dendritic cell function. *Nat Immunol* **7**, 971-977 (2006). https://doi.org:10.1038/ni1373

73 Mocchegiani, E. *et al.* Metallothioneins/PARP-1/IL-6 interplay on natural killer cell activity in elderly: parallelism with nonagenarians and old infected humans. Effect of zinc supply. *Mech Ageing Dev* **124**, 459-468 (2003). https://doi.org:10.1016/s0047-6374(03)00023-x

74 Aydemir, T. B., Blanchard, R. K. & Cousins, R. J. Zinc supplementation of young men alters metallothionein, zinc transporter, and cytokine gene expression in leukocyte populations. *Proceedings of the National Academy of Sciences of the United States of America* **103**, 1699-1704 (2006). https://doi.org:10.1073/pnas.0510407103

75 Shi, H. N., Scott, M. E., Stevenson, M. M. & Koski, K. G. Energy restriction and zinc deficiency impair the functions of murine T cells and antigen-presenting cells during gastrointestinal nematode infection. *J Nutr* **128**, 20-27 (1998). https://doi.org:10.1093/jn/128.1.20

76 Jeong, J. & Eide, D. J. The SLC39 family of zinc transporters. *Mol Aspects Med* **34**, 612-619 (2013). https://doi.org:10.1016/j.mam.2012.05.011

77 Huang, L. & Tepaamorndech, S. The SLC30 family of zinc transporters - a review of current understanding of their biological and pathophysiological roles. *Mol Aspects Med* **34**, 548-560 (2013). https://doi.org:10.1016/j.mam.2012.05.008

78 Ren, X. *et al.* SLC39A10 promotes malignant phenotypes of gastric cancer cells by activating the CK2-mediated MAPK/ERK and PI3K/AKT pathways. *Exp Mol Med* **55**, 1757-1769 (2023). https://doi.org:10.1038/s12276-023-01062-5

79 Li, M. *et al.* Aberrant expression of zinc transporter ZIP4 (SLC39A4) significantly contributes to human pancreatic cancer pathogenesis and progression. *Proc Natl Acad Sci U S A* **104**, 18636-18641 (2007). https://doi.org:10.1073/pnas.0709307104

80 Cheng, X. *et al.* Zinc transporter SLC39A13/ZIP13 facilitates the metastasis of human ovarian cancer cells via activating Src/FAK signaling pathway. *J Exp Clin Cancer Res* **40**, 199 (2021). https://doi.org:10.1186/s13046-021-01999-3

81 Hogstrand, C., Kille, P., Ackland, M. L., Hiscox, S. & Taylor, K. M. A mechanism for epithelial-mesenchymal transition and anoikis resistance in breast cancer triggered by zinc channel ZIP6 and STAT3 (signal transducer and activator of transcription 3). *Biochem J* **455**, 229-237 (2013). https://doi.org:10.1042/BJ20130483

82 Cheng, X. *et al.* Solute Carrier Family 39 Member 6 Gene Promotes Aggressiveness of Esophageal Carcinoma Cells by Increasing Intracellular Levels of Zinc, Activating Phosphatidylinositol 3-Kinase Signaling, and Up-regulating Genes That Regulate Metastasis. *Gastroenterology* **152**, 1985-1997 e1912 (2017). https://doi.org:10.1053/j.gastro.2017.02.006

83 Liu, M. *et al.* ZIP4 Promotes Pancreatic Cancer Progression by Repressing ZO-1 and Claudin-1 through a ZEB1-Dependent Transcriptional Mechanism. *Clin Cancer Res* **24**, 3186-3196 (2018). https://doi.org:10.1158/1078-0432.CCR-18-0263

84 Thomas, P., Pang, Y. & Dong, J. Ligand-independent signaling and migration of breast cancer cells expressing membrane androgen receptor, ZIP9 (SLC39A9). *Mol Cell Endocrinol* **578**, 112060 (2023). https://doi.org:10.1016/j.mce.2023.112060

85 Prasad, A. S. *et al.* Nutritional and zinc status of head and neck cancer patients: an interpretive review. *J Am Coll Nutr* **17**, 409-418 (1998). https://doi.org:10.1080/07315724.1998.10718787

86 Federico, A. *et al.* Effects of selenium and zinc supplementation on nutritional status in patients with cancer of digestive tract. *Eur J Clin Nutr* **55**, 293-297 (2001). https://doi.org:10.1038/sj.ejcn.1601157

87 Xie, Y. *et al.* Higher serum zinc levels may reduce the risk of cervical cancer in Asian women: A meta-analysis. *J Int Med Res* **46**, 4898-4906 (2018). https://doi.org:10.1177/0300060518805600

88 Lin, S. & Yang, H. Ovarian cancer risk according to circulating zinc and copper concentrations: A meta-analysis and Mendelian randomization study. *Clin Nutr* **40**, 2464-2468 (2021). https://doi.org:10.1016/j.clnu.2020.10.011

89 Wu, X., Wu, H., Liu, L., Qiang, G. & Zhu, J. Serum zinc level and tissue ZIP4 expression are related to the prognosis of patients with stages I-III colon cancer. *Transl Cancer Res* **9**, 5585-5594 (2020). https://doi.org:10.21037/tcr-20-2571

90 Zhao, J. *et al.* Comparative study of serum zinc concentrations in benign and malignant prostate disease: A Systematic Review and Meta-Analysis. *Sci Rep* **6**, 25778 (2016). https://doi.org:10.1038/srep25778

91 Singh, K. P. *et al.* Effect of zinc on immune functions and host resistance against infection and tumor challenge. *Immunopharmacol Immunotoxicol* **14**, 813-840 (1992). https://doi.org:10.3109/08923979209009237

92 Satoh, M. *et al.* Prevention of carcinogenicity of anticancer drugs by metallothionein induction. *Cancer Res* **53**, 4767-4768 (1993).

93 Sun, J. *et al.* Reduction in squamous cell carcinomas in mouse skin by dietary zinc supplementation. *Cancer Med* **5**, 2032-2042 (2016). https://doi.org:10.1002/cam4.768

94 Fong, L. Y., Mancini, R., Nakagawa, H., Rustgi, A. K. & Huebner, K. Combined cyclin D1 overexpression and zinc deficiency disrupts cell cycle and accelerates mouse forestomach carcinogenesis. *Cancer Res* **63**, 4244-4252 (2003).

95 Wang, J. *et al.* Serum zinc as a biomarker to predict the efficacy of immune checkpoint inhibitors in cancers. *PloS one* **20**, e0326057 (2025). https://doi.org:10.1371/journal.pone.0326057

96 Tang, W. *et al.* Efficacy of zinc carnosine in the treatment of colorectal cancer and its potential in combination with immunotherapy in vivo. *Aging (Albany NY)* **14**, 8688-8699 (2022). https://doi.org:10.18632/aging.204380

97 Ying Yang, H. F., Xinyu Xu, Shankun Yao, Wenhao Yu and Zijian Guo. Zinc Ion-Induced Immune Responses in Antitumor Immunotherapy. *CCS Chemistry* **0**, 1-20 (2024). https://doi.org:10.31635/ccschem.023.202303514

98 Sugandha Narayan, R. D., Zaigham Abbas Rizvi, Amit Awasthi. Zinc dampens anti-tumor immunity by promoting Foxp3+ regulatory T cells. *Front Immunol* **15** (2024). https://doi.org:10.3389/fimmu.2024.1389387

99 Chang, W., Li, H., Ou, W. & Wang, S. Y. A novel zinc metabolism-related gene signature to predict prognosis and immunotherapy response in lung adenocarcinoma. *Front Immunol* **14**, 1147528 (2023). https://doi.org:10.3389/fimmu.2023.1147528

100 Lim, B., Kim, K. S. & Na, K. pH-Responsive Zinc Ion Regulating Immunomodulatory Nanoparticles for Effective Cancer Immunotherapy. *Biomacromolecules* **24**, 4263-4273 (2023). https://doi.org:10.1021/acs.biomac.3c00557

101 Kreuger, I. Z. M., Slieker, R. C., van Groningen, T. & van Doorn, R. Therapeutic Strategies for Targeting CDKN2A Loss in Melanoma. *J Invest Dermatol* **143**, 18-25 e11 (2023). https://doi.org:10.1016/j.jid.2022.07.016

102 Young, R. J. *et al.* Loss of CDKN2A expression is a frequent event in primary invasive melanoma and correlates with sensitivity to the CDK4/6 inhibitor PD0332991 in melanoma cell lines. *Pigment Cell Melanoma Res* **27**, 590-600 (2014). https://doi.org:10.1111/pcmr.12228

103 Grard, M. *et al.* Homozygous Co-Deletion of Type I Interferons and CDKN2A Genes in Thoracic Cancers: Potential Consequences for Therapy. *Front Oncol* **11**, 695770 (2021). https://doi.org:10.3389/fonc.2021.695770

104 Barriga, F. M. *et al.* MACHETE identifies interferon-encompassing chromosome 9p21.3 deletions as mediators of immune evasion and metastasis. *Nat Cancer* **3**, 1367-1385 (2022). https://doi.org:10.1038/s43018-022-00443-5

105 Tiwari, A., Trivedi, R. & Lin, S. Y. Tumor microenvironment: barrier or opportunity towards effective cancer therapy. *J Biomed Sci* **29**, 83 (2022). https://doi.org:10.1186/s12929-022-00866-3

106 Kather, J. N. *et al.* Topography of cancer-associated immune cells in human solid tumors. *Elife* **7** (2018). https://doi.org:10.7554/eLife.36967

107 Meyer, C. *et al.* Frequencies of circulating MDSC correlate with clinical outcome of melanoma patients treated with ipilimumab. *Cancer Immunol Immunother* **63**, 247-257 (2014). https://doi.org:10.1007/s00262-013-1508-5

108 Riaz, N. *et al.* Tumor and Microenvironment Evolution during Immunotherapy with Nivolumab. *Cell* **171**, 934-949 e916 (2017). https://doi.org:10.1016/j.cell.2017.09.028

109 Zhu, Y. *et al.* Disruption of tumour-associated macrophage trafficking by the osteopontin-induced colony-stimulating factor-1 signalling sensitises hepatocellular carcinoma to anti-PD-L1 blockade. *Gut* **68**, 1653-1666 (2019). https://doi.org:10.1136/gutjnl-2019-318419

110 Xu, J. *et al.* CSF1R signaling blockade stanches tumor-infiltrating myeloid cells and improves the efficacy of radiotherapy in prostate cancer. *Cancer Res* **73**, 2782-2794 (2013). https://doi.org:10.1158/0008-5472.CAN-12-3981

111 Stafford, J. H. *et al.* Colony stimulating factor 1 receptor inhibition delays recurrence of glioblastoma after radiation by altering myeloid cell recruitment and polarization. *Neuro Oncol* **18**, 797-806 (2016). https://doi.org:10.1093/neuonc/nov272

112 Freeman, G. J. *et al.* Engagement of the PD-1 immunoinhibitory receptor by a novel B7 family member leads to negative regulation of lymphocyte activation. *J Exp Med* **192**, 1027-1034 (2000). https://doi.org:10.1084/jem.192.7.1027

113 Hirano, F. *et al.* Blockade of B7-H1 and PD-1 by monoclonal antibodies potentiates cancer therapeutic immunity. *Cancer Res* **65**, 1089-1096 (2005).

114 Dhupkar, P., Gordon, N., Stewart, J. & Kleinerman, E. S. Anti-PD-1 therapy redirects macrophages from an M2 to an M1 phenotype inducing regression of OS lung metastases. *Cancer Med* **7**, 2654-2664 (2018). https://doi.org:10.1002/cam4.1518

115 Xu, C. *et al.* Protocol for detecting macrophage-mediated cancer cell phagocytosis in vitro and in vivo. *STAR Protoc* **4**, 101940 (2023). https://doi.org:10.1016/j.xpro.2022.101940

116 Vitale, I., Manic, G., Coussens, L. M., Kroemer, G. & Galluzzi, L. Macrophages and Metabolism in the Tumor Microenvironment. *Cell Metab* **30**, 36-50 (2019). https://doi.org:10.1016/j.cmet.2019.06.001

117 Tangudu, N. K. *et al.* ATR promotes mTORC1 activation via de novo cholesterol synthesis in p16-low cancer cells. *bioRxiv* (2023). https://doi.org:10.1101/2023.10.27.564195

118 Deleye, Y. *et al.* CDKN2A/p16INK4a suppresses hepatic fatty acid oxidation through the AMPKalpha2-SIRT1-PPARalpha signaling pathway. *J Biol Chem* **295**, 17310-17322 (2020). https://doi.org:10.1074/jbc.RA120.012543

119 Bantubungi, K. *et al.* Cdkn2a/p16Ink4a regulates fasting-induced hepatic gluconeogenesis through the PKA-CREB-PGC1alpha pathway. *Diabetes* **63**, 3199-3209 (2014). https://doi.org:10.2337/db13-1921

120 Khan, A., Liu, Y., Gad, M., Kenny, T. C. & Birsoy, K. Solute carriers: The gatekeepers of metabolism. *Cell* **188**, 869-884 (2025). https://doi.org:10.1016/j.cell.2025.01.015

121 Sage, M. A. G. & Duffy, D. M. Novel Plasma Membrane Androgen Receptor SLC39A9 Mediates Ovulatory Changes in Cells of the Monkey Ovarian Follicle. *Endocrinology* **165** (2024). https://doi.org:10.1210/endocr/bqae071

122 Converse, A. & Thomas, P. The zinc transporter ZIP9 (Slc39a9) regulates zinc dynamics essential to egg activation in zebrafish. *Sci Rep* **10**, 15673 (2020). https://doi.org:10.1038/s41598-020-72515-4

123 Thomas, P. & Dong, J. (-)-Epicatechin acts as a potent agonist of the membrane androgen receptor, ZIP9 (SLC39A9), to promote apoptosis of breast and prostate cancer cells. *The Journal of steroid biochemistry and molecular biology* **211**, 105906 (2021). https://doi.org:10.1016/j.jsbmb.2021.105906

124 Thomas, P., Pang, Y. & Dong, J. Membrane androgen receptor characteristics of human ZIP9 (SLC39A) zinc transporter in prostate cancer cells: Androgen-specific activation and involvement of an inhibitory G protein in zinc and MAP kinase signaling. *Mol Cell Endocrinol* **447**, 23-34 (2017). https://doi.org:10.1016/j.mce.2017.02.025

125 Matsuura, W. *et al.* SLC39A9 (ZIP9) regulates zinc homeostasis in the secretory pathway: characterization of the ZIP subfamily I protein in vertebrate cells. *Biosci Biotechnol Biochem* **73**, 1142-1148 (2009). https://doi.org:10.1271/bbb.80910

126 Yamaji, T. *et al.* A CRISPR Screen Using Subtilase Cytotoxin Identifies SLC39A9 as a Glycan-Regulating Factor. *iScience* **15**, 407-420 (2019). https://doi.org:10.1016/j.isci.2019.05.005

127 Zhang, T. *et al.* Crystal structures of a ZIP zinc transporter reveal a binuclear metal center in the transport pathway. *Sci Adv* **3**, e1700344 (2017). https://doi.org:10.1126/sciadv.1700344

128 Bulldan, A., Malviya, V. N., Upmanyu, N., Konrad, L. & Scheiner-Bobis, G. Testosterone/bicalutamide antagonism at the predicted extracellular androgen binding site of ZIP9. *Biochim Biophys Acta Mol Cell Res* **1864**, 2402-2414 (2017). https://doi.org:10.1016/j.bbamcr.2017.09.012

129 Bukiya, A. N. & Dopico, A. M. Common structural features of cholesterol binding sites in crystallized soluble proteins. *J Lipid Res* **58**, 1044-1054 (2017). https://doi.org:10.1194/jlr.R073452

130 Atger, V. M. *et al.* Cyclodextrins as catalysts for the removal of cholesterol from macrophage foam cells. *J Clin Invest* **99**, 773-780 (1997). https://doi.org:10.1172/JCI119223

131 Zidovetzki, R. & Levitan, I. Use of cyclodextrins to manipulate plasma membrane cholesterol content: evidence, misconceptions and control strategies. *Biochim Biophys Acta* **1768**, 1311-1324 (2007). https://doi.org:10.1016/j.bbamem.2007.03.026

132 Xiong, Y., Zhang, H. & Beach, D. Subunit rearrangement of the cyclin-dependent kinases is associated with cellular transformation. *Genes Dev* **7**, 1572-1583 (1993). https://doi.org:10.1101/gad.7.8.1572

133 (!!! INVALID CITATION !!! 12,13,31,92-96,107-111).

134 Bian, Y. *et al.* Cancer SLC43A2 alters T cell methionine metabolism and histone methylation. *Nature* **585**, 277-282 (2020). https://doi.org:10.1038/s41586-020-2682-1

135 Ho, P. C. *et al.* Phosphoenolpyruvate Is a Metabolic Checkpoint of Anti-tumor T Cell Responses. *Cell* **162**, 1217-1228 (2015). https://doi.org:10.1016/j.cell.2015.08.012

136 Chang, C. H. *et al.* Metabolic Competition in the Tumor Microenvironment Is a Driver of Cancer Progression. *Cell* **162**, 1229-1241 (2015). https://doi.org:10.1016/j.cell.2015.08.016

137 Li, Z. *et al.* SLC3A2 promotes tumor-associated macrophage polarization through metabolic reprogramming in lung cancer. *Cancer Sci* **114**, 2306-2317 (2023). https://doi.org:10.1111/cas.15760

138 Kyritsi, K. *et al.* Downregulation of p16 Decreases Biliary Damage and Liver Fibrosis in the Mdr2(/) Mouse Model of Primary Sclerosing Cholangitis. *Gene Expr* **20**, 89-103 (2020). https://doi.org:10.3727/105221620X15889714507961

139 Cudejko, C. *et al.* p16INK4a deficiency promotes IL-4-induced polarization and inhibits proinflammatory signaling in macrophages. *Blood* **118**, 2556-2566 (2011). https://doi.org:10.1182/blood-2010-10-313106

140 Fuentes, L. *et al.* Downregulation of the tumour suppressor p16INK4A contributes to the polarisation of human macrophages toward an adipose tissue macrophage (ATM)-like phenotype. *Diabetologia* **54**, 3150-3156 (2011). https://doi.org:10.1007/s00125-011-2324-0

141 Liang, Y. *et al.* p16(INK4a) Plays Critical Role in Exacerbating Inflammaging in High Fat Diet Induced Skin. *Oxid Med Cell Longev* **2022**, 3415528 (2022). https://doi.org:10.1155/2022/3415528

142 Che, H. *et al.* p16 deficiency attenuates intervertebral disc degeneration by adjusting oxidative stress and nucleus pulposus cell cycle. *eLife* **9** (2020). https://doi.org:10.7554/eLife.52570

143 Zhu, Z., Song, H. & Xu, J. CDKN2A Deletion in Melanoma Excludes T Cell Infiltration by Repressing Chemokine Expression in a Cell Cycle-Dependent Manner. *Front Oncol* **11**, 641077 (2021). https://doi.org:10.3389/fonc.2021.641077

144 Balli, D., Rech, A. J., Stanger, B. Z. & Vonderheide, R. H. Immune Cytolytic Activity Stratifies Molecular Subsets of Human Pancreatic Cancer. *Clin Cancer Res* **23**, 3129-3138 (2017). https://doi.org:10.1158/1078-0432.CCR-16-2128

145 Wartenberg, M. *et al.* Integrated Genomic and Immunophenotypic Classification of Pancreatic Cancer Reveals Three Distinct Subtypes with Prognostic/Predictive Significance. *Clin Cancer Res* **24**, 4444-4454 (2018). https://doi.org:10.1158/1078-0432.CCR-17-3401

146 Morrison, C. *et al.* Predicting response to checkpoint inhibitors in melanoma beyond PD-L1 and mutational burden. *J Immunother Cancer* **6**, 32 (2018). https://doi.org:10.1186/s40425-018-0344-8

147 Nowak, J. E., Harmon, K., Caldwell, C. C. & Wong, H. R. Prophylactic zinc supplementation reduces bacterial load and improves survival in a murine model of sepsis. *Pediatr Crit Care Med* **13**, e323-329 (2012). https://doi.org:10.1097/PCC.0b013e31824fbd90

148 Brazao, V. *et al.* Zinc supplementation increases resistance to experimental infection by Trypanosoma cruzi. *Vet Parasitol* **154**, 32-37 (2008). https://doi.org:10.1016/j.vetpar.2008.02.015

149 Humphrey, P. A., Ashraf, M. & Lee, C. M. Hepatic cells' mitotic and peritoneal macrophage phagocytic activities during Trypanosoma musculi infection in zinc-deficient mice. *J Natl Med Assoc* **89**, 259-267 (1997).

150 Salvin, S. B., Horecker, B. L., Pan, L. X. & Rabin, B. S. The effect of dietary zinc and prothymosin alpha on cellular immune responses of RF/J mice. *Clin Immunol Immunopathol* **43**, 281-288 (1987). https://doi.org:10.1016/0090-1229(87)90137-1

151 Nabeel-Shah, S. *et al.* C2H2-zinc-finger transcription factors bind RNA and function in diverse post-transcriptional regulatory processes. *Mol Cell* **84**, 3810-3825 e3810 (2024). https://doi.org:10.1016/j.molcel.2024.08.037

152 Jackson, K. A., Valentine, R. A., Coneyworth, L. J., Mathers, J. C. & Ford, D. Mechanisms of mammalian zinc-regulated gene expression. *Biochem Soc Trans* **36**, 1262-1266 (2008). https://doi.org:10.1042/BST0361262

153 Newcomer, K. *et al.* Malignant melanoma: evolving practice management in an era of increasingly effective systemic therapies. *Curr Probl Surg* **59**, 101030 (2022). https://doi.org:10.1016/j.cpsurg.2021.101030

154 Clinton, L. K. *et al.* The LAST guidelines in clinical practice: implementing recommendations for p16 use. *Am J Clin Pathol* **144**, 844-849 (2015). https://doi.org:10.1309/AJCPUXLP7XD8OQYY

155 Chan, S. H., Chiang, J. & Ngeow, J. CDKN2A germline alterations and the relevance of genotype-phenotype associations in cancer predisposition. *Hered Cancer Clin Pract* **19**, 21 (2021). https://doi.org:10.1186/s13053-021-00178-x

156 Fraker, P. J. & King, L. E. Reprogramming of the immune system during zinc deficiency. *Annu Rev Nutr* **24**, 277-298 (2004). https://doi.org:10.1146/annurev.nutr.24.012003.132454

157 Costello, L. C. & Franklin, R. B. Cytotoxic/tumor suppressor role of zinc for the treatment of cancer: an enigma and an opportunity. *Expert Rev Anticancer Ther* **12**, 121-128 (2012). https://doi.org:10.1586/era.11.190

158 Mao, W. *et al.* Statin shapes inflamed tumor microenvironment and enhances immune checkpoint blockade in non-small cell lung cancer. *JCI Insight* **7** (2022). https://doi.org:10.1172/jci.insight.161940

159 Cantini, L. *et al.* High-intensity statins are associated with improved clinical activity of PD-1 inhibitors in malignant pleural mesothelioma and advanced non-small cell lung cancer patients. *Eur J Cancer* **144**, 41-48 (2021). https://doi.org:10.1016/j.ejca.2020.10.031

160 Cortellini, A. *et al.* Integrated analysis of concomitant medications and oncological outcomes from PD-1/PD-L1 checkpoint inhibitors in clinical practice. *J Immunother Cancer* **8** (2020). https://doi.org:10.1136/jitc-2020-001361

161 Kansal, V. *et al.* Statin drugs enhance responses to immune checkpoint blockade in head and neck cancer models. *J Immunother Cancer* **11** (2023). https://doi.org:10.1136/jitc-2022-005940

162 Takada, K. *et al.* A propensity score-matched analysis of the impact of statin therapy on the outcomes of patients with non-small-cell lung cancer receiving anti-PD-1 monotherapy: a multicenter retrospective study. *BMC Cancer* **22**, 503 (2022). https://doi.org:10.1186/s12885-022-09385-8

163 Liao, Y., Lin, Y., Ye, X. & Shen, J. Concomitant Statin Use and Survival in Patients With Cancer on Immune Checkpoint Inhibitors: A Meta-Analysis. *JCO Oncol Pract*, OP2400583 (2025). https://doi.org:10.1200/OP-24-00583

164 Wu, J. Y. *et al.* Cancer-Derived Succinate Promotes Macrophage Polarization and Cancer Metastasis via Succinate Receptor. *Mol Cell* **77**, 213-227 e215 (2020). https://doi.org:10.1016/j.molcel.2019.10.023

165 Reinfeld, B. I. *et al.* Cell-programmed nutrient partitioning in the tumour microenvironment. *Nature* **593**, 282-288 (2021). https://doi.org:10.1038/s41586-021-03442-1

166 Epstein, M. M. *et al.* Dietary zinc and prostate cancer survival in a Swedish cohort. *Am J Clin Nutr* **93**, 586-593 (2011). https://doi.org:10.3945/ajcn.110.004804

167 Gonzalez, A., Peters, U., Lampe, J. W. & White, E. Zinc intake from supplements and diet and prostate cancer. *Nutr Cancer* **61**, 206-215 (2009). https://doi.org:10.1080/01635580802419749

168 Li, L. & Gai, X. The association between dietary zinc intake and risk of pancreatic cancer: a meta-analysis. *Biosci Rep* **37** (2017). https://doi.org:10.1042/BSR20170155

169 Pan, S. Y. *et al.* Antioxidants and breast cancer risk- a population-based case-control study in Canada. *BMC Cancer* **11**, 372 (2011). https://doi.org:10.1186/1471-2407-11-372

170 Adzersen, K. H., Jess, P., Freivogel, K. W., Gerhard, I. & Bastert, G. Raw and cooked vegetables, fruits, selected micronutrients, and breast cancer risk: a case-control study in Germany. *Nutr Cancer* **46**, 131-137 (2003). https://doi.org:10.1207/S15327914NC4602_05

171 Lin, L. C. *et al.* Effects of zinc supplementation on clinical outcomes in patients receiving radiotherapy for head and neck cancers: a double-blinded randomized study. *Int J Radiat Oncol Biol Phys* **70**, 368-373 (2008). https://doi.org:10.1016/j.ijrobp.2007.06.073

172 Shi, Z. *et al.* Association between dietary zinc intake and mortality among Chinese adults: findings from 10-year follow-up in the Jiangsu Nutrition Study. *Eur J Nutr* **57**, 2839-2846 (2018). https://doi.org:10.1007/s00394-017-1551-7

173 Gutierrez-Gonzalez, E. *et al.* Dietary Zinc and Risk of Prostate Cancer in Spain: MCC-Spain Study. *Nutrients* **11** (2018). https://doi.org:10.3390/nu11010018

174 Zhang, Y., Song, M., Mucci, L. A. & Giovannucci, E. L. Zinc supplement use and risk of aggressive prostate cancer: a 30-year follow-up study. *Eur J Epidemiol* **37**, 1251-1260 (2022). https://doi.org:10.1007/s10654-022-00922-0

175 Gallus, S. *et al.* Dietary zinc and prostate cancer risk: a case-control study from Italy. *Eur Urol* **52**, 1052-1056 (2007). https://doi.org:10.1016/j.eururo.2007.01.094

176 Fernandez-Lazaro, C. I. *et al.* Dietary Antioxidant Vitamins and Minerals and Breast Cancer Risk: Prospective Results from the SUN Cohort. *Antioxidants (Basel)* **10** (2021). https://doi.org:10.3390/antiox10030340

177 Luo, H. *et al.* Association between Dietary Zinc and Selenium Intake, Oxidative Stress-Related Gene Polymorphism, and Colorectal Cancer Risk in Chinese Population - A Case-Control Study. *Nutr Cancer* **73**, 1621-1630 (2021). https://doi.org:10.1080/01635581.2020.1804950

178 Bravi, F. *et al.* Dietary intake of selected micronutrients and the risk of pancreatic cancer: an Italian case-control study. *Ann Oncol* **22**, 202-206 (2011). https://doi.org:10.1093/annonc/mdq302

179 Hoppe, C. *et al.* Zinc as a complementary treatment for cancer patients: a systematic review. *Clin Exp Med* **21**, 297-313 (2021). https://doi.org:10.1007/s10238-020-00677-6

180 Trumbo, P., Yates, A. A., Schlicker, S. & Poos, M. Dietary reference intakes: vitamin A, vitamin K, arsenic, boron, chromium, copper, iodine, iron, manganese, molybdenum, nickel, silicon, vanadium, and zinc. *J Am Diet Assoc* **101**, 294-301 (2001). https://doi.org:10.1016/S0002-8223(01)00078-5

181 Wang, K. *et al.* Zinc ions activate AKT and promote prostate cancer cell proliferation via disrupting AKT intramolecular interaction. *Oncogene* **44**, 8-18 (2025). https://doi.org:10.1038/s41388-024-03195-x

182 Taylor, K. M. *et al.* ZIP7-mediated intracellular zinc transport contributes to aberrant growth factor signaling in antihormone-resistant breast cancer Cells. *Endocrinology* **149**, 4912-4920 (2008). https://doi.org:10.1210/en.2008-0351

183 Lelliott, E. J. *et al.* Intracellular zinc protects tumours from T cell-mediated cytotoxicity. *Cell Death Differ* **31**, 1707-1716 (2024). https://doi.org:10.1038/s41418-024-01369-4

184 Provinciali, M., Pierpaoli, E., Bartozzi, B. & Bernardini, G. Zinc Induces Apoptosis of Human Melanoma Cells, Increasing Reactive Oxygen Species, p53 and FAS Ligand. *Anticancer Res* **35**, 5309-5316 (2015).

185 Xu, M. *et al.* Zinc-based radioenhancers to activate tumor radioimmunotherapy by PD-L1 and cGAS-STING pathway. *J Nanobiotechnology* **22**, 782 (2024). https://doi.org:10.1186/s12951-024-02999-z

186 Du, M. & Chen, Z. J. DNA-induced liquid phase condensation of cGAS activates innate immune signaling. *Science* **361**, 704-709 (2018). https://doi.org:10.1126/science.aat1022

187 Zhang, L. *et al.* A Peritumorally Injected Immunomodulating Adjuvant Elicits Robust and Safe Metalloimmunotherapy against Solid Tumors. *Adv Mater* **34**, e2206915 (2022). https://doi.org:10.1002/adma.202206915

188 Sies, H. & Jones, D. P. Reactive oxygen species (ROS) as pleiotropic physiological signalling agents. *Nat Rev Mol Cell Biol* **21**, 363-383 (2020). https://doi.org:10.1038/s41580-020-0230-3

189 Gide, T. N. *et al.* Distinct Immune Cell Populations Define Response to Anti-PD-1 Monotherapy and Anti-PD-1/Anti-CTLA-4 Combined Therapy. *Cancer Cell* **35**, 238-255 e236 (2019). https://doi.org:10.1016/j.ccell.2019.01.003

190 Lee, J. H. *et al.* Transcriptional downregulation of MHC class I and melanoma de-differentiation in resistance to PD-1 inhibition. *Nat Commun* **11**, 1897 (2020). https://doi.org:10.1038/s41467-020-15726-7

191 Hugo, W. *et al.* Genomic and Transcriptomic Features of Response to Anti-PD-1 Therapy in Metastatic Melanoma. *Cell* **165**, 35-44 (2016). https://doi.org:10.1016/j.cell.2016.02.065

192 Ayers, M. *et al.* IFN-γ-related mRNA profile predicts clinical response to PD-1 blockade. *The Journal of clinical investigation* **127**, 2930-2940 (2017). https://doi.org:10.1172/jci91190

193 Gyorffy, B. Integrated analysis of public datasets for the discovery and validation of survival-associated genes in solid tumors. *Innovation (Camb)* **5**, 100625 (2024). https://doi.org:10.1016/j.xinn.2024.100625

194 Gyorffy, B. Transcriptome-level discovery of survival-associated biomarkers and therapy targets in non-small-cell lung cancer. *Br J Pharmacol* **181**, 362-374 (2024). https://doi.org:10.1111/bph.16257

195 Kovacs, S. A., Fekete, J. T. & Gyorffy, B. Predictive biomarkers of immunotherapy response with pharmacological applications in solid tumors. *Acta Pharmacol Sin* **44**, 1879-1889 (2023). https://doi.org:10.1038/s41401-023-01079-6

196 Jerby-Arnon, L. *et al.* A Cancer Cell Program Promotes T Cell Exclusion and Resistance to Checkpoint Blockade. *Cell* **175**, 984-997 e924 (2018). https://doi.org:10.1016/j.cell.2018.09.006

197 Chen, Y. P. *et al.* Single-cell transcriptomics reveals regulators underlying immune cell diversity and immune subtypes associated with prognosis in nasopharyngeal carcinoma. *Cell Res* **30**, 1024-1042 (2020). https://doi.org:10.1038/s41422-020-0374-x

198 Uphoff, C. C. & Drexler, H. G. Detection of mycoplasma contaminations. *Methods Mol Biol* **290**, 13-23 (2005). https://doi.org:10.1385/1-59259-838-2:013

199 Sullivan, M. R. *et al.* Quantification of microenvironmental metabolites in murine cancers reveals determinants of tumor nutrient availability. *Elife* **8** (2019). https://doi.org:10.7554/eLife.44235

200 Corrin A. Wohlhieter *et al.* An optimized NGS sample preparation protocol for in vitro CRISPR screens. *STAR Protocols* **2**, 100390 (2021). https://doi.org:10.1016/j.xpro.2021.100390

201 Alker, W., Schwerdtle, T., Schomburg, L. & Haase, H. A Zinpyr-1-based Fluorimetric Microassay for Free Zinc in Human Serum. *Int J Mol Sci* **20** (2019). https://doi.org:10.3390/ijms20164006

202 Stringer, C., Wang, T., Michaelos, M. & Pachitariu, M. Cellpose: a generalist algorithm for cellular segmentation. *Nat Methods* **18**, 100-106 (2021). https://doi.org:10.1038/s41592-020-01018-x

203 Dimri, G. P. *et al.* A biomarker that identifies senescent human cells in culture and in aging skin in vivo. *Proc Natl Acad Sci U S A* **92**, 9363-9367 (1995). https://doi.org:10.1073/pnas.92.20.9363